

# NAVAL POSTGRADUATE SCHOOL

## Monterey, California



## THESIS

### **A COUPLED HYDRODYNAMIC/STRUCTURAL MODEL FOR SHIP/RAMP/BARGE INTERFACE**

by

Antonios Dalakos

December 2001

Thesis Advisor:

Fotis A. Papoulias

**Approved for public release; distribution is unlimited**

## Report Documentation Page

<b>Report Date</b> 19 Dec 2001	<b>Report Type</b> N/A	<b>Dates Covered (from... to)</b> -
<b>Title and Subtitle</b> A Coupled Hydrodynamic/Structural Model for Ship/Ramp/Barge Interface	<b>Contract Number</b>	
	<b>Grant Number</b>	
	<b>Program Element Number</b>	
<b>Author(s)</b> Dalakos, Antonios	<b>Project Number</b>	
	<b>Task Number</b>	
	<b>Work Unit Number</b>	
<b>Performing Organization Name(s) and Address(es)</b> Naval Postgraduate School Monterey, California	<b>Performing Organization Report Number</b>	
<b>Sponsoring/Monitoring Agency Name(s) and Address(es)</b>	<b>Sponsor/Monitor's Acronym(s)</b>	
	<b>Sponsor/Monitor's Report Number(s)</b>	
<b>Distribution/Availability Statement</b> Approved for public release, distribution unlimited		
<b>Supplementary Notes</b>		
<b>Abstract</b>		
<b>Subject Terms</b>		
<b>Report Classification</b> unclassified	<b>Classification of this page</b> unclassified	
<b>Classification of Abstract</b> unclassified	<b>Limitation of Abstract</b> UU	
<b>Number of Pages</b> 143		

THIS PAGE INTENTIONALLY LEFT BLANK

<b>REPORT DOCUMENTATION PAGE</b>			<i>Form Approved OMB No. 0704-0188</i>	
Public reporting burden for this collection of information is estimated to average 1 hour per response, including the time for reviewing instruction, searching existing data sources, gathering and maintaining the data needed, and completing and reviewing the collection of information. Send comments regarding this burden estimate or any other aspect of this collection of information, including suggestions for reducing this burden, to Washington headquarters Services, Directorate for Information Operations and Reports, 1215 Jefferson Davis Highway, Suite 1204, Arlington, VA 22202-4302, and to the Office of Management and Budget, Paperwork Reduction Project (0704-0188) Washington DC 20503.				
<b>1. AGENCY USE ONLY (Leave blank)</b>		<b>2. REPORT DATE</b> December 2001	<b>3. REPORT TYPE AND DATES COVERED</b> Master's Thesis	
<b>4. TITLE AND SUBTITLE:</b> A Coupled Hydrodynamic/Structural Model for Ship/Ramp/Barge Interface			<b>5. FUNDING NUMBERS</b>	
<b>6. AUTHOR(S)</b> Antonios Dalakos				
<b>7. PERFORMING ORGANIZATION NAME(S) AND ADDRESS(ES)</b> Naval Postgraduate School Monterey, CA 93943-5000			<b>8. PERFORMING ORGANIZATION REPORT NUMBER</b>	
<b>9. SPONSORING / MONITORING AGENCY NAME(S) AND ADDRESS(ES)</b> N/A			<b>10. SPONSORING / MONITORING AGENCY REPORT NUMBER</b>	
<b>11. SUPPLEMENTARY NOTES</b> The views expressed in this thesis are those of the author and do not reflect the official policy or position of the Department of Defense or the U.S. Government.				
<b>12a. DISTRIBUTION / AVAILABILITY STATEMENT</b> Approved for public release; distribution is unlimited			<b>12b. DISTRIBUTION CODE</b>	
<b>13. ABSTRACT (maximum 200 words)</b>  A mathematical model describing the fundamental dynamics in the interface problem between a ship, a barge, and a connecting ramp is developed and solved. The hydrodynamics for the ship and the barge are described by a 12-degree of freedom fully coupled model, which is based on potential theory and incorporates proximity effects. Ramp structural dynamics are studied by a finite element model, which has been calibrated based on detailed studies of commercially available codes. The models were coupled together through a spring/damper and the solution of the system was obtained in both regular waves and a representative sea state. Parametric studies with regards to different coupling conditions indicate that optimization based on either relative motions or ramp maximum stress is possible.				
<b>14. SUBJECT TERMS</b> Hydrodynamic model, RORO, Roll-On Roll-Off, RRDF, CAPE-T, CAPE-H, CAPE-D, WAMIT, RRDF, Structural Model, Finite Element Model, Ramp, Coupling, Barge.			<b>15. NUMBER OF PAGES</b> 143	
			<b>16. PRICE CODE</b>	
<b>17. SECURITY CLASSIFICATION OF REPORT</b> Unclassified	<b>18. SECURITY CLASSIFICATION OF THIS PAGE</b> Unclassified	<b>19. SECURITY CLASSIFICATION OF ABSTRACT</b> Unclassified	<b>20. LIMITATION OF ABSTRACT</b> UL	

NSN 7540-01-280-5500

Standard Form 298 (Rev. 2-89)  
Prescribed by ANSI Std. Z39-18

THIS PAGE INTENTIONALLY LEFT BLANK

Approved for public release; distribution is unlimited

**A COUPLED HYDRODYNAMIC/STRUCTURAL MODEL FOR  
SHIP/RAMP/BARGE INTERFACE**

Antonios Dalakos  
Lieutenant, Hellenic Navy  
B.S., Hellenic Naval Academy, 1990

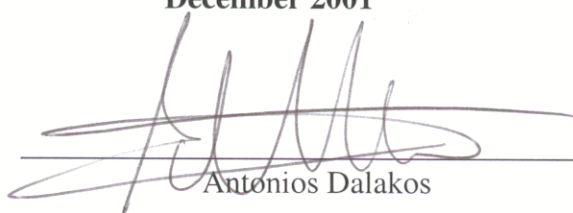
Submitted in partial fulfillment of the  
requirements for the degree of

**MASTER OF SCIENCE IN MECHANICAL ENGINEERING**


from the

**NAVAL POSTGRADUATE SCHOOL  
December 2001**

Author:

  
Antonios Dalakos

Approved by:

  
Fotis A. Papoulias, Thesis Advisor

  
Terry McNelley, Chairman  
Department of Mechanical Engineering

THIS PAGE INTENTIONALLY LEFT BLANK

## **ABSTRACT**

A mathematical model describing the fundamental dynamics in the interface problem between a ship, a barge, and a connecting ramp is developed and solved. The hydrodynamics for the ship and the barge are described by a 12-degree of freedom fully coupled model, which is based on potential theory and incorporates proximity effects. Ramp structural dynamics are studied by a finite element model, which has been calibrated based on detailed studies of commercially available codes. The models were coupled together through a spring/damper and the solution of the system was obtained in both regular waves and a representative sea state. Parametric studies with regards to different coupling conditions indicate that optimization based on either relative motions or ramp maximum stress is possible.



THIS PAGE INTENTIONALLY LEFT BLANK

## TABLE OF CONTENTS

<b>I.</b>	<b>INTRODUCTION.....</b>	<b>1</b>
<b>A.</b>	<b>BACKGROUND.....</b>	<b>1</b>
<b>B.</b>	<b>OBJECTIVES.....</b>	<b>2</b>
<b>II.</b>	<b>HYDRODYNAMIC MODEL OF THE SHIP AND THE BARGE (RRDF)</b>	
	<b>RESPONSE IN REGULAR WAVES.....</b>	<b>3</b>
<b>A.</b>	<b>INTRODUCTION.....</b>	<b>3</b>
<b>B.</b>	<b>DEVELOPMENT OF SEAKEEPING CALCULATIONS.....</b>	<b>3</b>
<b>C.</b>	<b>COMPUTATION OF MOTIONS IN REGULAR WAVES.....</b>	<b>6</b>
1.	Calculation Of Motions Using Six Degrees Of Freedom .....	6
2.	Calculation Of Motions Using a Three Degrees Of Freedom	
	Approximation.....	11
3.	Determination Of the Hydrodynamic Forces and Coefficients	
	Using WAMIT .....	12
<b>D.</b>	<b>RESULTS.....</b>	<b>18</b>
<b>III.</b>	<b>RAMP MODELING .....</b>	<b>23</b>
<b>A.</b>	<b>INTRODUCTION.....</b>	<b>23</b>
<b>B.</b>	<b>RAMP MODELING USING FINITE ELEMENT METHOD.....</b>	<b>23</b>
<b>C.</b>	<b>VALIDATION OF THE RAMP MODEL.....</b>	<b>28</b>
<b>IV.</b>	<b>COUPLING BETWEEN SHIP RAMP AND BARGE MODELS.....</b>	<b>31</b>
<b>A.</b>	<b>INTRODUCTION.....</b>	<b>31</b>
<b>B.</b>	<b>COUPLING BETWEEN SHIP, RAMP, BARGE.....</b>	<b>31</b>
1.	Spring–Damper Coupling Condition .....	32
2.	Roll Mitigation Coupling Condition.....	36
<b>C.</b>	<b>COUPLED SOLUTION IN FREQUENCY DOMAIN .....</b>	<b>38</b>
<b>D.</b>	<b>STRESS CALCULATION FOR THE RAMP .....</b>	<b>40</b>
<b>E.</b>	<b>RESULTS.....</b>	<b>41</b>
<b>V.</b>	<b>RESPONSE IN A SEAWAY.....</b>	<b>43</b>
<b>A.</b>	<b>INTRODUCTION.....</b>	<b>43</b>
<b>B.</b>	<b>DESCRIPTION OF THE SEAWAY.....</b>	<b>43</b>
<b>C.</b>	<b>SHIP/RAMP/BARGE RESPONSE SPECTRAL ANALYSIS .....</b>	<b>46</b>
<b>D.</b>	<b>RESULTS.....</b>	<b>48</b>
<b>VI.</b>	<b>CONCLUSIONS AND RECOMMENDATIONS.....</b>	<b>51</b>
<b>A.</b>	<b>CONCLUSIONS.....</b>	<b>51</b>
<b>B.</b>	<b>RECOMMENDATIONS.....</b>	<b>52</b>
	<b>APPENDIX A .....</b>	<b>53</b>
	<b>APPENDIX B.....</b>	<b>77</b>
	<b>APPENDIX C .....</b>	<b>105</b>
	<b>LIST OF REFERENCES .....</b>	<b>125</b>
	<b>INITIAL DISTRIBUTION LIST .....</b>	<b>127</b>

THIS PAGE INTENTIONALLY LEFT BLANK

## LIST OF FIGURES

Figure 1.	Rigid Body Motions of a Vessel, from Ref. [2].....	7
Figure 2.	Sketch Defining the Relative Position and Geometry of the CAPE-D and RRDF .....	10
Figure 3.	Sketch Defining the Coordinates, Fluid Depth, and Wave-Heading Angle from Ref. [3].....	12
Figure 4.	An Isometric View of the RRDF.....	19
Figure 5.	Typical Views of the Cape-D Ship Class.....	19
Figure 6.	Mesh of the Ramp Finite Element Model Showing the Numbering of the DOFs. ....	30
Figure 7.	Sketch of the Ship-Stern Ramp-Barge Arrangement. ....	77

THIS PAGE INTENTIONALLY LEFT BLANK

## LIST OF TABLES

Table 1.	Natural Frequencies of the Ramp Model. ....	29
Table 2	Parameters used in the Numerical Solution .....	77

THIS PAGE INTENTIONALLY LEFT BLANK

## **ACKNOWLEDGMENTS**

The author would like to thank professor Fotis A. Papoulas for all the guidance and unlimited help during the research and completion of this thesis. The author would also like to thank his wife Stavroula, and his newborn son Christos for all their patience, understanding and support.



THIS PAGE INTENTIONALLY LEFT BLANK

# **I. INTRODUCTION**

## **A. BACKGROUND**

In the recent years, the United States Military has taken an increasing interest in developing the ability to offload vehicles and machinery from large roll-on and roll-off (RO/RO) vessels in open seas. Several classes of vessels provided for this purpose, including are LMSRs, CAPE-Ds, CAPE-Hs and CAPE-Ts. Photos of these vessels and their principal characteristics can be found at the results section of Chapter III. Except for the difference in displacement between the different classes of ships, there is another significant difference, namely in the ramp design and placement aboard the ship - stern or side ramps. Equipment is going to be offloaded aboard a discharge facility that is specifically designed for that purpose. The RO/RO Discharge Facility (RRDF) is the interface between the ship's ramp and lighters/landing craft. Operational requirements for equipment transfer are set at sea state 3. However, the current design of the Ramp/RRDF system is only capable of operations in sea state 2 and below. The most limiting conditions result from high relative motions between the ship and the RRDF as well as the induced stresses that may exceed the yield stress of the material.

Successful implementation of a Ramp/RRDF Motion Compensation/Mitigation System will provide a significant increase in military readiness and capability of the RO/RO ships by enabling ramp operations during sea state 3, thus increasing the operational window by up to 50% (Applebee et al. 1997). Previous studies on the same subject, done at the Naval Postgraduate School [Ref. 3] and the University of Notre Dame [Ref. 5], have suggested that active or passive motion compensation can reduce the motions and the stresses of the ramp. Moreover, detailed finite element models of the various ship's ramps have been created and tested for stress and natural frequencies calculations [Ref. 6]. In Ref. [5] the hydrodynamic properties of the ships were approximated by a constant coefficient mass-spring-damper system, and active control techniques were designed and analyzed. In Ref. [3] several simplifying assumptions were made in the development of the dynamic model of the vessels and their interface. Ship motions were approximated by the vertical plane equations only, and the ramp was modeled as a generic second order system.

## **B. OBJECTIVES**

This thesis will attempt to overcome some of the limitations of the previous studies. It will focus on creating a mathematical dynamic model for the ship and the barge (RRDF). These models are going to be created using the latest calculation tools for marine vehicles so that vessel motions can be calculated with the least number of simplifying assumptions. A finite element model of the ship's ramp is going to be created so that it can be used in both the structural coupling of the two vessels and in ramp stress calculations. Once the equations of motion of the vessels in the frequency domain are written, the two vessels are going to be coupled with the ramp by using a specified coupling condition. This will allow calculation of the new motion of the ships along with the displacement field of the ramp. In this way the response in regular waves will be calculated. Finally the response in a seaway of the coupled system will be expressed in terms of standard seaway parameters.

For demonstration purposes the CAPE-D class of ships, with stern ramp, was chosen along with the new RRDF 2000 model. The coupling condition chosen for demonstration will be spring-damper coupling condition with constant parameters, modeling a standard motion isolation system. The method presented in this work is, however, general enough so that additional coupling conditions can be considered. Finally, a design methodology for proper motion mitigation is presented along with parametric studies for different isolator properties.

## **II. HYDRODYNAMIC MODEL OF THE SHIP AND THE BARGE (RRDF) RESPONSE IN REGULAR WAVES**

### **A. INTRODUCTION**

Modern seakeeping computations are used in all aspects of the engineering of the marine environment. The computations are performed using a variety of techniques-from simple strip theory to extremely complex fully nonlinear unsteady Reynolds Averaged Navier-Stokes equations in the time domain.

The major difficulties in seakeeping computations are the nonlinearities. These are nonlinearities associated with the fluid in the form of viscosity and the velocity squared terms in the pressure equation. The free surface causes nonlinear behavior due to the nature of the free-surface boundary conditions and the nonlinear behavior of the incident waves.

### **B. DEVELOPMENT OF SEAKEEPING CALCULATIONS**

For the interested reader a detailed historical development of seakeeping calculations can be found in Ogilvie (1977), Newman (1978), Mauro (1989) and Beck & Reed (2001) [Ref. 1]. A short historical approach to seakeeping computation will be presented here based on Beck & Reed (2001) [Ref. 1] where the most recent computation methods were evaluated.

The effort of predicting the response of a vessel in different sea conditions has a long history starting with Froude's original work on rolling (Froude 1861). Modern computations began with two developments in the 1950's. The first was the use of random process theory to determine the statistics of the ship responses in a seaway. The second was the development of the linear ship motion theories to predict the responses of the ship to regular waves.

In 1953 St. Denis and Pierson in their seminal paper proposed a method to predict the statistics of ship responses to a realistic seaway. Using spectral methods developed in other fields, they related the spectral density of ship responses to the input ocean wave spectrum. Two of their assumptions are critical: 1) the sea surface is an ergodic, Gaussian random process with zero mean and 2) the ship can be represented by a linear system.

Once the probability density function for a given response is known, all the desired statistics of the response can easily be determined. The linear system assumption allows the spectral density of any given response to be found by multiplying the incident wave spectrum by the square of the Response Amplitude Operator (or RAO) of the desired response. At any single frequency, the RAO is the amplitude and the phase of the desired response to regular incident waves acting on the vessel at the given frequency.

In the 1950's the development of analytic prediction techniques was started. The thin-ship approximation of Michell (1898) was examined critically by Peters and Stoker (1957). The first order theory was rather trivial in that it balanced hydrodynamic forces due to the undisturbed incident wave pressure field (the Froude-Krylov exciting force) and the hydrostatic restoring forces with the ship's mass time acceleration term. Newman (1961) avoided the shortcomings of Peters and Stoker by introducing refinements using a systematic expansion in multiple small parameters. Unfortunately, as with thin-ship theory, most nontrivial hydrodynamic effects are higher order compared to the Froude-Krylov exciting force and the hydrostatic restoring force.

At the same time an alternative strip slender-body was also being studied. Korvin-Kroukovsky (1955) did the initial work. Using a combination of slender-body theory and good physical insight, they developed a theory for heave and pitch that was suitable for numerical computations for the newly emerging digital computers. Strip theory was the first ship motion theory that gave results with enough engineering accuracy that the predicted motions were useful for design purposes. In the late 1960's more comprehensive strip theories were developed, most widely cited is Salvensen, et al. (1970). Using a combination of mathematics and judicious assumptions, these researchers arrived at a form of strip theory that today is still the most widely used method for seakeeping computations of ships.

Strip theory is a short wavelength theory and slender-body theory is a long wavelength theory. Attempts have been made to bridge the gap and find the theory that is valid over a wide frequency range. The interpolation theory of Mauro (1970) and the unified theory of Newman are typical examples. Comparisons with experimental results

by Sclavounos (1990) have indicated improved predictions relative to strip theory predictions.

By the late 1970's the Neumann-Kelvin approach was starting to be used. In this approach the body boundary condition is applied on the mean position of the exact body surface and the linearized free-surface boundary condition is used. The traditional approach to solve the Neumann-Kelvin problem is to use boundary integral methods in which the solution is formulated in terms of integrals of fundamental singularities (source and dipoles) over the surface surrounding the fluid domain.

Hess and Smith (1964) pioneered boundary element methods for flow without a free surface (equivalent to a double-body flow with a rigid body surface). Using just a source distribution, they subdivide the body surface into  $N$  flat quadrilaterals over which the source strength was assumed constant. The flat quadrilaterals were often called panels and now the term "panel methods" has come to mean any solution technique in which the body surface (and possibly other surfaces of the problem) has been subdivided. In panel methods, two tasks require almost all the computational effort. The first is setting up the influence matrix that requires multiple evaluations of the Green function for the problem. The second is solving the resulting linear system of equations.

Boundary element methods, while the most popular, are not the only methods available to solve the Neumann-Kelvin problem. Finite element or finite difference approaches can also be used. The only drawback is the mesh generation for a complex body geometry. The total computation effort and accuracy of the different numerical techniques depends on the details of the problem, the code, and the computers on which it is to be run. Several commercial codes are available, the first probably being Garrison (1978) and the most widely used is Wave Analysis Massachusetts Institute of Technology (WAMIT) (Korsmeyer et al. 1988). The codes have been extended to include second order mean drift and slowly vary forces.

WAMIT is a radiation/diffraction program developed for the analysis of the interaction of surface waves with offshore structures. WAMIT was used for the mathematical modeling of the barge and the ship and is based on a three-dimensional panel method. The theory and formulation of WAMIT is described in the following

section. The most recent developments and computation methods are described in detail in [Ref. 1]

### **C. COMPUTATION OF MOTIONS IN REGULAR WAVES**

The response of a ship advancing in a seaway is a complicated phenomenon involving the interactions between the vessel dynamics and several distinct hydrodynamic forces. All ship responses are nonlinear to some extent but in many cases when nonlinearities are small a linear theory will yield good predictions. As discussed in the previous section, the seaway can be considered a random process and spectral techniques can be used to define the characteristics of the seaway. By knowing the responses of a ship to regular waves of different frequencies, we can predict the statistics of the response to actual random seaways. In Ref. [2] the interested reader could find more details about the computation of vessel's motion, here a short discussion will be presented.

#### **1. Calculation Of Motions Using Six Degrees Of Freedom**

A ship advancing at a steady mean forward speed with arbitrary heading in a train of regular waves will move in six degrees of freedom. That is the ship's motion can be considered to be made up of three translational components, surge, sway and heave, and three rotational components, roll, pitch and yaw as shown in Figure 1. The six modes of motion are therefore:

$$\eta_1 = \textit{surge} = \text{translation in x-direction}$$

$$\eta_2 = \textit{sway} = \text{translation in y-direction}$$

$$\eta_3 = \textit{heave} = \text{translation in z-direction}$$

$$\eta_4 = \textit{roll} = \text{rotation about x-axis}$$

$$\eta_5 = \textit{pitch} = \text{rotation about y-axis}$$

$$\eta_6 = \textit{yaw} = \text{rotation about z-axis}$$

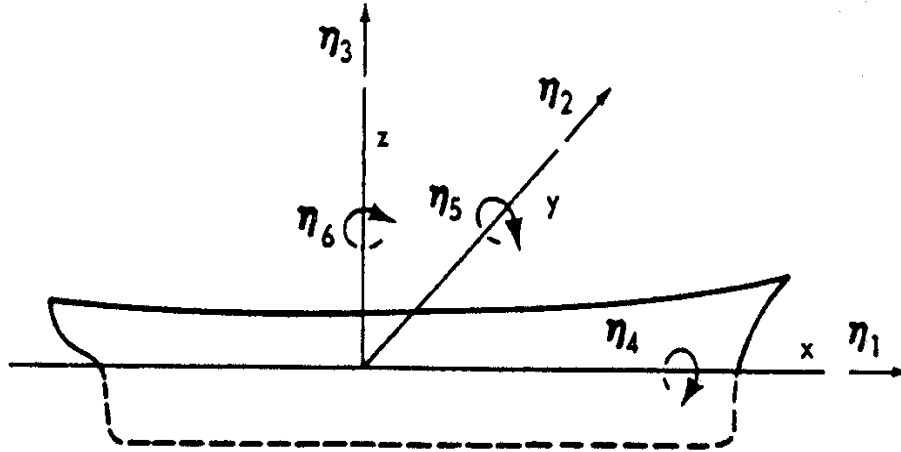


Figure 1. Rigid Body Motions of a Vessel, from Ref. [2]

In the problem to be formulated here, as origin will be considered a point in the waterline ( $z=0$ ), on the centerline ( $y=0$ ) and at the longitudinal center of gravity (which is also the longitudinal center of buoyancy for a freely floating body).

In order to be able to compute all responses of any vessel to regular waves, it is necessary to deal with the full six degrees of freedom equations, considering important couplings among them. Here only the final linear form of the equations of motion will be presented. Detailed derivations of the equations of motion may be found in Salvensen, et al (1970), Newman (1977), Ogilvie (1964), or Wehausen (1971).

The linearization of the equations is made on the basis of small motions. The motions will in general be small if the ship is stable and the incident wave amplitude is relatively small. The principal exceptions to this rule are resonant situations where damping is small, e.g., roll resonance in beam seas. Experimental and theoretical investigations have shown that a linear analysis of ship motions gives excellent predictions over a wide variety of sea conditions and vessel types. In situations where the linear theory assumptions are in doubt, only experiments can be used to compare the calculation results.

In linear theory, the responses of the vessel will be linear with (i.e. directly proportional to) wave amplitude and occur at the frequency at which the ship perceives the incident waves. This is an important point because even though it allows the use of



powerful linear tools, it also puts limitations on the results, which must be recognized. Since only the response of the vessel in sinusoidal waves (regular waves) is being considered in this section, the vessel's responses in the time domain,  $\eta_j(t)$ , will be sinusoidal at the frequency of encounter and can be written as follows:

$$\eta_j(t) = \bar{\eta}_j e^{i\omega_e t} \quad j = 1, 2, \dots, 6 \quad (1)$$

where,  $\bar{\eta}_j$  is the complex amplitude of the vessel's response in the  $j$ -th direction and  $j = 1, 2, 3, \dots, 6$  refer to surge, sway, heave, roll, pitch, and yaw respectively and  $\omega_e$  is the frequency of encounter and equals

$$\omega_0 - \frac{\omega_0^2}{g} U_0 \cos \mu \quad (2)$$

where,  $\mu$  is the angle that the ship moves with respect to the regular waves,  $\omega_0$  is the frequency of the regular wave and  $U_0$  is the speed of the ship. When the ship's speed is zero, which is the case considered here, then  $\omega_e$  equals  $\omega_0$ .

Using the linear theory, the motion of a vessel can be modeled as a generalized spring-mass-damper system. The equations of motion then are written as six simultaneous linear equations in the time domain:

$$\sum_{k=1}^6 (M_{jk} + A_{jk}) \ddot{\eta}_k + \sum_{k=1}^6 B_{jk} \dot{\eta}_k + \sum_{k=1}^6 C_{jk} \eta_k = F_j^H e^{i\omega_0 t} \quad j = 1, 2, \dots, 6 \quad (3)$$

Using the linear theory assumption and Equation (1),  $\ddot{\eta}_k$  and  $\dot{\eta}_k$  can be expressed as:

$$\begin{aligned} \ddot{\eta}_k &= -\omega_e^2 \bar{\eta}_k e^{i\omega_e t} \\ \dot{\eta}_k &= i\omega_e \bar{\eta}_k e^{i\omega_e t} \end{aligned} \quad (4)$$

Substituting Equations (4) into Equation (3) and eliminating the  $e^{i\omega_0 t}$  term we have the system of equations in the frequency domain:

$$\sum_{k=1}^6 \left[ -\omega_o^2 (M_{jk} + A_{jk}) + i\omega_o B_{jk} + C_{jk} \right] \bar{\eta}_k = F_j^H \quad (5)$$

The  $A_{jk}$  terms are called *hydrodynamic added mass*. These terms are in phase with vertical accelerations and physically  $A_{jk}$  represent the force component in the  $j$ -th mode of motion due to the acceleration in the  $k$ -th mode of motion. The  $B_{jk}$  terms correspond to *hydrodynamic damping* in phase with vertical velocity, and physically  $B_{jk}$  represent the force component in the  $j$ -th mode of motion due to the velocity in the  $k$ -th mode of motion. Generally both  $A_{jk}$  and  $B_{jk}$  are functions of frequency. Terms involving the coefficients  $C_{jk}$  are the *restoring forces and moments* representing the net hydrostatic buoyancy effects of the ship motions and similarly  $C_{jk}$  are the hydrostatic restoring force coefficients in the  $j$ -th direction due to  $k$ -th motion. The  $F_j^H$  terms represent the *hydrodynamic wave exciting forces and moments* and are usually subdivided into two components as follows:

$$F_j^H = F_j^I + F_j^D \quad (6)$$

The terms  $F_j^I$  are the complex amplitudes of the wave exciting forces and moments due to *incident* waves, also known as *Froude-Krylov* exciting forces after the classical work on ship rolling done by Froude (1861), and generalized to six degrees of freedom by Krylov (1898). The Froude-Krylov excitations represent the integration of the pressure over the body surface that would exist in the incident wave system if the body were not present. The  $F_j^D$  terms are the complex amplitudes of the wave exciting forces and moments due to *diffracted* waves. The diffraction exciting forces and moments are caused by the diffraction or modification of the incident waves due to the presence of the vessel. The computation of these terms is possible by using the so-called *Haskind Relations*, which are presented later in this Chapter. The Froude-Krylov forces and moments are sometimes used to approximate the total exciting forces since this is a considerably simpler task. This is a good approximation only if the wavelength is much larger than the length of the vessel, such as in the case of a small underwater vehicle in waves. For shorter wavelengths the approximation is increasingly inaccurate because the diffraction forces become significant.

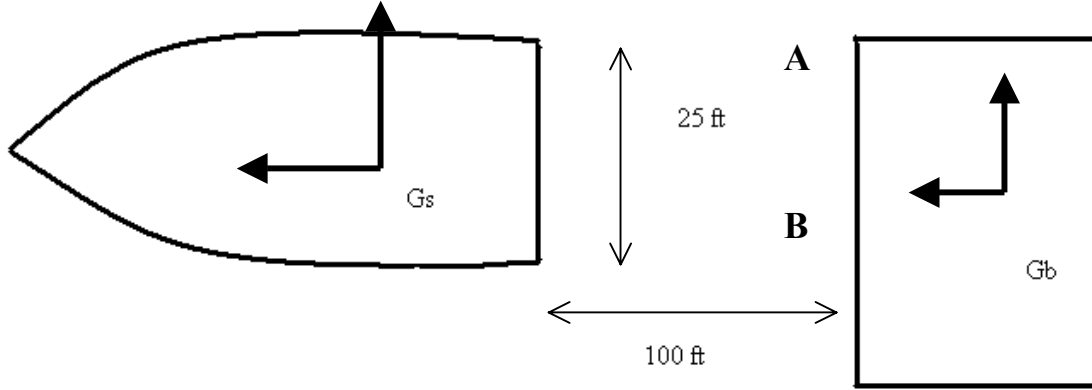


Figure 2. Sketch Defining the Relative Position and Geometry of the CAPE-D and RRDF

Equations (5) hold for a vessel floating in the open sea without any object in the proximity. In the case under consideration here, a ship (CAPE-D or CAPE-H) and a barge (RRDF) are floating very close to one another while maintaining zero speed. The relative position and the geometry of the two vessels can be seen in Figure (2). The short distance between the two vessels stimulates radiative effects. This is the result of the waves striking on one vessel, bouncing off its hull, and then striking the other vessel. Considerable coupling is created between the two vessels, which depends on the relative direction of the incident waves. In order to model accurately the motion of the ship and the barge, coupling coefficients have to be introduced, and the equations of motion of the two vessels have to be solved simultaneously. Now the system is made of twelve equations and twelve unknowns. The twelve unknowns are the six degrees of freedom of the ship and the six degrees of freedom of the barge. In matrix form the system can be represented by a single matrix equation

$$(-\omega_0^2 [M + A] + i\omega_0 [B] + [C])\{\bar{\eta}\} = \{F\} \quad (7)$$

From Equation (7) and by knowing the values of the coefficients and the exciting forces, we can obtain the twelve modes of motion for every frequency as follows:

$$\{\bar{\eta}\} = \left( -\omega_0^2 [M + A] + i\omega_0 [B] + [C] \right)^{-1} \{F\} \quad (8)$$

The solution of the above equation provides the RAO for every motion of the ship's and the barge's center of gravity. Knowing the motions of the gravitational center and by observing the geometry, the vertical motion of every point aboard the ship or the barge can be found as:

$$\xi = \bar{\eta}_3 + \bar{\eta}_4 y - \bar{\eta}_5 x \quad (9)$$

where  $\xi$  is the complex local amplitude of the vertical motion of the given point and  $x, y$  are its coordinates on the body fixed frame.

The determination of the coefficients, the amplitudes of the exciting forces and moments in Equation (8) represents the major task in ship motions calculations. The problem can be simplified by the use of advanced computational techniques as those discussed in the previous section.

## **2. Calculation Of Motions Using a Three Degrees Of Freedom Approximation**

Many times in calculating the motions of a vessel can be assumed that the coupling between the six degrees of freedom is not strong and Equations (5) can be decoupled. This is valid for the case of an unrestrained ship with port/starboard symmetry where the six equations may be uncoupled into two sets of three equations. The vertical-plane or longitudinal motions (surge, heave and pitch) are uncoupled from the horizontal-plane or transverse motions (sway, roll, and yaw). It should be noted that the lack of coupling between the vertical and horizontal modes is a consequence of linear theory. In nonlinear theories such cross-coupling may be present. For some ship motion problems this non-linear coupling can be very important. For example, there is a non-linear heave-roll cross-coupling that can lead to roll instabilities and eventual ship capsizing (Kerwin, 1955) or (Ogilvie and Beck, 1973). Another example is the nonlinear pitch-yaw coupling that results from varying submergence of the bow due to pitch motion (Korvin-Kroukovsky, 1980).

In Ref. [3] a detailed formulation of the equations (using the above approximation) of the ship and the barge, under consideration, can be found. Proximity effects were included into the equations, thereby introducing hydrodynamic coupling between the barge and the ship. The detailed formulation will not be presented here, however some of the results obtained by this method are going to be presented in the results section for comparison.

### 3. Determination Of the Hydrodynamic Forces and Coefficients Using WAMIT

In the present study we utilized results obtained from WAMIT. A short discussion of how WAMIT calculates the coefficients under determination will be presented here. For more details the reader should refer to WAMIT user manual [Ref. 4].

The objective of WAMIT is to evaluate the unsteady hydrodynamic pressure, loads and motions of the body, as well as the induced pressure and velocity in the fluid domain. The free-surface and body-boundary conditions are linearized, the flow is assumed to be potential, free of separation or lifting effects. A harmonic time dependence is adopted. Figure 3 illustrates a three-dimensional body interacting with plane progressive waves in water of finite water depth  $H$

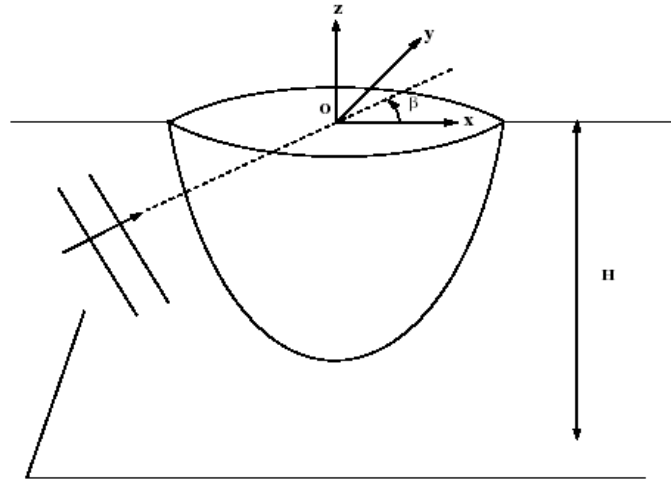


Figure 3. Sketch Defining the Coordinates, Fluid Depth, and Wave-Heading Angle from Ref. [3].

The Cartesian coordinate system  $(x, y, z)$  defined in Figure 3 is stationary relative to the undisturbed position of the free surface and body. Its origin may lie on, above or below the free surface, as the particular application requires. The body geometry input to WAMIT is defined relative to that system. Here, the origin is located on the free surface for the sake of simplicity.

The assumption of a potential flow permits the definition of the flow velocity as the gradient of the velocity potential  $\Phi$  satisfying the Laplace equation

$$\nabla^2 \Phi = 0 \quad (10)$$

in the fluid domain. The harmonic time dependence allows the definition of a complex velocity potential  $\varphi$ , related to  $\Phi$  by

$$\Phi = \text{Re}(\varphi e^{i\omega_0 t}) \quad (11)$$

where  $\text{Re}$  denotes the real part,  $\omega_0$  is the frequency of the incident wave and  $t$  is time. The ensuing boundary-value problem will be expressed in terms of the complex velocity potential,  $\varphi$  with the understanding that the product of all complex quantities with the factor  $e^{i\omega_0 t}$  applies. The linearized form of the free-surface condition is

$$\varphi_z - K\varphi = 0, \quad z = 0 \quad (12)$$

where  $K = \omega^2 / g$ , and  $g$  is the acceleration of gravity. The velocity potential of the incident wave is defined by

$$\varphi_0 = \frac{igA}{\omega} \frac{\cosh[\nu(z+H)]}{\cosh \nu H} e^{-i\nu x \cos \beta - i\nu y \sin \beta} \quad (13)$$

where the wavenumber  $\nu$  is the real root of the dispersion relation

$$\frac{\omega^2}{g} = \nu \tanh \nu H \quad (14)$$

and  $\beta$  is the angle between the direction of propagation of the incident wave and the positive  $x$  axis as defined in Figure 3.

The linearization of the problem permits the decomposition of the velocity potential into the radiation and diffraction components

$$\varphi = \varphi_R + \varphi_D \quad (15)$$

$$\varphi_R = i\omega \sum_{j=1}^6 \eta_j \varphi_j \quad (16)$$

$$\varphi_D = \varphi_0 + \varphi_7 \quad (17)$$

The constants  $\eta_j$  denote the complex amplitudes of the body oscillatory motion in its six rigid-body degrees of freedom, and  $\varphi_j$  the corresponding unit-amplitude radiation potentials. The velocity potential  $\varphi_7$  represents the *scattered* disturbance of the incident wave by the body fixed at its undisturbed position. The sum (17) will refer to as the *diffraction* potential  $\varphi_D$ .

On the undisturbed position of the body boundary, the radiation and diffraction potentials are subject to the conditions

$$\varphi_{,jn} = n_j \quad (18)$$

$$\varphi_{,Dn} = 0 \quad (19)$$

where  $(n_1, n_2, n_3) = \mathbf{n}$  and  $(n_4, n_5, n_6) = \mathbf{x} \times \mathbf{n}$ ,  $\mathbf{x} = (x, y, z)$ . The unit vector  $\mathbf{n}$  is normal to the body boundary and *points out of the fluid domain*.

In WAMIT the boundary value problems (10)-(19) are solved by using Green's theorem to derive integral equations for the radiation and diffraction velocity potentials on the body boundary. The integral equation satisfied by the radiation velocity potentials  $\varphi_j$  on the body boundary takes the form

$$2\pi\varphi_j(x) + \iint_{S_b} \varphi_j(\xi) \frac{\partial G(\xi; x)}{\partial n_\xi} d\xi = \iint_{S_b} n_j G(\xi; x) d\xi \quad (20)$$

where  $S_b$  denotes body wetted surface at calm water and  $G(x; \xi)$  is the Green function.

The corresponding equation for the total diffraction velocity potential  $\varphi_D$  is

$$2\pi\varphi_D(x) + \iint_{sb} \varphi_D(\xi) \frac{\partial G(\xi; x)}{\partial n_\xi} d\xi = 4\pi\varphi_0(x) \quad (21)$$

The diffraction potential may also be obtained from Equation (17) after solving for the scattered potential  $\varphi_\gamma$ . The equation for the scattered velocity potential is

$$2\pi\varphi_\gamma(x) + \iint_{sb} \varphi_\gamma(\xi) \frac{\partial G(\xi; x)}{\partial n_\xi} d\xi = -\iint_{sb} \frac{\partial \varphi_0(\xi)}{\partial n} G(\xi; x) d\xi \quad (22)$$

The Green function  $G(x; \xi)$  is referred to as the wave source potential. It is the velocity potential at the point  $\mathbf{x}$  due to a point source of strength  $-4\pi$  located at point  $\xi$ . It satisfies the free-surface and radiation conditions, and in infinite water depth is defined by

$$G(x; \xi) = \frac{1}{r} + \frac{1}{r'} + \frac{2K}{\pi} \int_0^\infty dk \frac{e^{k(z+\xi)}}{k-K} J_0(kR) \quad (23)$$

$$r^2 = (x-\xi)^2 + (y-\eta)^2 + (z-\zeta)^2 \quad (24)$$

$$r'^2 = (x-\xi)^2 + (y-\eta)^2 + (z+\zeta)^2 \quad (25)$$

where  $J_0(x)$  is the Bessel function of zero order. In finite depth, the Green function is defined by

$$G(x; \xi) = \frac{1}{r} + \frac{1}{r''} + 2 \int_0^\infty dk \frac{(k+K) \cosh k(z+H) \cosh k(\zeta+H)}{k \sinh kH - K \cosh kH} e^{-kH} J_0(kR) \quad (26)$$

$$(r'')^2 = (x-\xi)^2 + (y-\eta)^2 + (z+\zeta+2H)^2 \quad (27)$$

In both expressions (23) and (26) the Fourier  $k$ -integration is intended above the pole on the real axis in order to enforce the radiation condition. Efficient algorithms for the evaluation of the infinite and finite-depth wave-source potentials and their spatial derivatives have been developed. Provision has been made in WAMIT to permit the logarithmic singularity and its derivatives to be integrated analytically in the solution of the integral equations when the source and field points are close to each other and to the free surface.



As already mentioned in the above section, WAMIT utilizes the panel method for discretization. This allows for numerical solution of the above integral equations. The mean position of the body's wetted surface is approximated by a collection of quadrilaterals. Four vertices, lying on the body's surface, define each quadrilateral. In general the quadrilaterals defined above are not plane, but if a sufficiently fine discretization is used for the boundary surface with continuous curvature, each element will approach a plane surface.

The above solution of the velocity and scattering potentials allows WAMIT to calculate the coefficients of Equation (5), which can be written in matrix form as

$$(-\omega_0^2 [M + A] + i\omega_0 [B] + [C])\{\bar{\eta}\} = \{F\} \quad (28)$$

where  $M$  is the inertia matrix defined as

$$M = \begin{bmatrix} m & 0 & 0 & 0 & mz_g & -my_g \\ 0 & m & 0 & -mz_g & 0 & mx_g \\ 0 & 0 & m & my_g & -mx_g & 0 \\ 0 & -mz_g & my_g & I_{11} & I_{12} & I_{13} \\ mz_g & 0 & -mx_g & I_{21} & I_{22} & I_{23} \\ -my_g & mx_g & 0 & I_{31} & I_{32} & I_{33} \end{bmatrix} \quad (29)$$

$m$  is the body mass,  $(x_g, y_g, z_g)$  are the coordinates of the center of gravity and  $I_{ij}$  are the moments of inertia in terms of the corresponding radii of gyration.

The forces and other quantities evaluated by WAMIT are output in a standard nondimensional form, in terms of the appropriate combinations of the water density  $\rho$ , the acceleration of gravity  $g$ , the incident-wave amplitude  $A$ , the frequency  $\omega$ , and the length scale  $L$ .

All hydrostatic data can be expressed in the form of surface integrals over the mean body wetted surface  $S_b$ , by virtue of Gauss' divergence theorem. So the mass can be found by

$$m = \rho \nabla \quad (30)$$

where  $\nabla$  is the underwater volume and can be calculated by

$$\nabla = -\iint_{S_b} n_1 x dS = -\iint_{S_b} n_2 y dS = -\iint_{S_b} n_3 z dS \quad (31)$$

The elements of the *hydrostatic and gravitational* coefficients matrix  $C$  in Equation (28) can be found as follows:

$$\begin{aligned} C(3,3) &= \rho g \iint_{S_b} n_3 dS \\ C(3,4) &= \rho g \iint_{S_b} y n_3 dS \\ C(3,5) &= -\rho g \iint_{S_b} x n_3 dS \\ C(4,4) &= \rho g \iint_{S_b} y^2 n_3 dS + \rho g \nabla z_b - m g z_g \\ C(4,5) &= -\rho g \iint_{S_b} x y n_3 dS \\ C(4,6) &= -\rho g \nabla x_b + m g x_g \\ C(5,5) &= \rho g \iint_{S_b} x^2 n_3 dS + \rho g \nabla z_b - m g z_g \\ C(5,6) &= -\rho g \nabla y_b + m g y_g \end{aligned} \quad (32)$$

WAMIT's output format is in non-dimensional form that is defined as:

$$\begin{aligned} \bar{C}(3,3) &= C(3,3) / \rho g L^2 \\ \bar{C}(3,4) &= C(3,4) / \rho g L^3 \\ \bar{C}(3,5) &= C(3,5) / \rho g L^3 \\ \bar{C}(4,4) &= C(4,4) / \rho g L^4 \\ \bar{C}(4,5) &= C(4,5) / \rho g L^4 \\ \bar{C}(4,6) &= C(4,6) / \rho g L^4 \\ \bar{C}(5,5) &= C(5,5) / \rho g L^4 \\ \bar{C}(5,6) &= C(5,6) / \rho g L^4 \end{aligned} \quad (33)$$

where  $C(i,j) = C(j,i)$  for all  $i, j$  except for  $C(4,6)$  and  $C(5,6)$ . For all other values of the indices  $i, j$ ,  $C(i,j) = 0$ . In particular,  $C(6,4) = C(6,5) = 0$ .

The *added mass* and *added damping* coefficients of the matrices  $A$  and  $B$  of Equation (28) can be found by the following equations:

$$A_{ij} - \frac{i}{\omega} B_{ij} = \rho \iint_{S_b} n_i \phi_j dS \quad (34)$$

in the non-dimensional output form

$$\bar{A}_{ij} = \frac{A_{ij}}{\rho L^k} \quad \bar{B}_{ij} = \frac{B_{ij}}{\rho L^k \omega} \quad (35)$$

where  $k = 3$  for  $i, j = 1, 2, 3$ ,  $k = 4$  for  $i = 1, 2, 3, j = 4, 5, 6$  or  $i = 4, 5, 6, j = 1, 2, 3$  and  $k = 5$  for  $i, j = 4, 5, 6$ .

The exciting forces are calculated both from the Haskind Relations

$$X_i = -i\omega\rho \iint_{S_b} \left( n_i \phi_0 - \phi_i \frac{\partial \phi_0}{\partial n} \right) dS \quad (36)$$

and from direct integration of the hydrodynamic pressure

$$X_i = -i\omega\rho \iint_{S_b} n_i \phi_D dS \quad (37)$$

The non-dimensional output format is defined as:

$$\bar{X}_i = \frac{X_i}{\rho g A L^m} \quad (38)$$

where  $m = 2$  for  $i = 1, 2, 3$  and  $m = 3$  for  $i = 4, 5, 6$ .

#### D. RESULTS

Numerical results are presented for the Cape-D class of ships and the RRDF2000 (Roll-On Roll-Off Discharge Facility). The RRDF is made up of a number of interconnected modules, in an asymmetrical way, as can be seen in Figure 4. Each module has 8x8x40 ft nominal dimensions, and floats at an approximate draft of 2 ft. The RRDF is placed astern of the Cape-D ship which is equipped with a stern ramp only. The Cape-D ship has a length of 634 ft, beam 97 ft, nominal draft 32.4 ft, and displaces approximately 36,000 tons. This ship is part of the Ready Reserve Force and is one of the main ships used for dry cargo transfer by the Military Sealift Command's (MSC) Strategic Sealift Forces. A picture of the ship is shown in Figure 5. Raw WAMIT results for this configuration in terms of added mass, damping, hydrostatic, and wave exciting forces were provided by NSWCC, Carderock Division. Calculations were performed for 30

frequencies ranging from 0.3 to 2.5 rad/sec and for 24 headings, 0 to 345 degrees in 15 degree increments. We remind the reader that, as shown in Figure 3, 0 deg corresponds to following (astern) seas, 180 deg to head seas, 90 deg to starboard beam seas, and 270 deg to port beam seas.

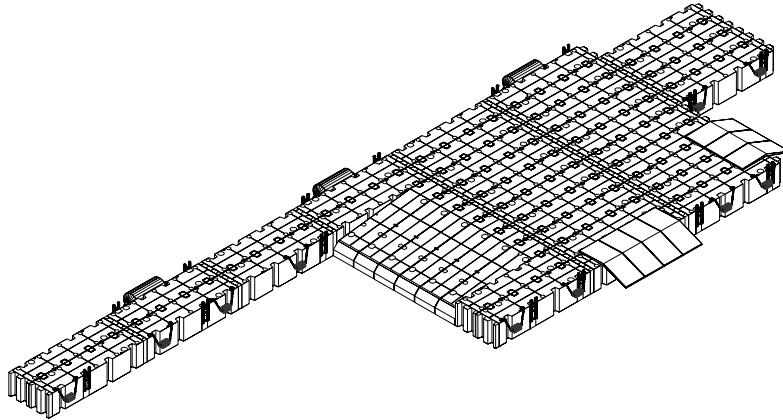


Figure 4. An Isometric View of the RRDF.



Figure 5. Typical Views of the Cape-D Ship Class.

Regular wave results are presented in Figures A1 through A44 in Appendix A. Figures A1 and A2 show the heave response for the Cape-D per unit wave amplitude for various wave directions. It should be emphasized that, at this point, the ramp is not included in the formulation. Therefore, there is no structural coupling between the two bodies, although of course hydrodynamic coupling is fully included. The results are port/starboard symmetric. This shows that ship response is unaffected by the presence of the RRDF, a result which is consistent with physical intuition. Figures A3 and A4 show the corresponding heave response for the RRDF. It can be seen that in this case, a slight asymmetry between port beam and starboard beam seas has developed. This is due to the asymmetric nature of the RRDF as shown in Figure 4. Also, heave response is less for head seas than following seas, a result which is partially due to the sheltering of the RRDF by the ship. As expected (Ref [8]) the roll motion for a large monohull, as the CAPE-D, is lightly damped especially for low frequencies. This explains the large values for the ship's roll motion at wave periods greater than 18 seconds. Corresponding plots, with similar conclusions, for the roll and pitch responses are shown in Figures A5 through A12. Only heave, pitch, and roll motions are presented since these motions determine the vertical motion at the interface between ship and RRDF, which is analyzed in the following chapters.

Figures A13 through A28 are presented in order to gain some understanding on the hydrodynamic coupling aspects of the motions of the two bodies. These figures show a comparison between the full 12 degrees of freedom (6 from each body) solutions and simplified reduced approximations where only vertical plane motions are considered. The latter approximation is often utilized in seakeeping studies, since it is generally accepted that linear vertical plane motions (heave, pitch, and roll) are decoupled from horizontal plane motions (sway, yaw, and surge). Both the amplitude and the phase angle are included in the figures. Based on this set of figures, the following conclusions can be made:

1. Ship vertical/horizontal plane coupling is negligible for following seas, and it is small for head seas.
2. Ship vertical/horizontal plane coupling can be significant for beam seas.

3. RRDF coupling between horizontal and vertical plane motions is significant throughout the wave direction and frequency range and cannot be neglected. This means that any attempts to simplify the motion of the RRDF into an equivalent low order dynamical system will have to proceed very cautiously. In this thesis, we will continue to utilize the full 12-degree of freedom hydrodynamic model.

Figures A29 through A44 present the vertical motion at the two connection points between the ship and the RRDF. Point A is the starboard connection point, and point B is at port. These motions are used as the basis for the structural coupling in the Ship/ramp/RRDF system and also form some of the primary Response Amplitude Operators (RAO) that are further studied in the next chapters. The phase angle for the Ship/RRDF vertical motions is also shown in the figures, in order to explain the fact that the relative motion between the two points is not simply the difference between the amplitudes of the two vertical motions. Points where the relative motion experiences a peak will become very important in the subsequent chapters, since they will relate to excessive twist and stresses in the ramp.

THIS PAGE INTENTIONALLY LEFT BLANK

### **III. RAMP MODELING**

#### **A. INTRODUCTION**

Following the numerical solution for the motions of the ship and the barge, the formulation of the mathematical model of the ramp between the ship and the barge must be done. Previous work done on this subject has shown shortcomings that have to be overcome. In Ref. [3] a simplified second order system was used to simulate the ramp, also the solution of the barge and the ship motion was found using the three degrees of freedom hydrodynamic approximation described in the previous chapter. In Ref. [5], an analytical model for the ramp was created by using Timoshenko's plate theory but a simplified spring-mass-damper system was used for the barge. In Ref. [6] a detailed finite element model of the ramp was used to show the influence of the roll motion in the stress profile of the ramp, but the plate was not directly coupled with the barge and the ship.

#### **B. RAMP MODELING USING FINITE ELEMENT METHOD**

In this work, we will approximate the ramp by a rectangular plate with uniform properties. This approximation is valid here since our primary concern is to establish the level of influence that a structural component such as a ramp has on a floating body such as the RRDF. This approximation allows us to use relatively simple algorithms and computer programs that can be easily adjusted in order to examine different coupling conditions. For comparison purposes only the relative magnitudes of the stresses are of interest for the different coupling conditions, and not their exact values. Once the ramp/RRDF influence levels have been established, one could use more detailed finite element techniques such as those presented in [6] for accurate stress calculations, or the strategies developed in [5] for active control studies.

A finite element model for the ramp was created using shear deformable plate elements, as described in Ref. [7]. The Mindlin/Reissner theory was utilized for the formulation of the stiffness matrix. This theory includes the effect of the transverse shear deformation like the Timoshenko beam theory. Hence, a plane normal to the midplane of the plate before the deformation does not remain normal to the midplane any longer after the deformation. An expression for the internal energy of the shear deformable plate



should include transverse shear energy and bending energy as well. The internal energy is expressed as:

$$U = \frac{1}{2} \int_V \{\sigma_b\}^T \{\varepsilon_b\} dV + \frac{\kappa}{2} \int_V \{\sigma_s\}^T \{\varepsilon_s\} dV \quad (39)$$

where

$$\{\sigma_b\} = \{\sigma_x \quad \sigma_y \quad \tau_{xy}\}^T \quad (40)$$

$$\{\varepsilon_b\} = \{\varepsilon_x \quad \varepsilon_y \quad \gamma_{xy}\}^T \quad (41)$$

are the bending stress and strain components while,

$$\{\sigma_s\} = \{\tau_{xz} \quad \tau_{yz}\}^T \quad (42)$$

$$\{\varepsilon_s\} = \{\gamma_{xz} \quad \gamma_{yz}\}^T \quad (43)$$

are the transverse shear components. Additionally,  $\kappa$  is the shear energy correction factor equal to  $\frac{5}{6}$  and  $V$  indicates integration over the volume.

Substitution of the equations (40)-(43) into (39) yields

$$U = \frac{1}{2} \int_V \{\varepsilon_b\}^T [D_b] \{\varepsilon_b\} dV + \frac{\kappa}{2} \int_V \{\varepsilon_s\}^T [D_s] \{\varepsilon_s\} dV \quad (44)$$

in which

$$[D_b] = \frac{E}{1-\nu^2} \begin{bmatrix} 1 & \nu & 0 \\ \nu & 1 & 0 \\ 0 & 0 & \frac{1-\nu}{2} \end{bmatrix} \quad (45)$$

is the constitutive equation for the plane stress condition and

$$[D_s] = \begin{bmatrix} G & 0 \\ 0 & G \end{bmatrix} \quad (46)$$

Further,  $G$  is the shear modulus and  $\nu$  is the Poisson's Ratio.

Next, in order to derive the element stiffness matrix for the shear deformable plate, the strains need to be expressed in terms of nodal variables. The displacements along the  $x, y$  plane are given as

$$u = -z\theta_x(x, y) \quad (47)$$

$$v = -z\theta_y(x, y) \quad (48)$$

and the transverse displacement along the  $z$  axis is

$$w = w(x, y) \quad (49)$$

where  $\theta_x$  and  $\theta_y$  are the rotations of the midplane about the  $y$  and  $x$  axes respectively.

The midplane is assumed to have no inplane deformation. For the shear deformable plate,

$$\theta_x = \frac{\partial w}{\partial x} - \gamma_{xz} \quad (50)$$

$$\theta_y = \frac{\partial w}{\partial y} - \gamma_{yz} \quad (51)$$

where  $\gamma$  is the angle caused by the transverse shear deformation.

The displacement  $w$  and the slope  $\theta$  are independent. Because of their independence we need shape functions to interpolate them independently. As a result, the shear deformable plate element requires  $C^0$  compatibility. The isoparametric shape functions,  $H_i$ , are used for the plate element formulation (Ref. [7])

where

$$H_1(\xi, \eta) = \frac{1}{4}(1-\xi)(1-\eta) \quad (52)$$

$$H_2(\xi, \eta) = \frac{1}{4}(1+\xi)(1-\eta) \quad (53)$$

$$H_3(\xi, \eta) = \frac{1}{4}(1+\xi)(1+\eta) \quad (54)$$

$$H_4(\xi, \eta) = \frac{1}{4}(1-\xi)(1+\eta) \quad (55)$$

and  $\xi, \eta$  are the natural coordinates of the isoparametric element. A point  $(\xi, \eta)$  within the natural element is mapped into a point  $(x, y)$  within the physical element, using the shape function described above, as

$$x = \sum_{i=1}^4 H_i(\xi, \eta) x_i \quad (56)$$

$$y = \sum_{i=1}^4 H_i(\xi, \eta) y_i \quad (57)$$

Then the transverse displacement and the slopes are interpolated as

$$w = \sum_{i=1}^n H_i(\xi, \eta) w_i \quad (58)$$

$$\theta_x = \sum_{i=1}^n H_i(\xi, \eta) (\theta_x)_i \quad (59)$$

$$\theta_y = \sum_{i=1}^n H_i(\xi, \eta) (\theta_y)_i \quad (60)$$

Here  $n$  is the number of nodes per element and the same shape functions are used for the displacement and slope interpolations. In the formulation presented here, bilinear isoparametric shape functions are used for simplicity. For more information about bilinear isoparametric elements and shape functions the interested reader should read the corresponding chapter in Ref. [7]. The bilinear isoparametric elements have four nodes per element. So the total degrees of freedom per element are twelve.

Both bending and shear strains for each element are computed from displacements

$$\{\epsilon_b\} = -z[B_b]\{d^e\} \quad (61)$$

$$\{\epsilon_s\} = [B_s]\{d^e\} \quad (62)$$

where

$$[B_b] = \begin{bmatrix} \frac{\partial H_1}{\partial x} & 0 & 0 & \frac{\partial H_2}{\partial x} & 0 & 0 & \frac{\partial H_3}{\partial x} & 0 & 0 & \frac{\partial H_4}{\partial x} & 0 & 0 \\ 0 & \frac{\partial H_1}{\partial x} & 0 & 0 & \frac{\partial H_2}{\partial x} & 0 & 0 & \frac{\partial H_3}{\partial x} & 0 & 0 & \frac{\partial H_4}{\partial x} & 0 \\ \frac{\partial H_1}{\partial x} & \frac{\partial H_1}{\partial x} & 0 & \frac{\partial H_2}{\partial x} & \frac{\partial H_2}{\partial x} & 0 & \frac{\partial H_3}{\partial x} & \frac{\partial H_3}{\partial x} & 0 & \frac{\partial H_4}{\partial x} & \frac{\partial H_4}{\partial x} & 0 \end{bmatrix} \quad (63)$$

$$[B_s] =$$

$$\begin{bmatrix} -H_1 & 0 & \frac{\partial H_1}{\partial x} & -H_2 & 0 & \frac{\partial H_2}{\partial x} & -H_3 & 0 & \frac{\partial H_3}{\partial x} & -H_4 & 0 & \frac{\partial H_4}{\partial x} \\ 0 & -H_1 & \frac{\partial H_1}{\partial y} & 0 & -H_2 & \frac{\partial H_2}{\partial y} & 0 & -H_3 & \frac{\partial H_3}{\partial y} & 0 & -H_4 & \frac{\partial H_4}{\partial y} \end{bmatrix} \quad (64)$$

and

$$\{d^e\} =$$

$$\left\{ (\theta_x)_1 \quad (\theta_y)_1 \quad w_1 \quad (\theta_x)_2 \quad (\theta_y)_2 \quad w_2 \quad (\theta_x)_3 \quad (\theta_y)_3 \quad w_3 \quad (\theta_x)_4 \quad (\theta_y)_4 \quad w_4 \right\}^T \quad (65)$$

and

Finally, substitution of Equations (61) and (62) into the energy expression (44) yields for each plate element

$$U =$$

$$\frac{1}{2} \{d^e\}^T \int_{\Omega^e} \int_z [B_b]^T [D_b] [B_b] dz d\Omega \{d^e\} + \frac{\kappa}{2} \{d^e\}^T \int_{\Omega^e} \int_z [B_s]^T [D_s] [B_s] dz d\Omega \{d^e\} \quad (66)$$

As a result, the element stiffness matrix for the plate bending can be expressed as

$$[K^e] = \frac{t^3}{12} \int_{\Omega^e} [B_b]^T [D_b] [B_b] |J| d\Omega + \kappa t \int_{\Omega^e} [B_s]^T [D_s] [B_s] |J| d\Omega \quad (67)$$

where  $t$  is the plate thickness and  $J$  is the Jacobian matrix to transform from the natural coordinates  $(\xi, \eta)$  to physical coordinates  $(x, y)$ .

The mass matrix for each plate element can be found (Ref. [7]) as

$$[M^e] = \int_{\Omega^e} \rho A [H]^T [H] |J| d\Omega \quad (68)$$

where  $l$  is the length of the individual element,  $\rho$  is the mass density of the ramp,  $A$  is the cross sectional area of the ramp and  $[H]$  is the diagonal matrix of the shape functions. The above matrix is called the consistent mass matrix. A more computational efficient form of the above mass matrix is the lumped mass matrix, which is a diagonal matrix and can be developed using a method described in Ref. [7]. In the case of the shear deformable element the lumped mass matrix is as follows

$$[M^e] = \frac{\rho A}{4} \begin{bmatrix} 0 & 0 & 0 & 0 & 0 & 0 & 0 & 0 & 0 & 0 & 0 & 0 \\ 0 & 0 & 0 & 0 & 0 & 0 & 0 & 0 & 0 & 0 & 0 & 0 \\ 0 & 0 & 1 & 0 & 0 & 0 & 0 & 0 & 0 & 0 & 0 & 0 \\ 0 & 0 & 0 & 0 & 0 & 0 & 0 & 0 & 0 & 0 & 0 & 0 \\ 0 & 0 & 0 & 0 & 0 & 0 & 0 & 0 & 0 & 0 & 0 & 0 \\ 0 & 0 & 0 & 0 & 0 & 1 & 0 & 0 & 0 & 0 & 0 & 0 \\ 0 & 0 & 0 & 0 & 0 & 0 & 0 & 0 & 0 & 0 & 0 & 0 \\ 0 & 0 & 0 & 0 & 0 & 0 & 0 & 0 & 0 & 0 & 0 & 0 \\ 0 & 0 & 0 & 0 & 0 & 0 & 0 & 0 & 1 & 0 & 0 & 0 \\ 0 & 0 & 0 & 0 & 0 & 0 & 0 & 0 & 0 & 0 & 0 & 0 \\ 0 & 0 & 0 & 0 & 0 & 0 & 0 & 0 & 0 & 0 & 0 & 0 \\ 0 & 0 & 0 & 0 & 0 & 0 & 0 & 0 & 0 & 0 & 0 & 1 \end{bmatrix} \quad (69)$$

Using a program in MATLAB the mass matrix and the stiffness matrix of the whole ramp can be found for every boundary condition that the user specifies. The mesh of the finite element model consisted of 100 elements as can be seen in Figure (6). A total of 121 nodes were used with a total of 363 degrees of freedom.

### C. VALIDATION OF THE RAMP MODEL

The finite element model of the ramp described above approximates the complicated structure of the physical ramp, with a plate of uniform properties. The thickness and the modulus of elasticity of the model should be selected so that the natural frequencies of the model are comparable with the natural frequencies of the physical ramp. In Ref. [6] a complicated finite element model was validated and the natural frequencies were found for various boundary conditions. Those natural frequencies were used as reference for the selection of the appropriate thickness and modulus of elasticity

using the same boundary conditions. The natural frequencies of the ramp model were calculated by solving the eigenvalue-eigenvector problem

$$([K] - \omega^2 [M])\{\bar{d}\} = 0, \quad (70)$$

where  $\omega$  is the natural frequency in radians per second and  $\{\bar{d}\}$  is the corresponding mode shape. Different ramp thickness and Young's moduli were tested, and the corresponding natural frequencies were found. The natural frequencies obtained from the solution of the above problem can be seen in the Table 1.

<b>From Ref. [6] case 5</b>	<b>E = 39*10<sup>6</sup> psi, t = 10 in</b>	<b>E = 29*10<sup>6</sup> psi, t = 20 in</b>	<b>E = 40*10<sup>6</sup> psi, t = 20 in</b>	<b>E = 49*10<sup>6</sup> psi, t = 25 in</b>
2.1	0.37	0.639	0.75	0.65
2.62	1.22	2.1	2.47	2.64
3.45	1.34	2.28	2.68	3.45
6.65	2.6	4.46	5.24	6.04

Table 1. Natural Frequencies of the Ramp Model.

From the above results it is obvious that we cannot model exactly a complicated structure like the CAPE-D ramp as a plate, with uniform properties. Detailed finite element models are more appropriate for that purpose. Since the purpose of this work is to establish the interaction between the ramp and the RRDF and not to find the exact response and stress values of the ramp, the plate model can approximate with acceptable accuracy the physical ramp. The only exception to this is the first natural frequency, which corresponds to longitudinal bending. A closer look at the physical structure of the ramp reveals that the ramp is highly reinforced longitudinally by stiffeners that run throughout the whole length of the ramp. This explains the difference in the first natural frequency in bending. Based on the above observations, we select the last case presented in Table 1 as the baseline ramp for the current work.

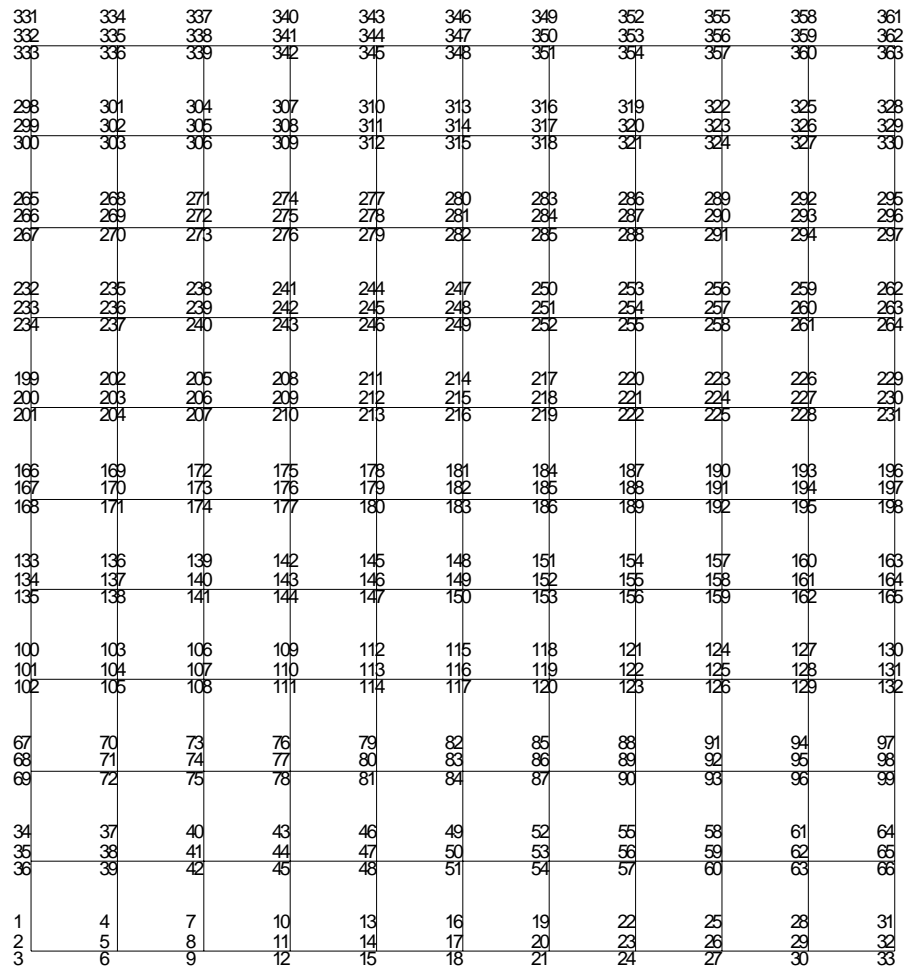


Figure 6. Mesh of the Ramp Finite Element Model Showing the Numbering of the DOFs.

## IV. COUPLING BETWEEN SHIP RAMP AND BARGE MODELS

### A. INTRODUCTION

In section II the mathematical models of the ship and the barge in regular waves were created. In section III the finite element of the ramp was created and validated. From those models the mass, stiffness, and damping matrices of each model can be found. Since damping was not considered for the ramp, its damping matrix is zero. Previous studies (see for example Ref. [5]), have suggested that active or passive motion compensation can reduce the motions and the stresses of the ramp. One such coupling condition for motion and stress reduction is the use of a spring-damper combination at the two ends of the ramp, between the barge and the ramp. This coupling method is used in the current work. The coupling methodology is, however, general enough so that other coupling conditions can be also used. A sketch of the system can be seen in Figure 7.

### B. COUPLING BETWEEN SHIP, RAMP, BARGE

The equations of motion for the ship, the ramp and the barge in the time domain are

$$[M_s + A_s]\{\ddot{\eta}_s\} + [B_s]\{\dot{\eta}_s\} + [C_s]\{\eta_s\} = \{F_{ws}\} \quad (71)$$

$$[M_p]\{\ddot{d}_p\} + [C_p]\{\dot{d}_p\} + [K_p]\{d_p\} = \{F_p\} \quad (72)$$

$$[M_b + A_b]\{\ddot{\eta}_b\} + [B_b]\{\dot{\eta}_b\} + [C_b]\{\eta_b\} = \{F_{wb}\} \quad (73)$$

where the subscripts s, b, and p correspond to the ship, the barge, and the ramp respectively. The matrices in the ship and barge equations were defined in section II and the matrices in the ramp equation were obtained from the finite element model as described in section III. The matrices  $F_{wb}$  and  $F_{ws}$  represent the wave forces acting on the barge and on the ship. Note that the damping matrix for the ramp is zero. Equations (71) and (73) have been solved as a system of twelve equations with twelve unknowns in section II.

Since the ship is very heavy compared to either the ramp or the barge, its inertia forces are orders of magnitude greater than the barge's, it is reasonable to assume that its



motions are not going to be affected by the dynamic forces transmitted through the ramp. Therefore, the motions of the ship can be considered as uncoupled from the ramp and the barge and they are going to be given by the solution obtained in section II.

### 1. Spring–Damper Coupling Condition

The main coupling condition considered in this work is the spring-damper case. Between the ramp and the barge we assume the existence of two sets of spring-damper combinations attached to the end points of the ramp, as can be seen in Figure 7 in Appendix B. From the barge's equations of motion, the heave, roll and pitch equations are going to be affected from the coupling like follow:

#### Heave equation:

$$\begin{aligned}
 & \left( \begin{matrix} M_{31b} + A_{31b} & M_{32b} + A_{32b} & M_{33b} + A_{33b} & M_{34b} + A_{34b} & M_{35b} + A_{35b} & M_{36b} + A_{36b} \end{matrix} \right) \left\{ \begin{matrix} \ddot{\eta}_{1b} \\ \ddot{\eta}_{2b} \\ \ddot{\eta}_{3b} \\ \ddot{\eta}_{4b} \\ \ddot{\eta}_{5b} \\ \ddot{\eta}_{6b} \end{matrix} \right\} + \\
 & \left( \begin{matrix} B_{31b} & B_{32b} & B_{33b} & B_{34b} & B_{35b} & B_{36b} \end{matrix} \right) \left\{ \begin{matrix} \dot{\eta}_{1b} \\ \dot{\eta}_{2b} \\ \dot{\eta}_{3b} \\ \dot{\eta}_{4b} \\ \dot{\eta}_{5b} \\ \dot{\eta}_{6b} \end{matrix} \right\} + \left( \begin{matrix} C_{31b} & C_{32b} & C_{33b} & C_{34b} & C_{35b} & C_{36b} \end{matrix} \right) \left\{ \begin{matrix} \eta_{1b} \\ \eta_{2b} \\ \eta_{3b} \\ \eta_{4b} \\ \eta_{5b} \\ \eta_{6b} \end{matrix} \right\} = \\
 & = (F_{3wb}) - (\xi_A - w_A)k_A - (\xi_B - w_B)k_B - (\dot{\xi}_A - \dot{w}_A)c_A - (\dot{\xi}_B - \dot{w}_B)c_B
 \end{aligned}$$

the right hand side becomes

$$LHS = (F_{3wb}) - \xi_A k_A - \xi_B k_B - \dot{\xi}_A c_A - \dot{\xi}_B c_B + w_A k_A + w_B k_B + \dot{w}_A c_A + \dot{w}_B c_B \quad (74)$$

where  $\xi$  was defined in Equation (9) and  $k_A, k_B, c_A, c_B$  are the spring and damping coefficients at points  $A$  and  $B$ , respectively. By substituting the value of  $\xi$  in Equation (74) we get

$$\begin{aligned}
LHS = & (F_{wb}) - \eta_{3b}(k_A + k_B) - \eta_{4b}(k_A y_A + k_B y_B) - \eta_{5b}(-x_A k_A - x_B k_B) - \\
& - \dot{\eta}_{3b}(c_A + c_B) - \dot{\eta}_{4b}(c_A y_A + c_B y_B) - \dot{\eta}_{5b}(-x_A c_A - x_B c_B) + \\
& + w_A k_A + w_B k_B + \dot{w}_A c_A + \dot{w}_B c_B
\end{aligned} \tag{75}$$

Equation (75) can be written as

$$\{M_{3b} + A_{3b}\}\{\ddot{\eta}_b\} + \{B_{3bp}\}\{\dot{\eta}_b\} + \{C_{3bp}\}\{\eta_b\} - w_A k_A - w_B k_B - \dot{w}_A c_A - \dot{w}_B c_B = (F_{3wb}) \tag{76}$$

where

$$\{C_{3bp}\} = \begin{Bmatrix} C_{31} & C_{32} & C_{33} + k_A + k_B & C_{34} + k_A y_A + k_B y_B & C_{35} - k_A x_A - k_B x_B & C_{36} \end{Bmatrix} \tag{77}$$

and

$$\{B_{3bp}\} = \begin{Bmatrix} B_{31} & B_{32} & B_{33} + c_A + c_B & B_{34} + c_A y_A + c_B y_B & B_{35} - c_A x_A - c_B x_B & B_{36} \end{Bmatrix} \tag{78}$$

### Roll Equation:

$$\begin{aligned}
& \begin{pmatrix} M_{41b} + A_{41b} & M_{42b} + A_{42b} & M_{43b} + A_{43b} & M_{44b} + A_{44b} & M_{45b} + A_{45b} & M_{46b} + A_{46b} \end{pmatrix} \begin{Bmatrix} \ddot{\eta}_{1b} \\ \ddot{\eta}_{2b} \\ \ddot{\eta}_{3b} \\ \ddot{\eta}_{4b} \\ \ddot{\eta}_{5b} \\ \ddot{\eta}_{6b} \end{Bmatrix} + \\
& \begin{pmatrix} B_{41b} & B_{42b} & B_{43b} & B_{44b} & B_{45b} & B_{46b} \end{pmatrix} \begin{Bmatrix} \dot{\eta}_{1b} \\ \dot{\eta}_{2b} \\ \dot{\eta}_{3b} \\ \dot{\eta}_{4b} \\ \dot{\eta}_{5b} \\ \dot{\eta}_{6b} \end{Bmatrix} + \begin{pmatrix} C_{41b} & C_{42b} & C_{43b} & C_{44b} & C_{45b} & C_{46b} \end{pmatrix} \begin{Bmatrix} \eta_{1b} \\ \eta_{2b} \\ \eta_{3b} \\ \eta_{4b} \\ \eta_{5b} \\ \eta_{6b} \end{Bmatrix} = \\
& = (F_{4wb}) - (\xi_A - w_A)k_A y_A - (\xi_B - w_B)k_B y_B - (\dot{\xi}_A - \dot{w}_A)c_A y_A - (\dot{\xi}_B - \dot{w}_B)c_B y_B
\end{aligned}$$

the right hand side becomes

$$LHS = (F_{4wb}) - \xi_A k_A y_A - \xi_B k_B y_B - \dot{\xi}_A c_A y_A - \dot{\xi}_B c_B y_B + \\ + w_A k_A y_A + w_B k_B y_B + \dot{w}_A c_A y_A + \dot{w}_B c_B y_B \quad (79)$$

After massaging equation (79) becomes

$$\{M_{4b} + A_{4b}\}\{\ddot{\eta}_b\} + \{B_{4bp}\}\{\dot{\eta}_b\} + \{C_{4bp}\}\{\eta_b\} - w_A k_A y_A - w_B k_B y_B - \dot{w}_A c_A y_A - \dot{w}_B c_B y_B \\ = (F_{4wb}) \quad (80)$$

where

$$\{C_{4bp}\} = \\ \begin{Bmatrix} C_{41} & C_{42} & C_{43} + k_A y_A - k_B y_B & C_{44} + k_A y_A^2 - k_B y_B^2 & C_{45} - k_A x_A y_A + k_B x_B y_B & C_{46} \end{Bmatrix} \quad (81)$$

and

$$\{B_{4bp}\} = \\ \begin{Bmatrix} B_{41} & B_{42} & B_{43} + c_A y_A - c_B y_B & B_{44} + c_A y_A^2 - c_B y_B^2 & B_{45} - c_A x_A y_A - c_B x_B y_B & B_{46} \end{Bmatrix} \quad (82)$$

### Pitch Equation:

$$\begin{pmatrix} M_{51b} + A_{51b} & M_{52b} + A_{52b} & M_{53b} + A_{53b} & M_{54b} + A_{54b} & M_{55b} + A_{55b} & M_{56b} + A_{56b} \end{pmatrix} \begin{Bmatrix} \ddot{\eta}_{1b} \\ \ddot{\eta}_{2b} \\ \ddot{\eta}_{3b} \\ \ddot{\eta}_{4b} \\ \ddot{\eta}_{5b} \\ \ddot{\eta}_{6b} \end{Bmatrix} + \\ + \begin{pmatrix} B_{51b} & B_{52b} & B_{53b} & B_{54b} & B_{55b} & B_{56b} \end{pmatrix} \begin{Bmatrix} \dot{\eta}_{1b} \\ \dot{\eta}_{2b} \\ \dot{\eta}_{3b} \\ \dot{\eta}_{4b} \\ \dot{\eta}_{5b} \\ \dot{\eta}_{6b} \end{Bmatrix} + \begin{pmatrix} C_{51b} & C_{52b} & C_{53b} & C_{54b} & C_{55b} & C_{56b} \end{pmatrix} \begin{Bmatrix} \eta_{1b} \\ \eta_{2b} \\ \eta_{3b} \\ \eta_{4b} \\ \eta_{5b} \\ \eta_{6b} \end{Bmatrix} = \\ = (F_{5wb}) + (\xi_A - w_A) k_A x_A + (\xi_B - w_B) k_B x_B + (\dot{\xi}_A - \dot{w}_A) c_A x_A + (\dot{\xi}_B - \dot{w}_B) c_B x_B$$

Easily can be shown that equation the above equation becomes

$$\begin{aligned} & \{M_{sb} + A_{sb}\}\{\ddot{\eta}_b\} + \{B_{sbp}\}\{\dot{\eta}_b\} + \{C_{sbp}\}\{\eta_b\} + w_A k_A x_A + w_B k_B x_B + \dot{w}_A c_A x_A + \dot{w}_B c_B x_B \\ & = (F_{5wb}) \end{aligned} \quad (83)$$

where

$$\begin{aligned} & \{C_{sbp}\} = \\ & \begin{Bmatrix} C_{51} & C_{52} & C_{53} - k_A x_A - k_B x_B & C_{54} - k_A x_A y_A - k_B x_B y_B & C_{55} + k_A x_A^2 + k_B x_B^2 & C_{56} \end{Bmatrix} \end{aligned} \quad (84)$$

and

$$\begin{aligned} & \{B_{sbp}\} = \\ & \begin{Bmatrix} B_{51} & B_{52} & B_{53} - c_A x_A - c_B x_B & B_{54} - c_A x_A y_A - c_B x_B y_B & B_{55} + c_A x_A^2 + c_B x_B^2 & B_{56} \end{Bmatrix} \end{aligned} \quad (85)$$

For the ramp the equation of motion in the time domain becomes

$$\begin{aligned} & [M_p]\{\ddot{d}_p\} + [C_p]\{\dot{d}_p\} + [K_p]\{d_p\} = \{F_p\} + (\xi_A - w_A)k_A + (\xi_B - w_B)k_B + \\ & + (\dot{\xi}_A - \dot{w}_A)c_A + (\dot{\xi}_B - \dot{w}_B)c_B \end{aligned} \quad (86)$$

Substituting  $\xi$  and rearranging, Equation (86) becomes

$$\begin{aligned} & [M_p]\{\ddot{d}_p\} + [C_p]\{\dot{d}_p\} + [K_p]\{d_p\} - \eta_3(k_A + k_B) - \eta_4(k_A y_A + k_B y_B) - \\ & - \eta_5(-x_A k_A - x_B k_B) - \dot{\eta}_3(c_A + c_B) - \dot{\eta}_4(c_A y_A + c_B y_B) - \dot{\eta}_5(-x_A c_A - x_B c_B) + \\ & + w_A k_A + w_B k_B + \dot{w}_A c_A + \dot{w}_B c_B = \{F_p\} \end{aligned} \quad (87)$$

or

$$\begin{aligned} & [M_p]\{\ddot{d}_p\} + [C_{pb}]\{\dot{d}_p\} + [K_{pb}]\{d_p\} - \eta_3(k_A + k_B) - \eta_4(k_A y_A + k_B y_B) - \\ & - \eta_5(-x_A k_A - x_B k_B) - \dot{\eta}_3(c_A + c_B) - \dot{\eta}_4(c_A y_A + c_B y_B) - \dot{\eta}_5(-x_A c_A - x_B c_B) = \{F_p\} \end{aligned} \quad (88)$$

where

$$[C_{pb}] = \begin{bmatrix} C_{11} & \cdots & \cdots & \cdots & \cdots & C_{1\ 363} \\ \vdots & \ddots & \cdots & \cdots & \cdots & \vdots \\ \vdots & \cdots & \ddots & \cdots & \cdots & \vdots \\ \vdots & \cdots & \cdots & C_{333\ 333} + c_B & \cdots & \vdots \\ \vdots & \cdots & \cdots & \cdots & \ddots & \vdots \\ C_{363\ 1} & \cdots & \cdots & \cdots & \cdots & C_{363\ 363} + c_A \end{bmatrix} \quad (89)$$

and

$$[K_{pb}] = \begin{bmatrix} K_{11} & \cdots & \cdots & \cdots & \cdots & K_{1\ 363} \\ \vdots & \ddots & \cdots & \cdots & \cdots & \vdots \\ \vdots & \cdots & \ddots & \cdots & \cdots & \vdots \\ \vdots & \cdots & \cdots & K_{333\ 333} + k_B & \cdots & \vdots \\ \vdots & \cdots & \cdots & \cdots & \ddots & \vdots \\ K_{363\ 1} & \cdots & \cdots & \cdots & \cdots & K_{363\ 363} + k_A \end{bmatrix} \quad (90)$$

## 2. Roll Mitigation Coupling Condition

The second coupling condition considered is a roll mitigation coupling condition. For demonstration purposes, we assume that one point of the barge is connected at the center of the ramp with the use of a special universal joint. This allows heave transfer from the barge to the ramp but leaves the two other degrees of freedom (roll and pitch) free. The universal joint will be modeled as a spring that connects one point at the end of the barge with three points in the middle of the ramp. The three points on the ramp were considered to represent an area in the physical model. The stiffness of the springs was chosen such that the vertical motion of the ramp follows the vertical motion of the barge without producing singularities in the solution.

By constructing a free body diagram for the ramp and the barge the new equations of motion can be found. The coupled equations of motion of the barge for the heave, roll, pitch motions become

$$\{M_{3b} + A_{3b}\}\{\ddot{\eta}_b\} + \{B_{3b}\}\{\dot{\eta}_b\} + \{C_b\}\{\eta_b\} = \{F_{3wb}\} - \sum_{i=1}^3 (\xi_C - w_{C_i}) k_C \quad (91)$$

$$\{M_{4b} + A_{4b}\}\{\ddot{\eta}_b\} + \{B_{4b}\}\{\dot{\eta}_b\} + \{C_{4b}\}\{\eta_b\} = \{F_{4wb}\} + \sum_{i=1}^3 (\xi_C - w_{C_i}) k_C d_{yc} \quad (92)$$

$$\{M_{sb} + A_{sb}\}\{\ddot{\eta}_b\} + \{B_{sb}\}\{\dot{\eta}_b\} + \{C_{sb}\}\{\eta_b\} = \{F_{5wb}\} + \sum_{i=1}^3 (\xi_C - w_{C_i}) k_C d_{xc} \quad (93)$$

where  $k_C$  is the stiffness of the springs, and  $C, C_i$  represent the connection points on the barge and the ramp respectively. By substituting the value of  $\xi$  in Equations (91) - (93) and rearranging we get

$$[M_b + A_b]\{\ddot{\eta}_b\} + [B_b]\{\dot{\eta}_b\} + [C_{bp}]\{\eta_b\} = \begin{Bmatrix} F_{1wb} \\ F_{2wb} \\ F_{3wb} + 3 \sum_{i=1}^3 w_{C_i} k_C \\ F_{4wb} + 3 \sum_{i=1}^3 w_{C_i} k_C d_{yc} \\ F_{5wb} - 3 \sum_{i=1}^3 w_{C_i} k_C d_{xc} \\ F_{6wb} \end{Bmatrix} \quad (94)$$

where

$$[C_{bp}] = \begin{bmatrix} C_{11} & C_{12} & C_{13} & C_{14} & C_{15} & C_{16} \\ C_{21} & C_{24} & C_{23} & C_{24} & C_{25} & C_{26} \\ C_{31} & C_{32} & C_{33} + 3k_C & C_{34} + \sum_{i=1}^3 d_{yC_i} k_C & C_{35} - \sum_{i=1}^3 d_{xC_i} k_C & C_{36} \\ C_{41} & C_{42} & C_{43} + \sum_{i=1}^3 d_{yC_i} k_C & C_{44} + \sum_{i=1}^3 d_{yC_i}^2 k_C & C_{45} + \sum_{i=1}^3 d_{xC_i} d_{yC_i} k_C & C_{46} \\ C_{51} & C_{52} & C_{53} - \sum_{i=1}^3 d_{xC_i} k_C & C_{54} - \sum_{i=1}^3 d_{xC_i} d_{yC_i} k_C & C_{55} + \sum_{i=1}^3 d_{xC_i}^2 k_C & C_{56} \\ C_{61} & C_{62} & C_{63} & C_{64} & C_{65} & C_{66} \end{bmatrix} \quad (95)$$

For the ramp the equation of motion in the time domain becomes

$$[M_p]\{\ddot{d}_p\} + [C_p]\{\dot{d}_p\} + [K_p]\{d_p\} = \{F_p\} + \sum_{i=1}^3 (\xi_C - w_{C_i}) k_C \quad (96)$$

By substituting  $\xi$  and rearranging, Equation (96) becomes

$$[M_p]\{\ddot{d}_p\} + [C_p]\{\dot{d}_p\} + [K_p]\{d_p\} - 3\eta_3 k_C - 3\eta_4 y_C k_C + 3\eta_5 x_C k_C + \sum_{i=1}^3 w_{C_i} k_C = \{F_p\} \quad (97)$$

or

$$[M_p]\{\ddot{d}_p\} + [C_b]\{\dot{d}_p\} + [K_{pb}]\{d_p\} - 3\eta_3 k_C - 3\eta_4 y_C k_C + 3\eta_5 x_C k_C = \{F_p\} \quad (98)$$

where

$$[K_{pb}] = \begin{bmatrix} K_{11} & \cdots & \cdots & \cdots & \cdots & K_{1 \ 363} \\ \vdots & \ddots & \cdots & \cdots & \cdots & \vdots \\ \vdots & \cdots & \ddots & \cdots & \cdots & \vdots \\ \vdots & \cdots & \cdots & K_{i \ i} + k_C & \cdots & \vdots \\ \vdots & \cdots & \cdots & \cdots & \ddots & \vdots \\ K_{363 \ 1} & \cdots & \cdots & \cdots & \cdots & K_{363 \ 363} \end{bmatrix} \quad (99)$$

and  $i = 180, 183, 186$ .

### C. COUPLED SOLUTION IN FREQUENCY DOMAIN

The solution of the ship-ramp-barge system in the frequency domain is required in order to obtain the new RAO of the barge motions and the RAO of the ramp motion. In order to obtain the solution of the complete system, the motion of the ship has to be taken into account. It is assumed that the end of the ramp attached to the ship is pinned on the ship's stern. Therefore, all the points along the ship-end of the ramp are going to follow the ship's vertical motion. This induces the following boundary condition for all points across the ship-end of the ramp

$$w_i = \xi_{s_i} \quad (100)$$

and

$$(\theta_x)_i = -\eta_{4s} \quad (101)$$

where  $w_i$  is the displacement along the z axis of a point  $i$  on the ramp,  $(\theta_x)_i$  is the rotation along the x axis of a point  $i$  on the ramp,  $\xi_{s_i}$  is the displacement along the z axis of a point  $i$  on the ship, and  $\eta_{4s}$  is the roll angle of the ship.

Quantities  $\xi_i, \eta_4$  are known from the hydrodynamics of the ship. Therefore, Equations (100) and (101) can be implemented as boundary conditions in the finite element model of the ramp. This means that the stiffness and the force matrices of the ramp, as shown in Equations (90) and (99) have already taken into account the ship's motions.

It should be pointed out that the equations of motion of the barge as shown in (73) do not reflect the proximity effect of the ship's presence. To take into account the ship's presence, additional forces have to be added. In the solution presented in section II those forces were taken into account since the full  $12 \times 12$  system was solved, while Equations (73) are only a  $6 \times 6$  system. Forces due to proximity effects are added in Equations (76) and (94) as additional external excitation vectors  $\{F_{bs}\}$  that are proportional to the ship's accelerations and velocities.

Furthermore, in the scenario considered in this work, the load of two tanks was placed in the middle of the ramp. This was done in order to model the envisioned worst-case scenario of one vehicle stopped because of mechanical failure and another coming to provide assistance. This adds an additional force vector  $F_L$  in Equations (88) and (98). Therefore, the equations of the ramp and the barge can be coupled together in a single system of equations

$$[M_{aug}]\{\ddot{d}_{aug}\} + [C_{aug}]\{\dot{d}_{aug}\} + [K_{aug}]\{d_{aug}\} = \{F_{aug}\} \quad (102)$$

where

$$\{d_{aug}\} = \begin{Bmatrix} \{d_p\} \\ \{\eta_b\} \end{Bmatrix} \quad (103)$$

$$[M_{aug}] = \begin{bmatrix} [M_p] & [0] \\ [0] & [M_b + A_b] \end{bmatrix} \quad (104)$$

$$[C_{aug}] = \begin{bmatrix} [C_{pb}] & [C_1] \\ [C_2] & [B_{bp}] \end{bmatrix} \quad (105)$$



$$\begin{bmatrix} K_{aug} \end{bmatrix} = \begin{bmatrix} \begin{bmatrix} K_{pb} \end{bmatrix} & \begin{bmatrix} K_1 \end{bmatrix} \\ \begin{bmatrix} K_2 \end{bmatrix} & \begin{bmatrix} C_{bp} \end{bmatrix} \end{bmatrix} \quad (106)$$

$$\{F_{aug}\} = \begin{Bmatrix} \{F_p + F_L\} \\ \{F_{wb} + F_{bs}\} \end{Bmatrix} \quad (107)$$

and  $C_1, C_2, K_1, K_2$  are the coupling matrices, created by the additional left hand term quantities in the Equations (76), (88), (94) and (98).

By using the same linear theory assumption as in section II the vector of displacements can be written as

$$\{\ddot{d}_{aug}\} = -\omega_e^2 \{\bar{d}_{aug}\} e^{i\omega_e t} \quad (108)$$

$$\{\dot{d}_{aug}\} = i\omega_e \{\bar{d}_{aug}\} e^{i\omega_e t} \quad (109)$$

where again  $\omega_e$  is the frequency of the incoming wave and  $\bar{d}_{aug}$  are the complex amplitudes of the displacements.

The solution of Equation (102) in the frequency domain then becomes

$$\{\bar{d}_{aug}\} = \frac{\{\bar{F}_{aug}\}}{\begin{bmatrix} -\omega_0^2 M_{aug} + i\omega_0 C_{aug} + K_{aug} \end{bmatrix}} \quad (110)$$

where  $\bar{F}_{aug}$  are the complex amplitudes of the forces.

The above solution represents the Response Amplitude Operator (RAO) of the ramp and the barge in the coupled system.

#### D. STRESS CALCULATION FOR THE RAMP

The solution of Equation (110) can be used to obtain the stress for the ramp. From Hooke's Law it is known that

$$\sigma = E\varepsilon \quad (111)$$

$$\tau = G\gamma \quad (112)$$

Substituting Equations (40), (41) in (111), (112) and rearranging

$$\begin{Bmatrix} \sigma_x \\ \sigma_y \\ \tau_{xy} \end{Bmatrix} = \begin{bmatrix} E & 0 & 0 \\ 0 & E & 0 \\ 0 & 0 & G \end{bmatrix} \begin{Bmatrix} \varepsilon_x \\ \varepsilon_y \\ \gamma_{xy} \end{Bmatrix} \quad (113)$$

The same process with Equations (42), (43) yields

$$\begin{Bmatrix} \tau_{xz} \\ \tau_{yz} \end{Bmatrix} = G \begin{Bmatrix} \gamma_{xz} \\ \gamma_{yz} \end{Bmatrix} \quad (114)$$

The strains can be found by substituting the solution of Equation (110) in Equations (61) and (62). Therefore, the Von-Misses stress for the elements of the ramp can be found from

$$\sigma_{VM} = \frac{1}{\sqrt{2}} \sqrt{(\sigma_x - \sigma_y)^2 + (\sigma_y - \sigma_z)^2 + (\sigma_z - \sigma_x)^2 + 6(\tau_{xy}^2 + \tau_{yz}^2 + \tau_{xz}^2)} \quad (115)$$

where in our case  $\sigma_z = 0$ . Unlike the ramp validation case, the true value of Young's modulus of elasticity is used to calculate stresses.

## E. RESULTS

Numerical results are presented in Appendix B. The general parameters used in the numerical solution are presented in Table 2. The spring-damper boundary conditions were used throughout the results, see Figure 7 of Appendix B for a schematic. The nominal values for the spring and damper constants are also shown in Appendix B. Unless otherwise stated, these values will be used for the results.

The effect of the flexural rigidity of the ramp and the assumed boundary conditions on RRDF response is shown in Figure2 B1 through B24. It can be seen that, in general, the effects of the ramp does not alter the fundamental frequency response shape of the RRDF. This can be attributed to the high hydrostatic stiffness of the large waterplane area, shallow bodies, that make up the RRDF. Although the general shape of the response amplitude operator does not change, the relative values differ so that the response in a seaway will be different. This means that the effect of the ramp and the spring/damper constants on the RRDF is expected to be measurable and it could be quantified in random seas. This will be explored further in the next chapter.

A comprehensive set of plots showing the response of the RRDF as modified by the ramp, for all heading angles is presented in Figures B25 through B30. As expected, wave direction has a very significant effect on RRDF response. Therefore, results in random seas are expected to vary greatly depending on sea directionality.

Figures B31 through B38 present results on the relative motions between at the two touchdown points between the ramp and the RRDF. Point A is the starboard connection point, and point B is the port connection point, see Figure 7. Figures B39 and B40 summarize the relative motion results for all wave headings. The relative motion results are used in figures B41 and B42 to calculate and present the ramp twist angle RAO as a function of frequency and wave direction. The ramp twist angle is of extreme importance in operations, since it is directly related to maximum stress, which is in most cases the limiting factor in performance. Figures B43 through B46 show 3-dimensional views of the ramp displacement field. These are presented selected frequencies and wave directions and are to be used for general visualization purposes; the vertical scale is much smaller than the horizontal scale and do not necessarily reflect the actual ramp deformation in a forced motion setting.

Finally, the remaining figures in Appendix B show representative RAO's in terms of ramp stress. The maximum stress in the ramp in terms of frequency and wave direction is shown in Figures B47 and B48. Peaks in the stress correspond to either maximum relative motion or ramp twist. When coupled with an appropriate seaway model, these will result in maximum expected values in a given seaway. Representative stress fields in the ramp for select wave periods and headings are shown in Figures B49 through B52.

## **V. RESPONSE IN A SEAWAY**

### **A. INTRODUCTION**

The ultimate goal of ship motion studies is to be able to predict how the ship will behave in realistic irregular seas. As already mentioned in section II the calculation of a vessel's motions in regular waves is only the first step towards the prediction of the motions in a seaway. According to the method proposed in 1953 by St. Denis and Pierson, using spectral methods developed in other fields, it is possible to relate the spectral density of ship responses to the input ocean wave spectrum. In Ref. [2] and [8] the interested reader can find a very detailed discussion on seaway modeling. Here only a short description and some useful formulas will be presented.

### **B. DESCRIPTION OF THE SEAWAY**

The wave patterns in an open sea are ever changing with time and space, in a manner that appears to defy analysis be it linear or second order Stokes waves. Ambient waves on the surface of the sea are dispersive as well as random. Random refers to the character of the wave height distribution. The generating mechanism is, predominantly, the effect upon the water surface of wind in the atmosphere. The wind is itself random, especially when viewed from the standpoint of the turbulent fluctuations and eddies which are important in generating waves. The randomness of sea waves is subsequently enhanced by their propagation over large distances in space and time and their exposure to the random nonuniformities of the water and air.

According to the principle of superposition, one could attempt a description of the seaway deterministically accounting for each one of the individual wave components. Leaving aside the issue of whether such an approach is possible or not, it is clearly a highly impractical task. Fortunately, it is not required either. It would suffice to represent sea waves in a probabilistic manner.

The statistical properties of a random process can be defined with two possible ways. It can be considered with statistical properties taken "across the ensemble" at fixed values of time  $t = t_1, t = t_2$ , etc., or may be considered with properties of the random process taken "along the ensemble" where  $t_1, t_2$ , etc., are assumed to vary. Description of

a random process so general would require an enormous amount of information. Fortunately, for certain random processes such as sea waves, it is possible to assume that the process is of a special form: "stationary", "homogeneous", and "ergodic". For sea waves it should be adequate to describe the wave environment over a period of a few hours (or before the next weather report comes in), and to assume that the wave motion is stationary (its statistics remain the same over time) during this interval of time. Likewise, there is no interest in describing the wave environment simultaneously throughout the world, a small area of operations is all that is needed, and it can be assumed that the wave motion is homogeneous (its statistics remain the same in that area) in space over the area in question. These statements have meaning only in a statistical sense, since for a random wave system it would be funny to suggest that the precise wave motion is the same at different points in space or time. Eventually, it is reasonable to assume that the statistical properties of the waves measured over time, should be "typical" of the random process. This means that they should be the same even if we were able to sample all possible realizations of the wave motion at a fixed time. Such random processes are said to be ergodic.

One of the most significant parameters needed in order to arrive at a statistical description of the seaway is the total mean energy of the wave system per unit area of the free surface ( $\bar{E}$ ). It can be shown from hydrodynamics that this is equal to:

$$\bar{E} = \rho g \int_0^\infty \int_0^{2\pi} S(\omega, \theta) d\theta d\omega \quad (116)$$

where  $\theta$  is the wave direction. The function  $S(\omega, \theta)$  is called the spectral density and more rigorously can be defined as the Fourier transform of the correlation function for the free surface elevation. It is customary to ignore the factor  $\rho g$  and to refer to the function  $S(\omega, \theta)$  as the spectral energy density or simply the energy spectrum. More specifically, this is a directional energy spectrum. It can be integrated over all wave directions to give the frequency spectrum:

$$S(\omega) = \int_0^{2\pi} S(\omega, \theta) d\theta \quad (117)$$

Using Equations (116) and (117) we can see that:

$$\bar{E} = \int_0^\infty S(\omega) d\omega \quad (118)$$

i.e., the area under the spectrum  $S(\omega)$  is equal to (within the constant  $\rho g$ ) the mean energy stored in that particular wave system. If one attempts to find the sea wave spectrum from measurements of the free surface elevation at a single point in space, for instance by recording the heave motion of a buoy, the directional characteristic of the waves will be lost. Only the frequency spectrum (117) can be determined from such a restricted set of data. A limited amount of directional information follows if one measures the slope of the free surface, for example by measuring the angular response of the buoy as well as its heave. A complete description of the directional wave spectrum requires an extensive array of measurements at several adjacent points in space, and there are practical difficulties associated with this task.

As a simpler alternative, one can assume that the waves are unidirectional, with the energy spectrum proportional to a delta function in  $\theta$ . Wave spectra of this form are called long crested, since the fluid motion is two-dimensional and the wave crests are parallel, and the frequency spectrum (117) is sufficient to describe the wave environment.

If the waves are generated by a single storm, far removed from the point of observation, it might be presumed that these waves would come from the direction of the storm in a long crested manner. The limitations of this assumption are obvious to anyone who has observed the sea surface. While a preferred direction may exist, especially for long swell that has traveled large distances, even these long waves will be distributed in their direction, and for short steep waves the directional variation is particularly significant. Since the superposition of such waves from a range of different directions appears in space as a variation of the free surface elevation in all directions, these waves are known as short crested waves.

Usually in the fields of ocean engineering and naval architecture it is customary to assume that the waves are long crested. With such a simplification it is possible to use existing information for the frequency spectrum (117), which is based on a combination of theory and full-scale observations. Sea wave spectra depend on the velocity of the wind as well as its duration in time and the distance over which the wind is acting on the

free surface. This distance is known as the fetch. Wave spectra that have reached a steady state of equilibrium, independent of the duration and fetch are known as fully developed. There are many proposals of the analytical expression of the frequency spectrum. Some of them are generic and some of them are based on observations and data collected in specific geographical regions. A semi-empirical generic expression for the frequency spectrum of fully developed seas is:

$$S(\omega) = \frac{\alpha g^2}{\omega^5} \exp \left[ -\beta \left( \frac{g}{U\omega} \right)^4 \right] \quad (119)$$

Here  $\alpha$  and  $\beta$  are nondimensional parameters defining the spectrum, and  $U$  is the wind velocity at a standard height of 19.5 meters above the free surface. This two parameters spectrum is sufficiently general to fit quite a few observations and is consistent with theoretical predictions of the high frequency limit. The most common values for these parameters are:

$$\alpha = 8.1 \times 10^{-3} \quad \text{and} \quad \beta = 0.74 \quad (120)$$

and with these values it is known as the Pierson - Moscovitz spectrum.

### C. SHIP/RAMP/BARGE RESPONSE SPECTRAL ANALYSIS

The relationship between motions in regular and irregular waves must be established in order to use either theoretical equations or experimental studies to lead to practical predictions of system behavior in a realistic seaway. The required relationship is expressed by the principle of linear superposition, which says that the response of a ship to an irregular sea can be represented by a linear summation of its responses to the component regular waves that comprise the irregular sea. To make use of this principle, a ship response to regular waves, whether it has been determined by calculation or by model measurement, is expressed in a Response Amplitude Operator (RAO) form as measure of the response to a regular wave of unit amplitude.

Like the sea waves themselves, a ship response is a random variable. The statistics of a floating body response are identical to the wave statistics, except that the wave energy spectrum  $S$  is multiplied by the square of the RAO (this is a property of linear systems). Thus, if the subscript  $R$  represents any body response, we have:

$$S_R(\omega) = |Z_R(\omega)|^2 S(\omega) \quad (121)$$

where  $Z_R(\omega)$  is the RAO of the response  $R$ , and  $S(\omega)$  the spectrum of the seaway. Equation (121) can then be utilized to obtain the spectrum of the response  $R$ , and after that specific formulas can be used to provide the statistics of this response in a particular sea state.

To a large extent, Equation (121) provides the justification for studying regular wave responses. The transfer function  $Z_R(\omega)$  is valid not only in regular waves, where it has been derived, but also in a superposition of regular waves, and ultimately in a spectrum of random waves. Generally speaking, a vessel with favorable response characteristics in regular waves will be good in irregular waves, and vice versa. This statement is oversimplified, however, and the relative shape of the energy spectrum and the transfer function is very crucial. For example, a large resonant response of the body will be of importance only if the resonant frequency is located close to the peak of the wave energy spectrum, and vice versa.

Eventually, the statistical predictions of the amplitudes of ship motions may be determined from the variance, or spectral area, of a ship response spectrum given by the equation:

$$\bar{S}_R = \int_0^\infty S_R(\omega) d\omega \quad (122)$$

In order to present the random wave results in a more compact manner, the significant and the Root Mean Square (RMS) values of the responses will be employed. The significant value of a random process is defined as the average of the 1/3 of the highest values of all responses and is frequently used in design to characterize the severity of a particular response. The RMS value can be easily computed from the spectrum of the response and is in the square root of the area under the spectrum of the response, which is the integral of the spectrum function over the frequency range. The significant value (single amplitude) is equal to two times the RMS value. To get the “8 hour maximum amplitude”, the RMS value must be multiplied by four. This is also equal to the significant double amplitude or “height” (peak to trough deviation) of the response.



## D. RESULTS

Typical results in random seas are presented in Appendix C. For demonstration purposes, we use the standard Pierson-Moskowitz spectrum at sea state 3, shown in Figure C1. This corresponds to fully developed, long crested unidirectional seas of approximately 4 ft significant wave height, significant range of periods between 2 and 7 seconds, an average period of 4 seconds, a wind speed of 15 knots, and waves of approximately 50 ft wave length. We also use three different settings of the spring and damper coefficients, as follows:

- $(k=1, c=1)$  corresponds to a *soft* spring/damper combination with both values equal to the *nominal* values shown in Table 2 of Appendix B.
- $(k=2, c=2)$  corresponds to a *hard* spring/damper combination with both values equal to 10 times the *nominal* values for  $k$  and  $c$ .
- $(k=3, c=3)$  corresponds to a *very hard* spring/damper combination with both values 100 times larger than the nominal values shown in Table 2 of Appendix B.

Sample plots of response spectra are shown in Figures C2 through C13, in terms of the spectrum of the relative motion at connection point A. The various peaks in the spectrum correspond to combinations of peaks of the corresponding frequency response of the relative motion and the peak of the wave spectrum.

The RMS value of the relative motion at connection point A is calculated based on the above spectra and is shown in Figure C14. Based on these results we can observe the following:

1. The RMS values are higher at port beam and starboard beam seas. For directional sea spectra, the curves viewed as functions of heading would be smoother.
2. Port/starboard response is not symmetric as has been discussed previously.
3. Higher spring and/or damping coefficients result in less relative motions, as expected. This is more pronounced in the case of beam seas and less in the case of following or head seas.

Figures C15 through C20 present the results of Figure C14 in a set of polar plot contours. The radial coordinate in the polar plots is the RMS value of the relative motion, while the angular coordinate designates the wave heading. As can be seen, both spring and damper constants have a direct effect on the contour plots, with the greatest effect due to the spring constant. Figures C21 through C27 present similar results in terms of the ramp twist while Figures C28 through C34 present results in terms of the ramp maximum stress. Here, higher values of the spring constant result, in general, in higher levels of twist and stress. The above sets of graphs can be used to select a compromising set of values of spring constant and damping ratio, which will minimize both relative motions and stresses in a given seaway.

The last sets of graphs, Figures C35 and C36, present for completeness the RMS values of the barge motion at points A and B as functions of heading, and parameterized in terms of the spring and damper constants.

THIS PAGE INTENTIONALLY LEFT BLANK

## **VI. CONCLUSIONS AND RECOMMENDATIONS**

### **A. CONCLUSIONS**

Based on the methodology and the results presented in this thesis, the following conclusions can be made:

1. The dynamics of the two ships show significant hydrodynamic coupling between vertical and horizontal plane motions. More specifically, vertical/horizontal plane coupling for the ship is small for head and following seas, but it can be significant for beam seas.
2. Hydrodynamic coupling between horizontal and vertical plane motions for the RRDF is very significant throughout the wave direction and frequency range and cannot be neglected.
3. Structural coupling of the ramp does not alter the fundamental frequency response shape of the RRDF. However, although the general shape of the response amplitude operator does not change, the relative values differ so that the response in a seaway is different.
4. Relative motions at the ramp/RRDF connection points, as quantified by their RMS values in random seas, are higher for port beam and starboard beam seas.
5. Higher spring and/or damper coefficients result in smaller relative motions but higher levels of twist and stresses. These results are not always strictly monotonic, which suggests that optimization based on a systematic series of parametric studies is possible.
6. Isolator spring constant has, in general, a more pronounced effect on the RMS values of the response than the isolator damping coefficient.

## **B. RECOMMENDATIONS**

The primary recommendations for further research are as follows:

1. A systematic parametric study of various isolator properties (spring and damper constants) and ramp loading conditions in short crested seas [Ref. 8].
2. Incorporation of more accurate, computationally intensive, commercial finite element packages for the ramp, based on the structural synthesis method presented in [Ref. 9].

## **APPENDIX A**

This Appendix contains the following figures:

- Figures A1 through A12: Heave, Roll, and Pitch Amplitudes for the Ship and the RRDF for Various Wave Directions.
- Figures A13 through A28: Comparisons Between Full and Reduced Hydrodynamic Models for the Ship and the RRDF.
- Figures A29 through A44: Vertical Motions at the Ramp/RRDF Connection Points.

Discussion of these figures is presented in Chapter II, Section D.

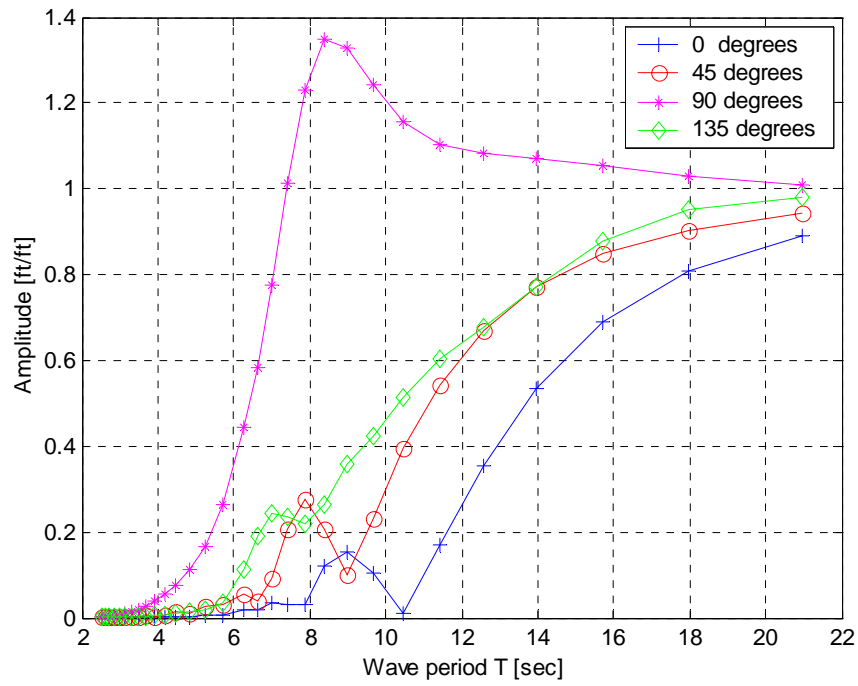


Figure A1. Plot of Heave Amplitude per [ft] Wave Height, for the Ship (CAPE-D) at Various Wave Directions

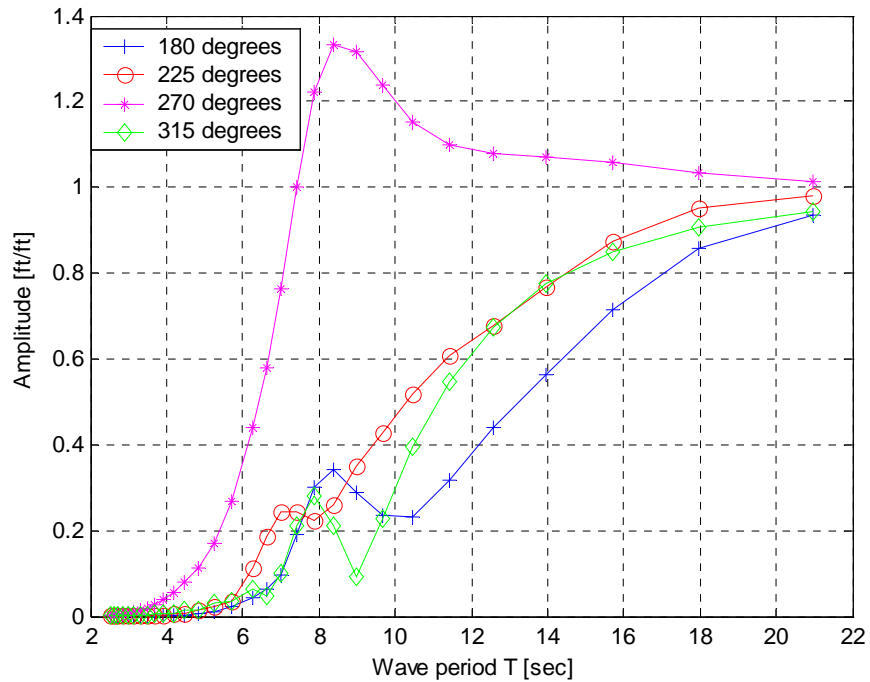


Figure A2. Plot of Heave Amplitude per [ft] Wave Height, for the Ship (CAPE-D) at Various Wave Directions

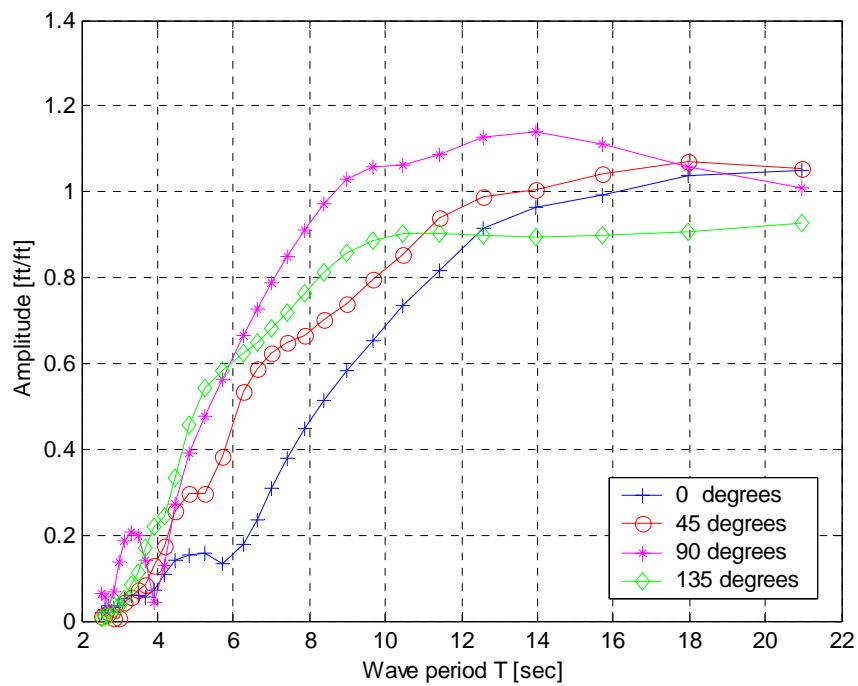


Figure A3. Plot of Heave Amplitude per [ft] Wave Height, for the Barge (RRDF) at Various Wave Directions

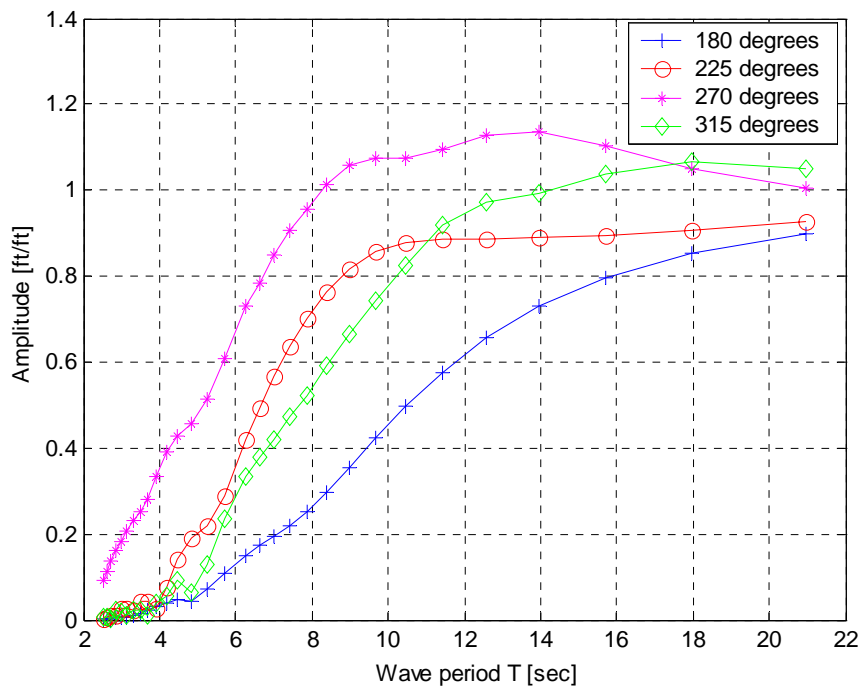


Figure A4. Plot of Heave Amplitude per [ft] Wave Height, for the Barge (RRDF) at Various Wave Directions



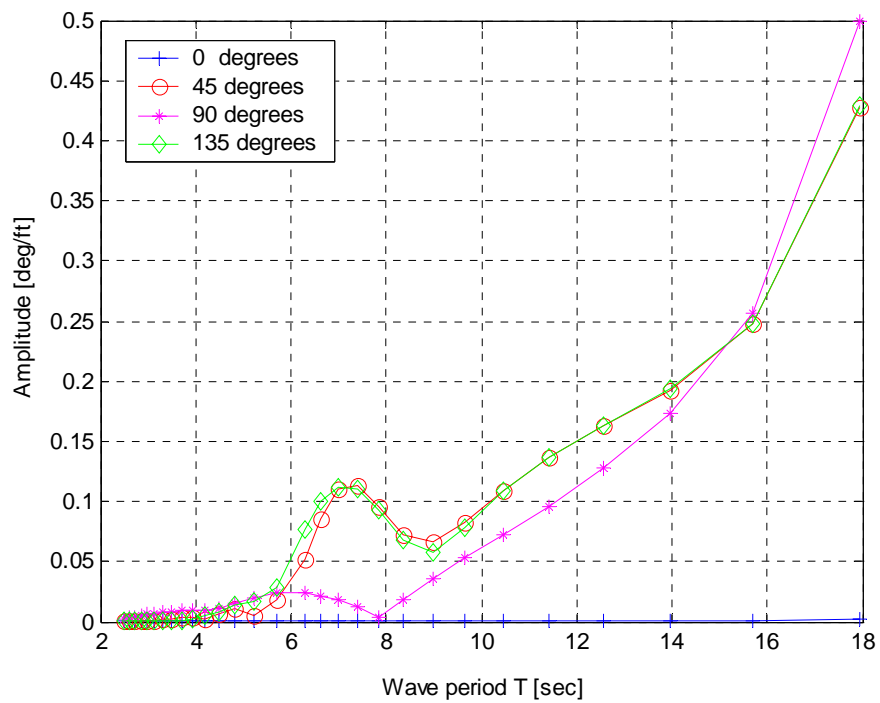


Figure A5. Plot of Roll Amplitude per [ft] Wave Height, for the Ship (CAPE-D) at Various Wave Directions

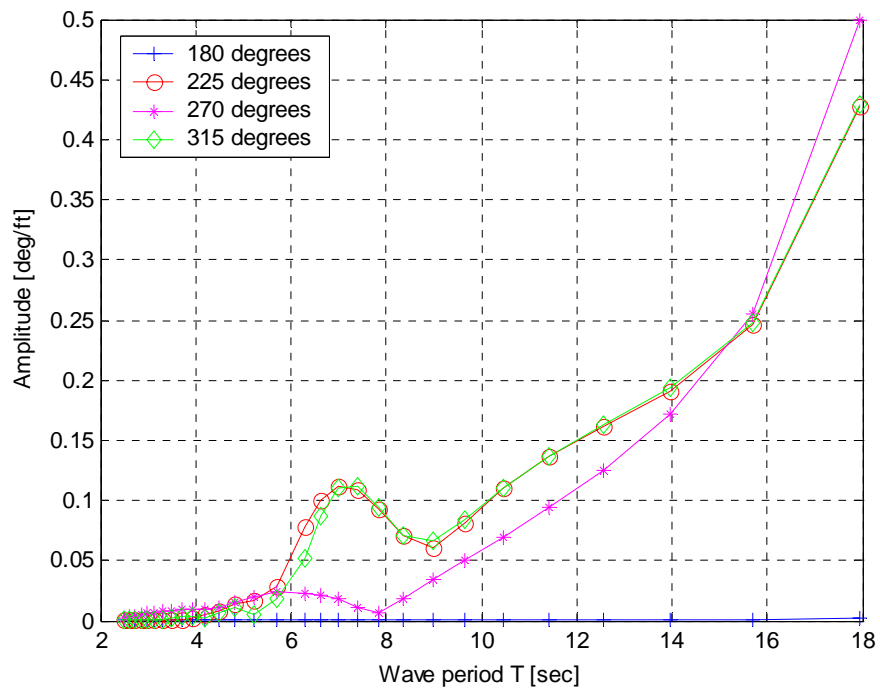


Figure A6. Plot of Roll Amplitude per [ft] Wave Height, for the Ship (CAPE-D) at Various Wave Directions

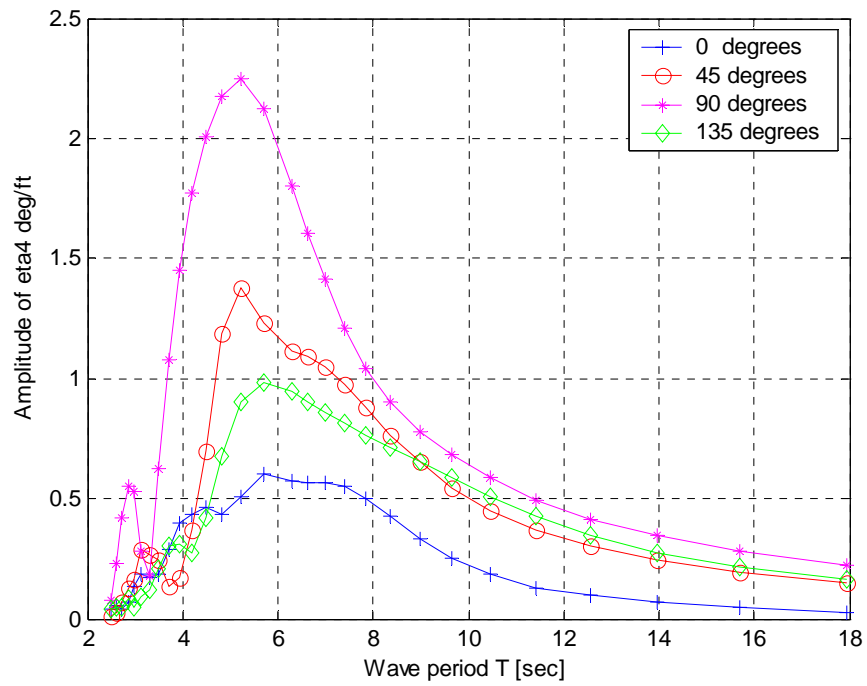


Figure A7. Plot of Roll Amplitude per [ft] Wave Height, for the Barge (RRDF) at Various Wave Directions

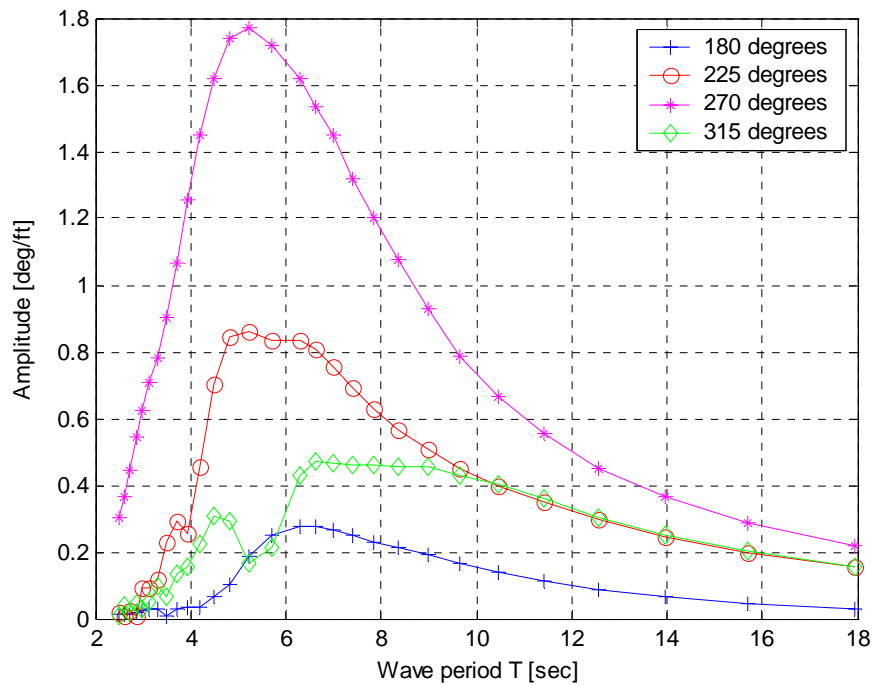


Figure A8. Plot of Roll Amplitude per [ft] Wave Height, for the Barge (RRDF) at Various Wave Directions

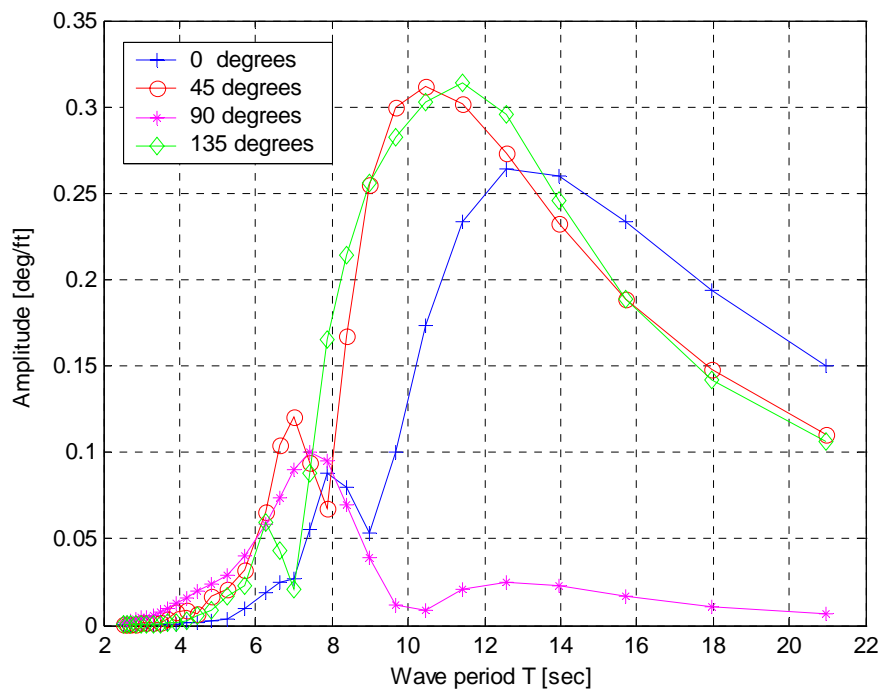


Figure A9. Plot of Pitch Amplitude per [ft] Wave Height, for the Ship (CAPE-D) at Various Wave Directions

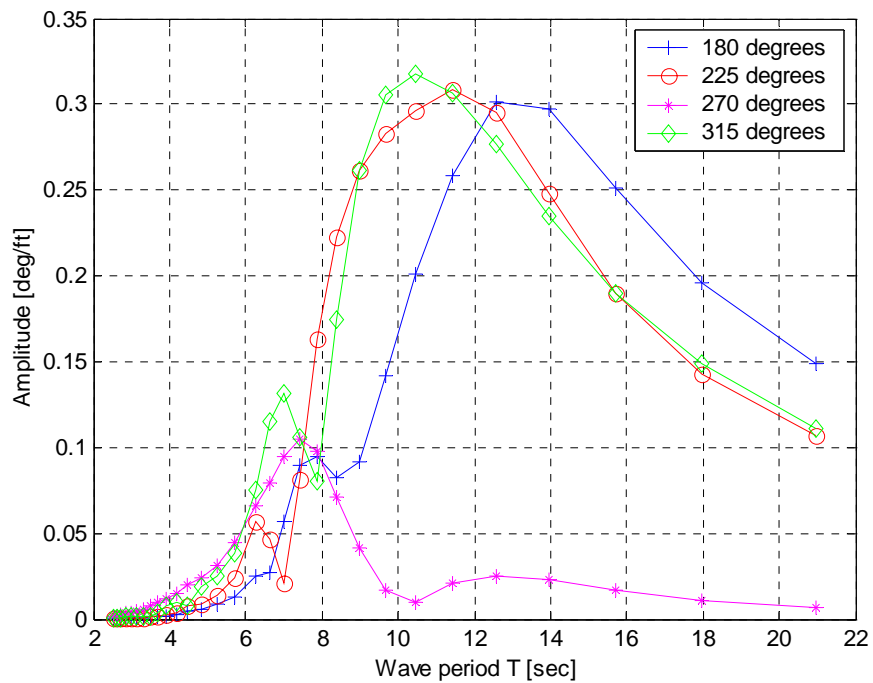


Figure A10. Plot of Pitch Amplitude per [ft] Wave Height, for the Ship (CAPE-D) at Various Wave Directions

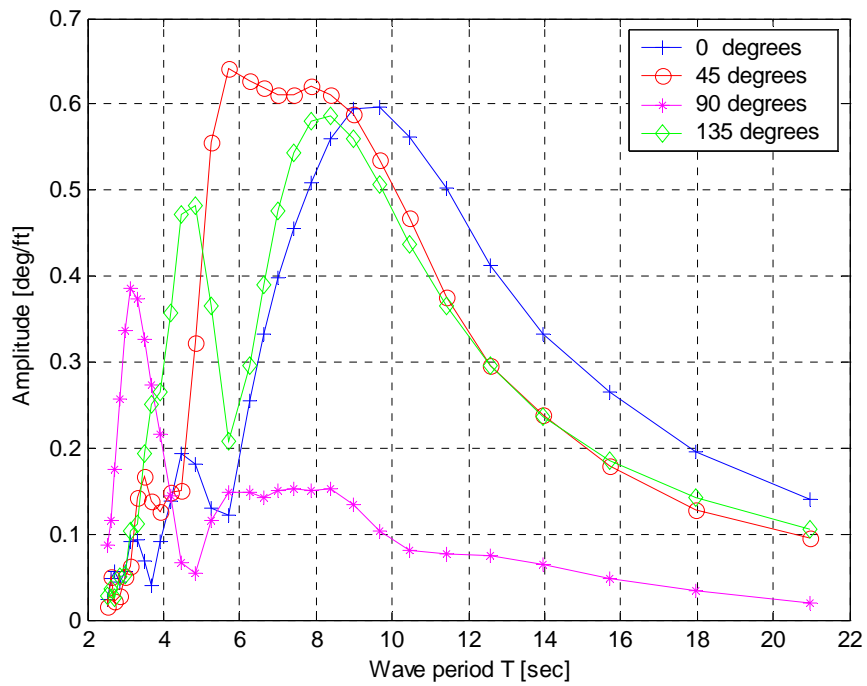


Figure A11. Plot of Pitch Amplitude per [ft] Wave Height, for the Barge (RRDF) at Various Wave Directions

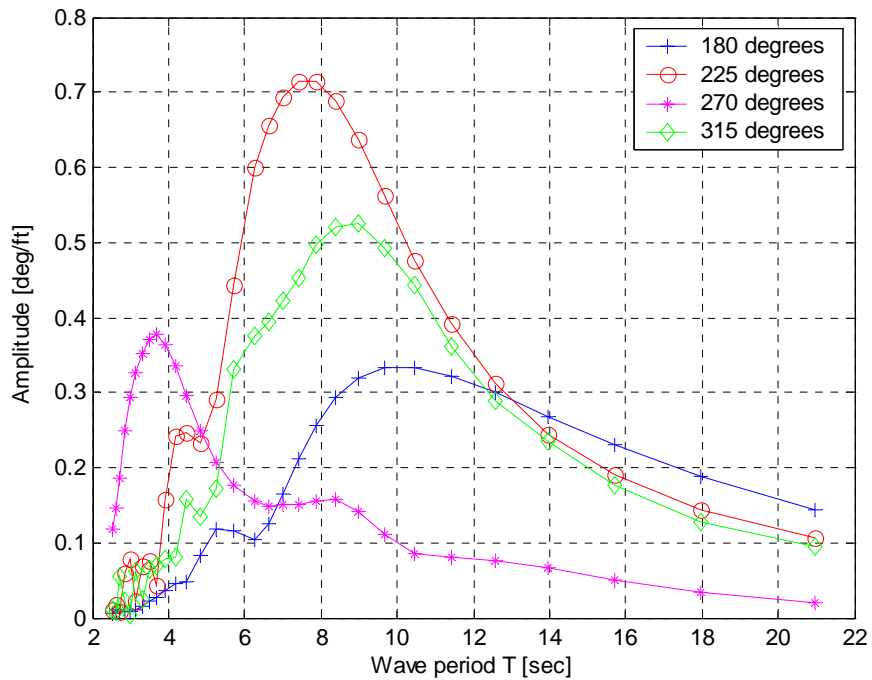


Figure A12. Plot of Pitch Amplitude per [ft] Wave Height, for the Barge (RRDF) at Various Wave Directions

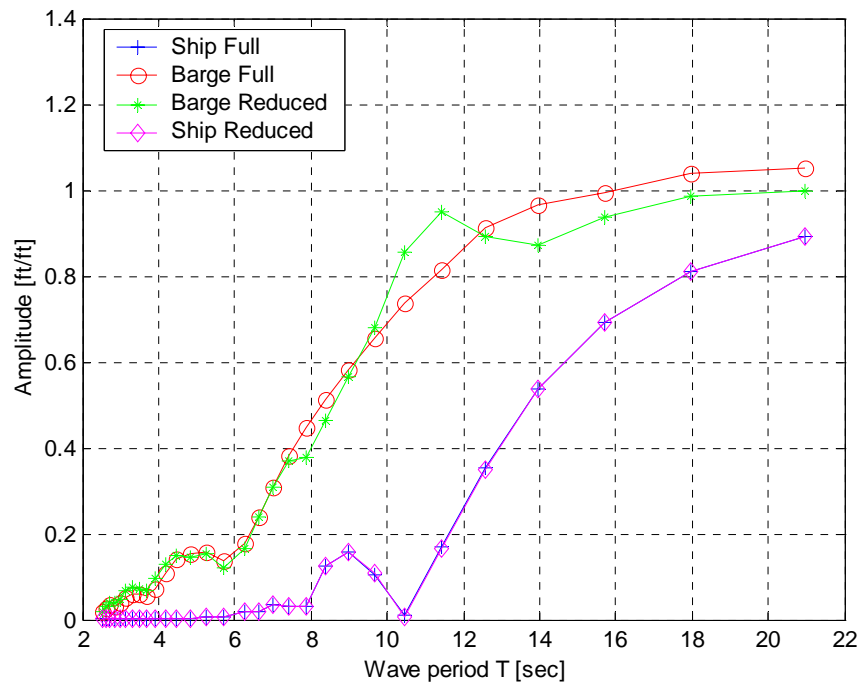


Figure A13. Comparison between Full 12x12 Solution and Reduced Approximation for the Heave Amplitude per [ft] Wave Height at Following Seas (0 deg).

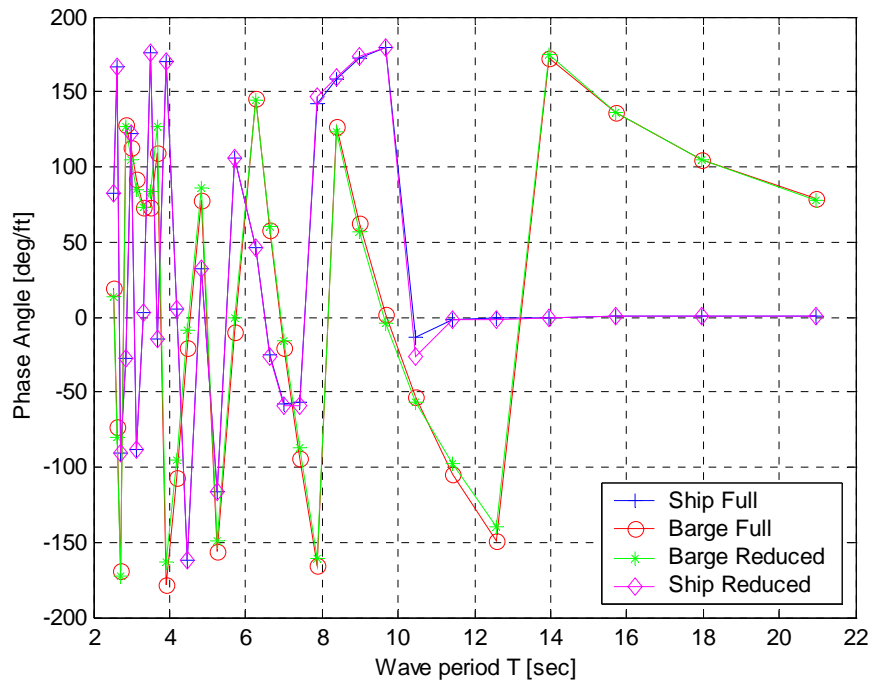


Figure A14. Comparison between Full 12x12 Solution and Reduced Approximation for the Heave Phase Angle per [ft] Wave Height at Following Seas (0 deg).

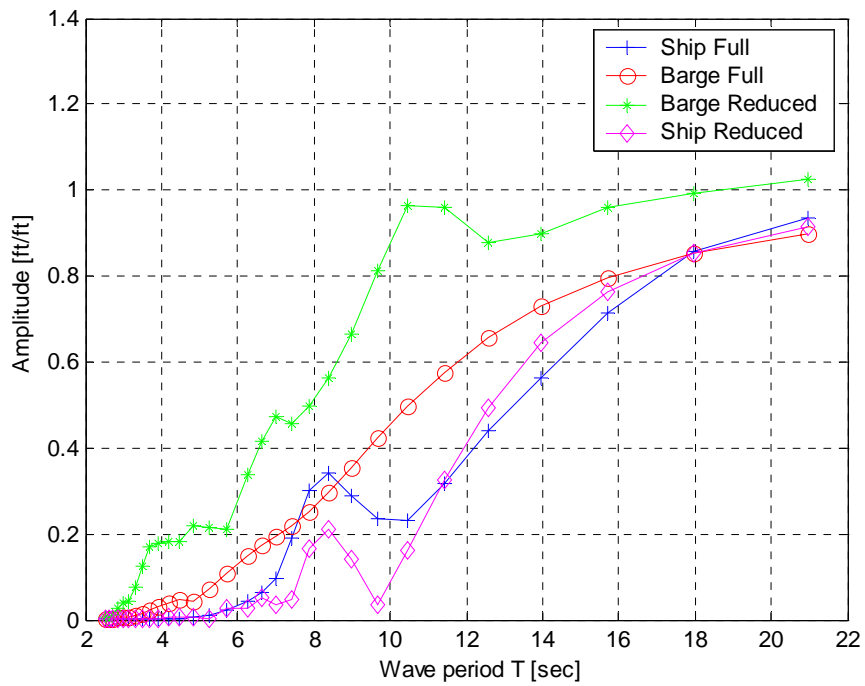


Figure A15. Comparison between Full 12x12 Solution and Reduced Approximation for the Heave Amplitude per [ft] Wave Height at Heading Seas (180 deg).

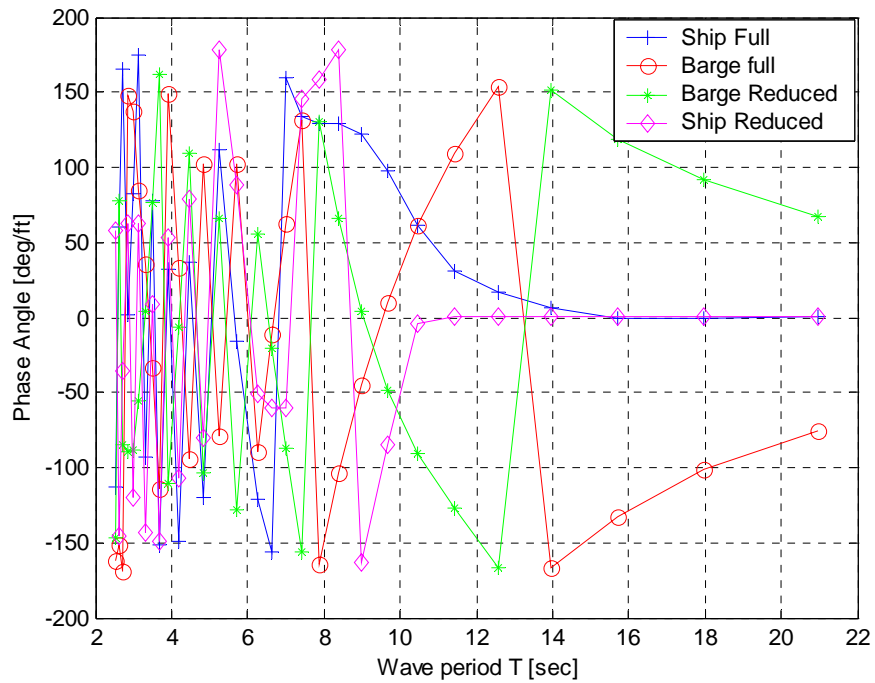


Figure A16. Comparison between Full 12x12 Solution and Reduced Approximation for the Heave Phase Angle per [ft] Wave Height at Heading Seas (180 deg).

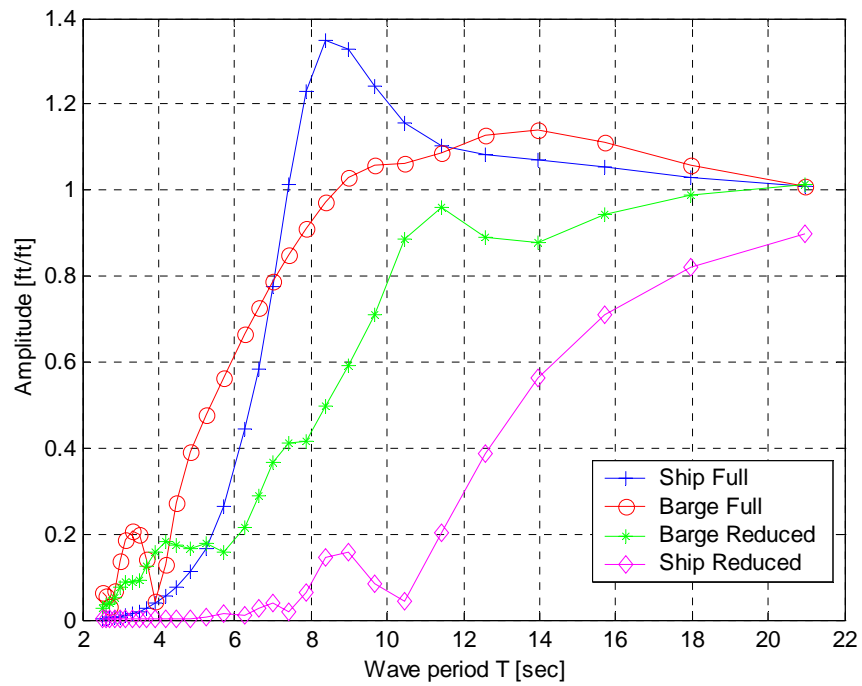


Figure A17. Comparison between Full 12x12 Solution and Reduced Approximation for the Heave Amplitude per [ft] Wave Height at Starboard Beam Seas (90 deg).

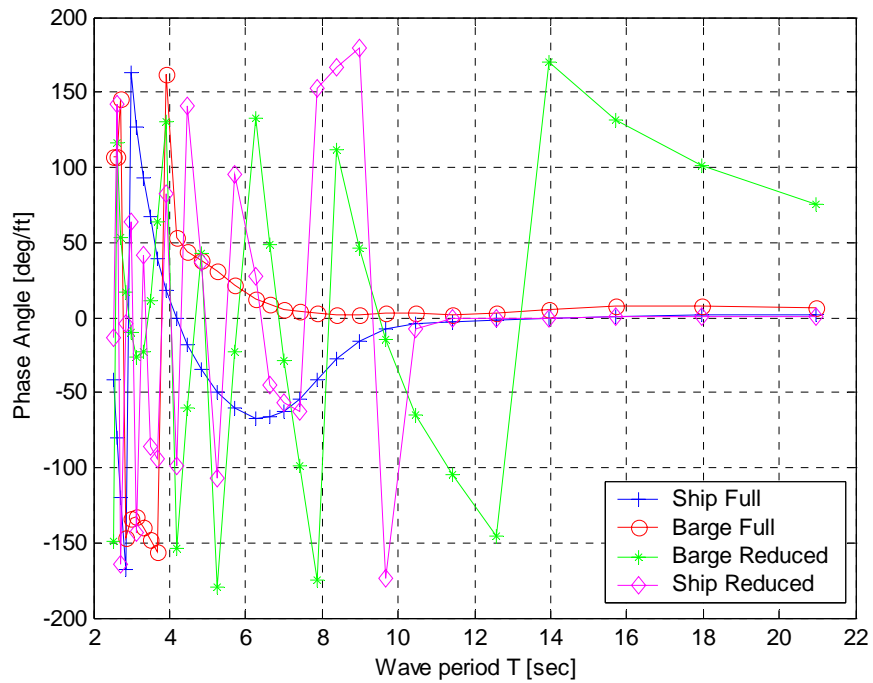


Figure A18. Comparison between Full 12x12 Solution and Reduced Approximation for the Heave Phase Angle per [ft] Wave Height at Starboard Beam Seas (90 deg).

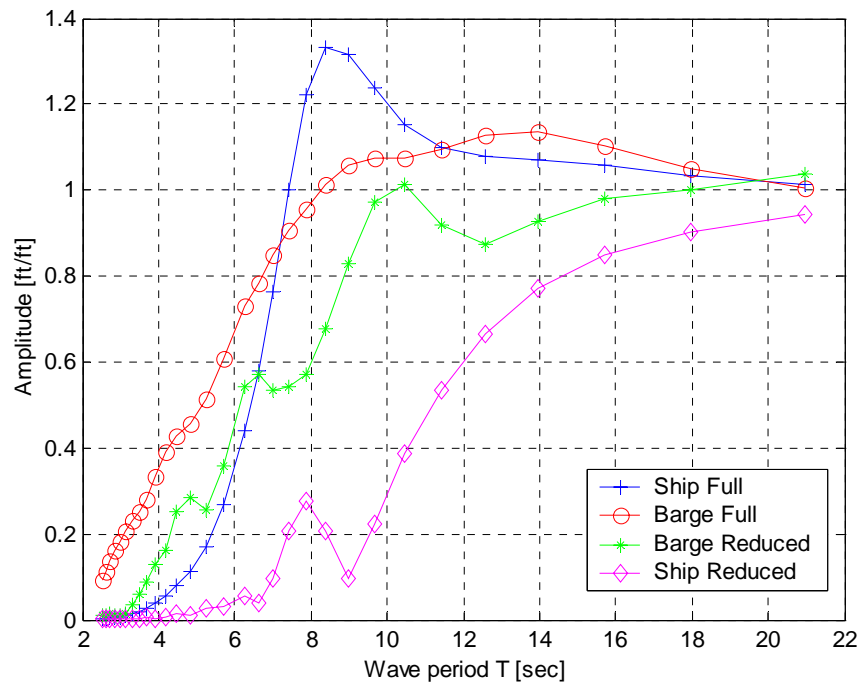


Figure A19. Comparison between Full 12x12 Solution and Reduced Approximation for the Heave Amplitude per [ft] Wave Height at Port Beam Seas (270 deg).

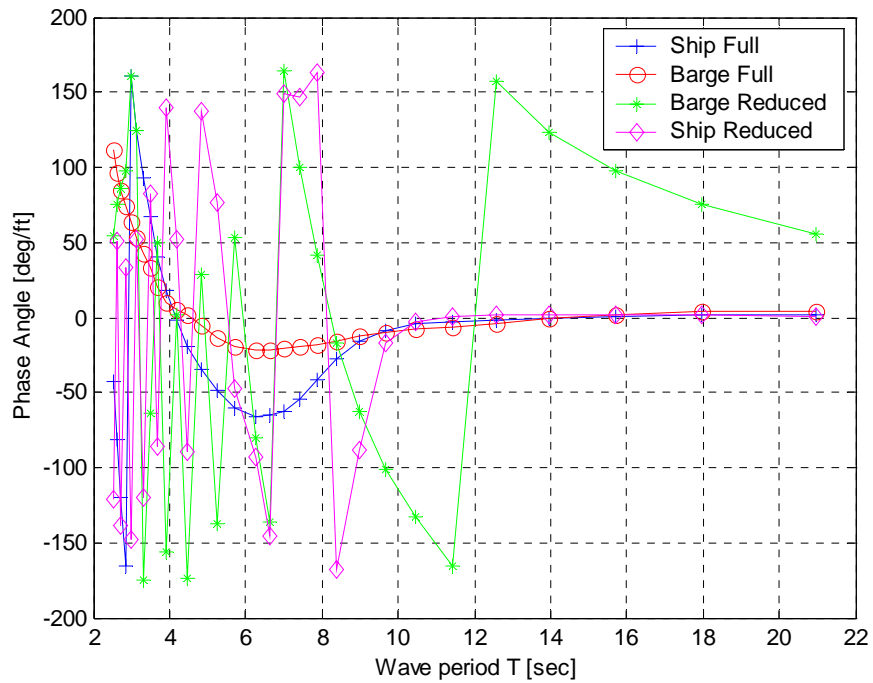


Figure A20. Comparison between Full 12x12 Solution and Reduced Approximation for the Heave Phase Angle per [ft] Wave Height at Port Beam Seas (270 deg).



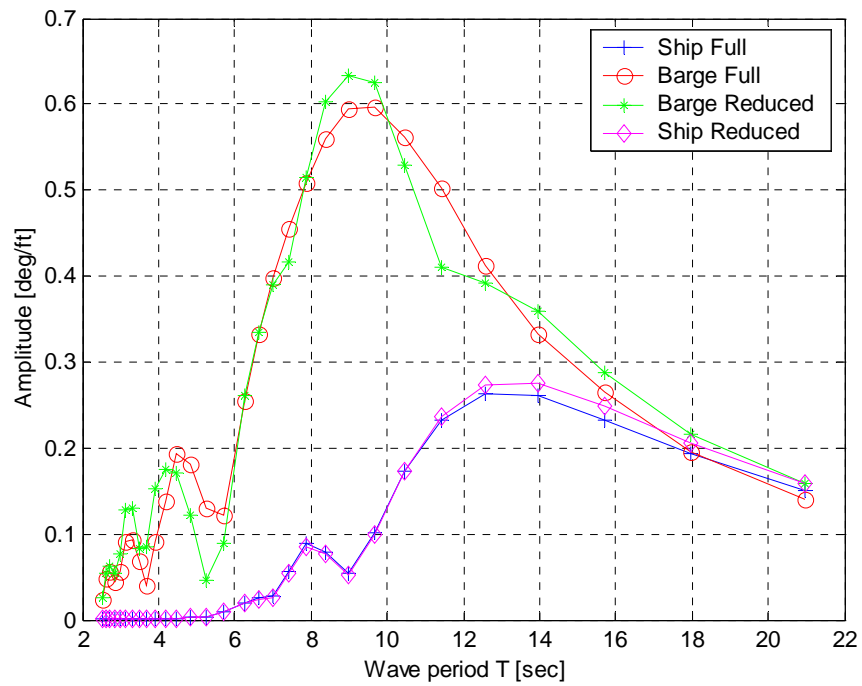


Figure A21. Comparison between Full 12x12 Solution and Reduced Approximation for the Pitch Amplitude per [ft] Wave Height at Following Seas (0 deg).

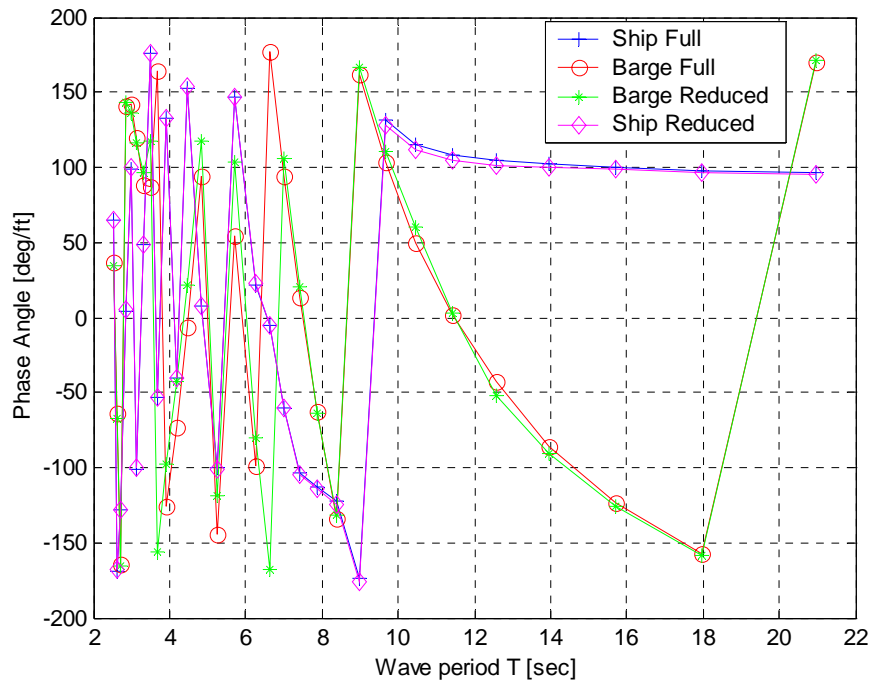


Figure A22. Comparison between Full 12x12 Solution and Reduced Approximation for the Pitch Phase Angle per [ft] Wave Height at Following Seas (0 deg).

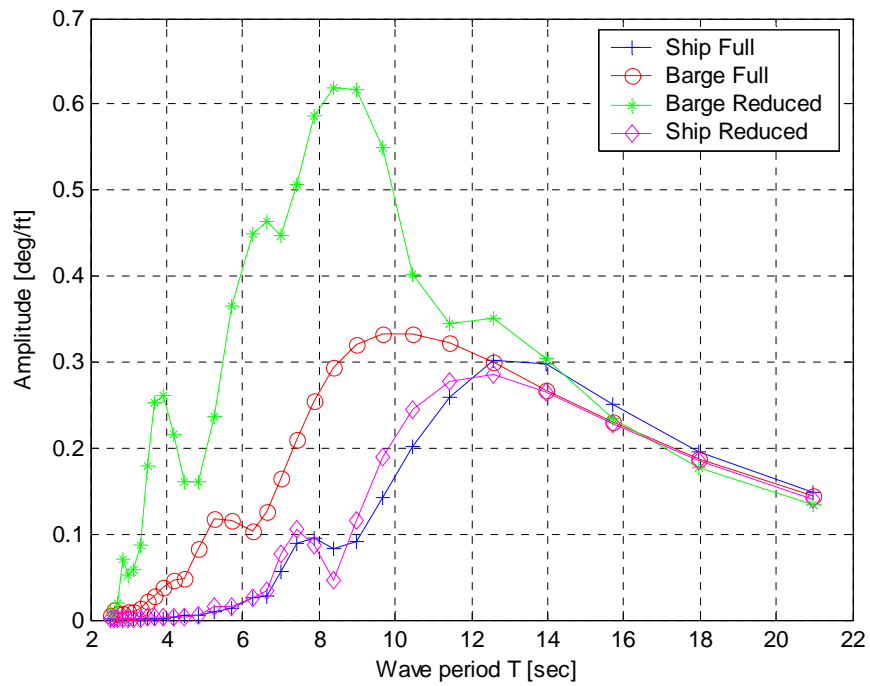


Figure A23. Comparison between Full 12x12 Solution and Reduced Approximation for the Pitch Amplitude per [ft] Wave Height at Head Seas (180 deg).

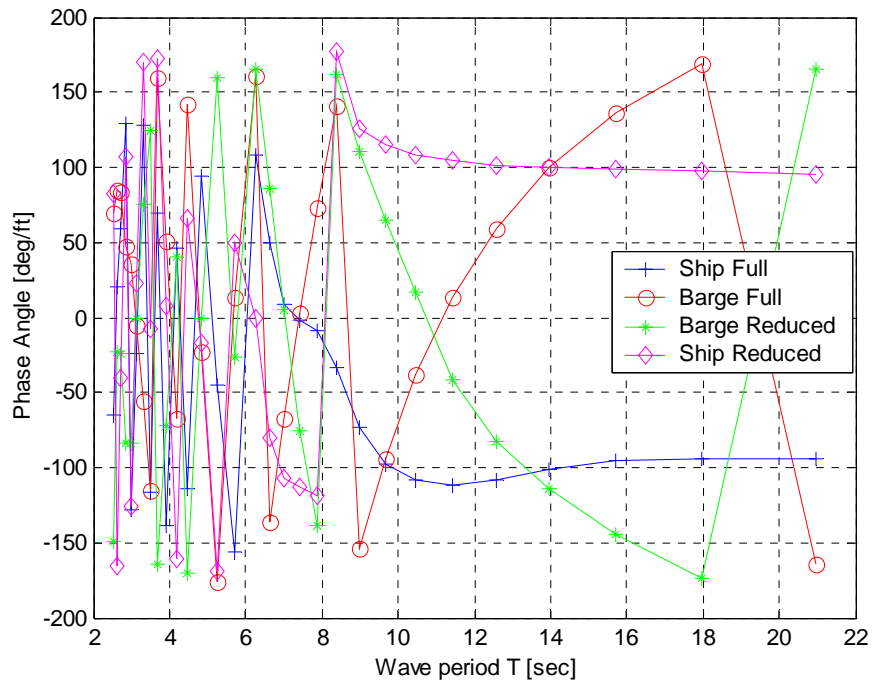


Figure A24. Comparison between Full 12x12 Solution and Reduced Approximation for the Pitch Phase Angle per [ft] Wave Height at Head Seas (180 deg).

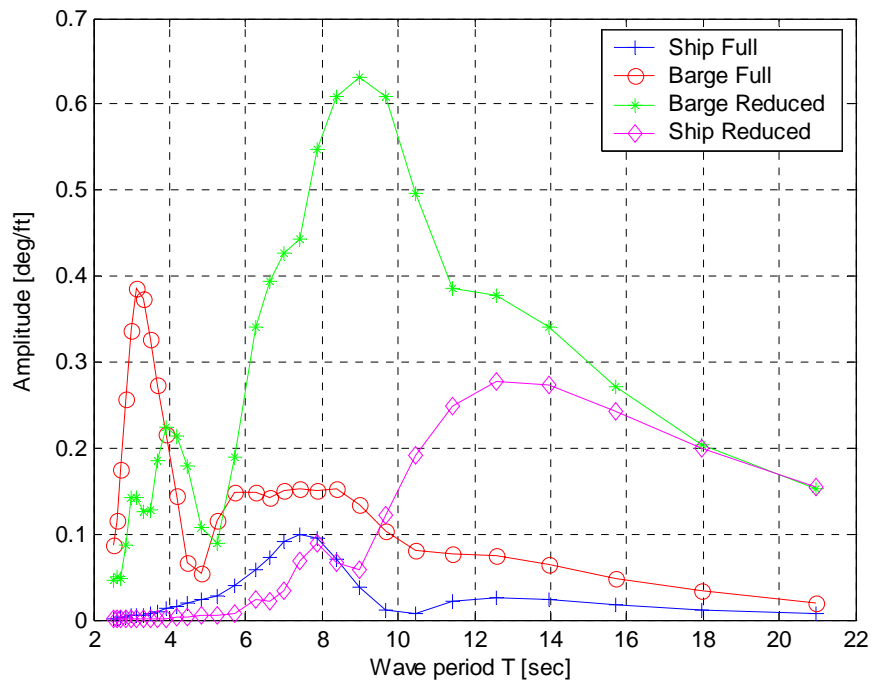


Figure A25. Comparison between Full 12x12 Solution and Reduced Approximation for the Pitch Amplitude per [ft] Wave Height at Starboard Beam Seas (90 deg).

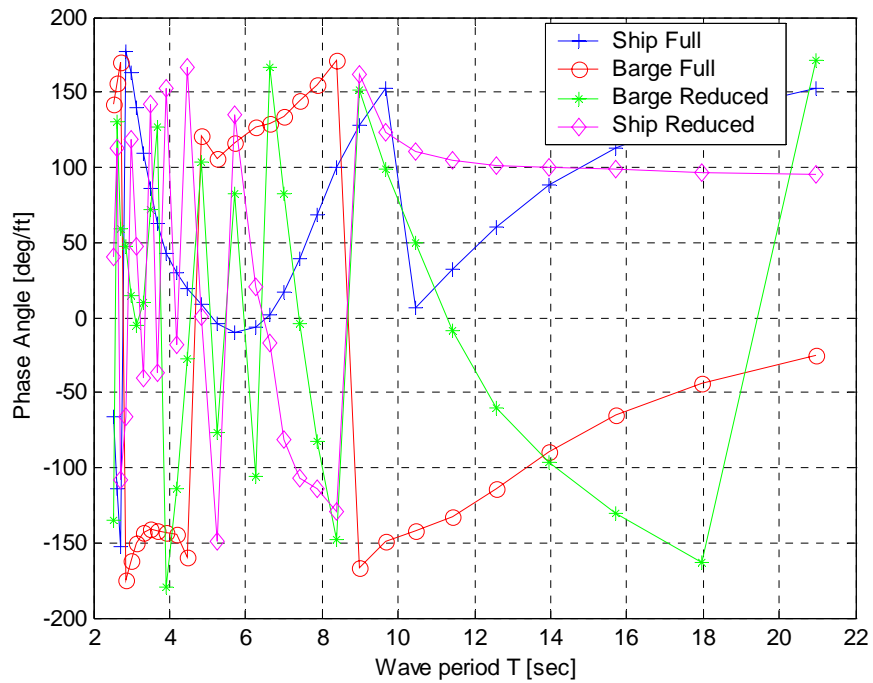


Figure A26. Comparison between Full 12x12 Solution and Reduced Approximation for the Pitch Phase Angle per [ft] Wave Height at Starboard Beam Seas (90 deg).

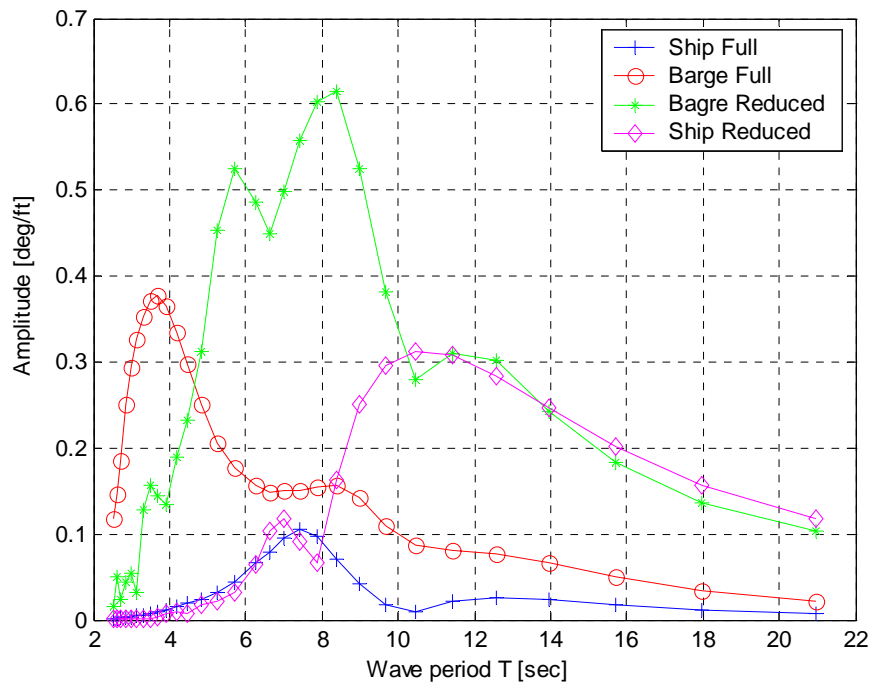


Figure A27. Comparison between Full 12x12 Solution and Reduced Approximation for the Pitch Amplitude per [ft] Wave Height at Port Beam Seas (270 deg).

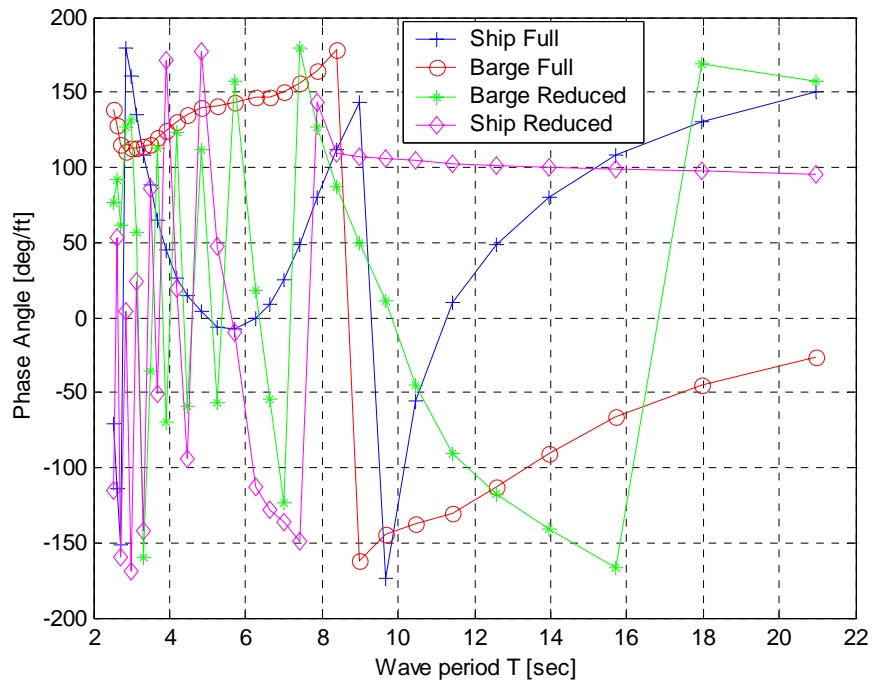


Figure A28. Comparison between Full 12x12 Solution and Reduced Approximation for the Pitch Phase Angle per [ft] Wave Height at Port Beam Seas (270 deg).

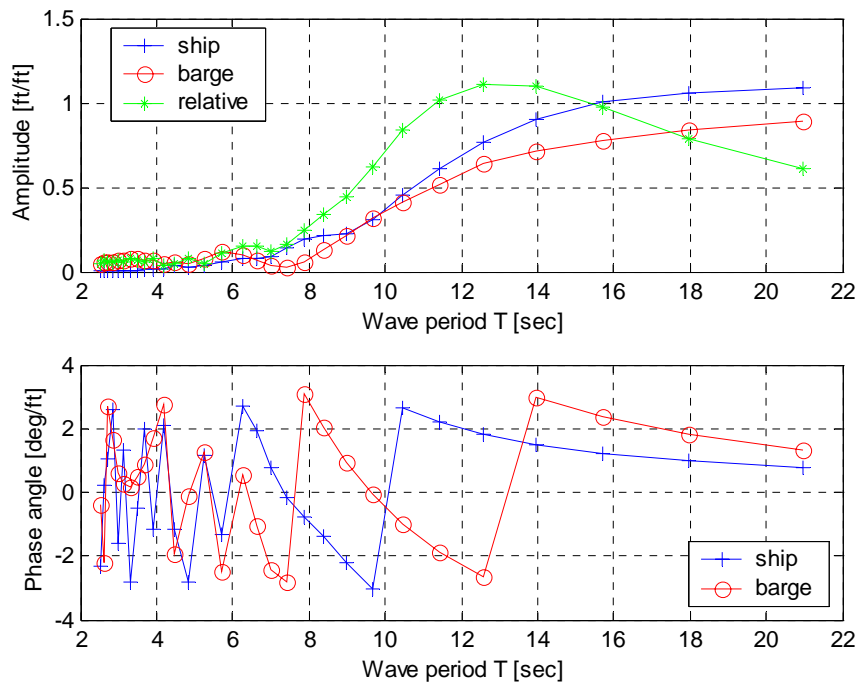


Figure A29. Plot of Vertical Motion ( $\xi$ ) per [ft] Wave Height of Connection Point A, Onboard the Ship (CAPE-D) and the Barge (RRDF) at Following Seas (0 degrees)

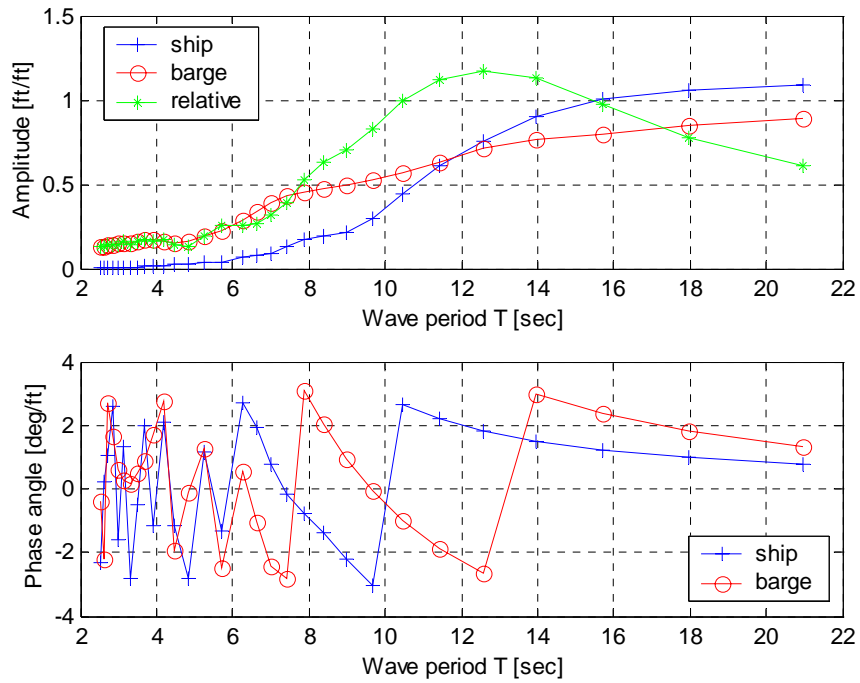


Figure A30. Plot of Vertical Motion ( $\xi$ ) per [ft] Wave Height of Connection Point B, Onboard the Ship (CAPE-D) and the Barge (RRDF) at Following Seas (0 degrees)

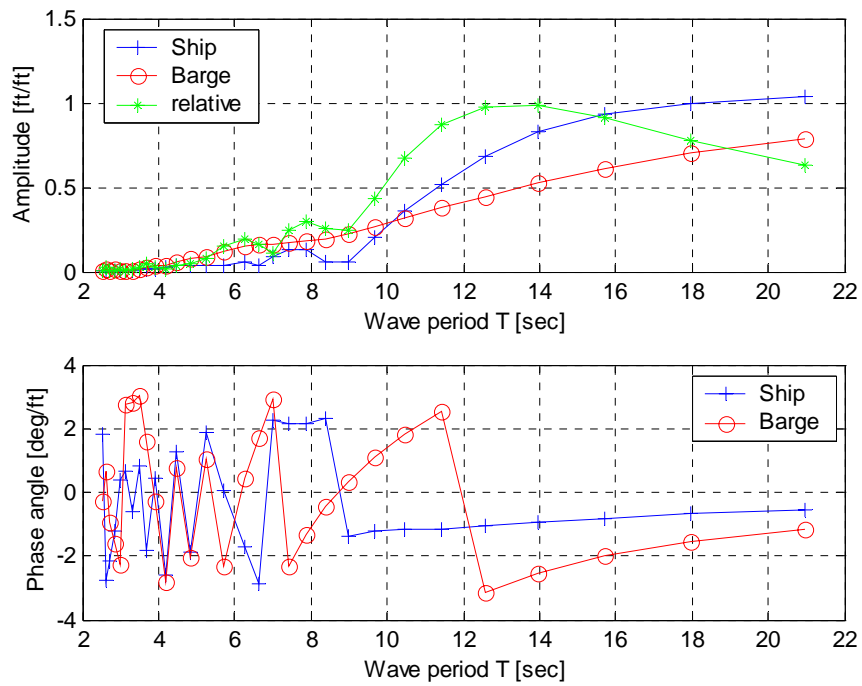


Figure A31. Plot of Vertical Motion ( $\xi$ ) per [ft] Wave Height of Connection Point A, Onboard the Ship (CAPE-D) and the Barge (RRDF) at Head Seas (180 degrees)

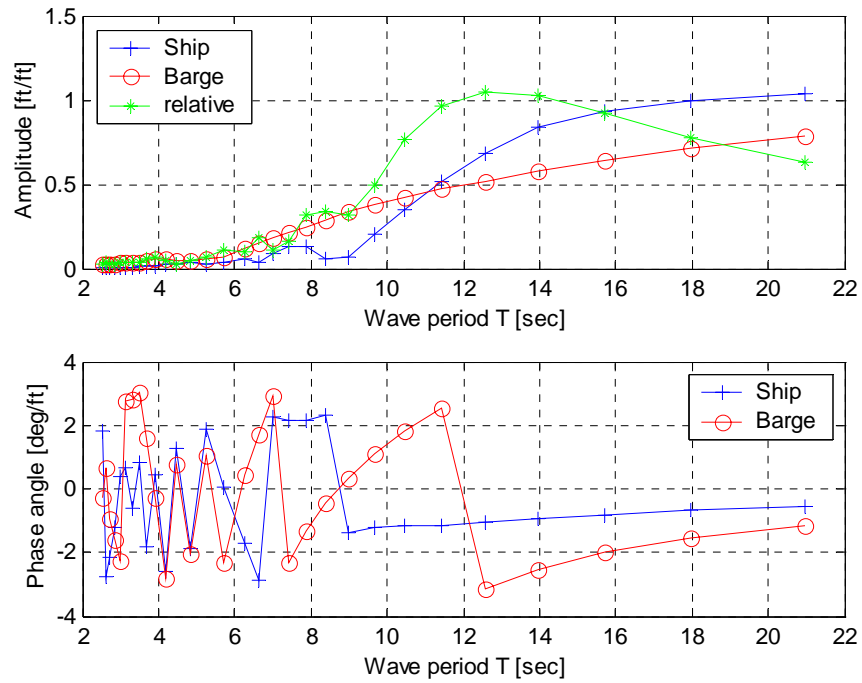


Figure A32. Plot of Vertical Motion ( $\xi$ ) per [ft] Wave Height of Connection Point B, Onboard the Ship (CAPE-D) and the Barge (RRDF) at Head Seas (180 degrees)

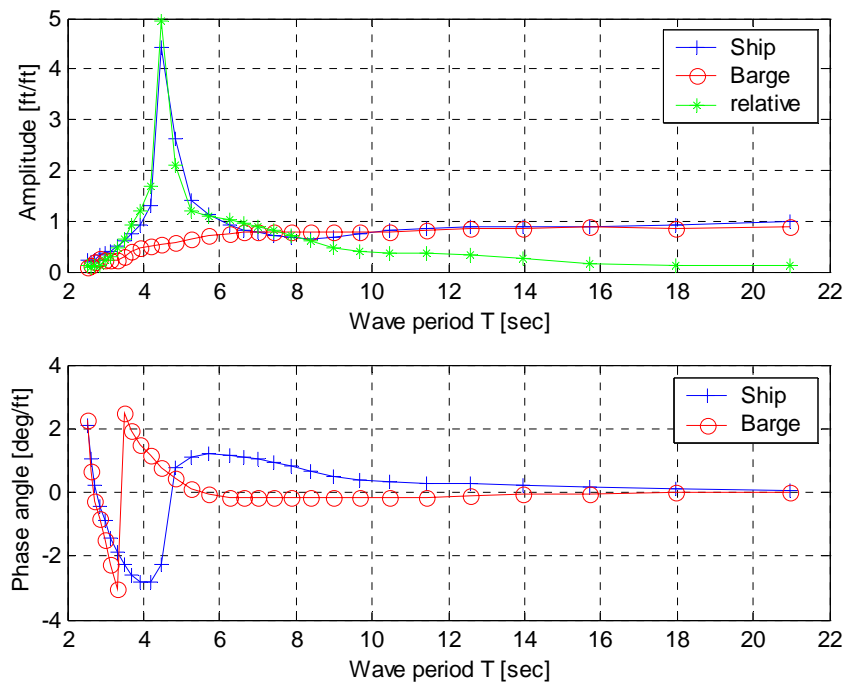


Figure A33. Plot of Vertical Motion ( $\xi$ ) per [ft] Wave Height of Connection Point A, Onboard the Ship (CAPE-D) and the Barge (RRDF) at Starboard Beam Seas (90 degrees)

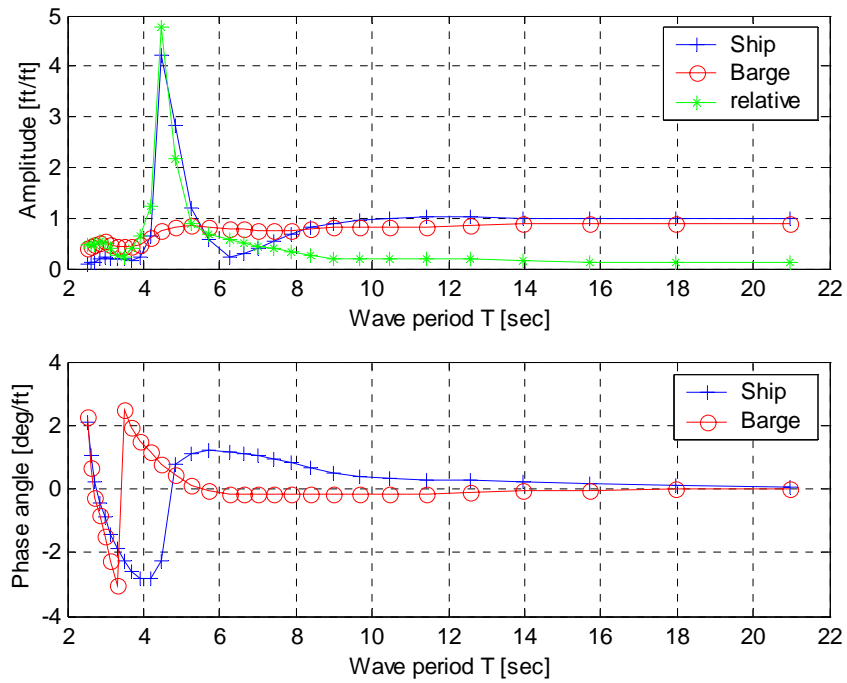


Figure A34. Plot of Vertical Motion ( $\xi$ ) per [ft] Wave Height of Connection Point B, Onboard the Ship (CAPE-D) and the Barge (RRDF) at Starboard Beam Seas (90 degrees)

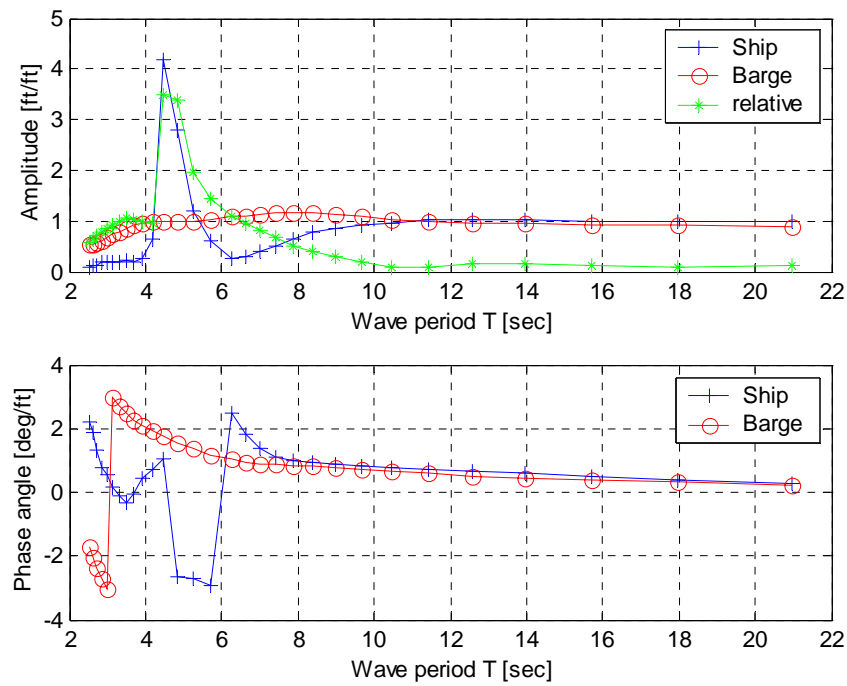


Figure A35. Plot of Vertical Motion ( $\xi$ ) per [ft] Wave Height of Connection Point A, Onboard the Ship (CAPE-D) and the Barge (RRDF) at Port Beam Seas (270 degrees)

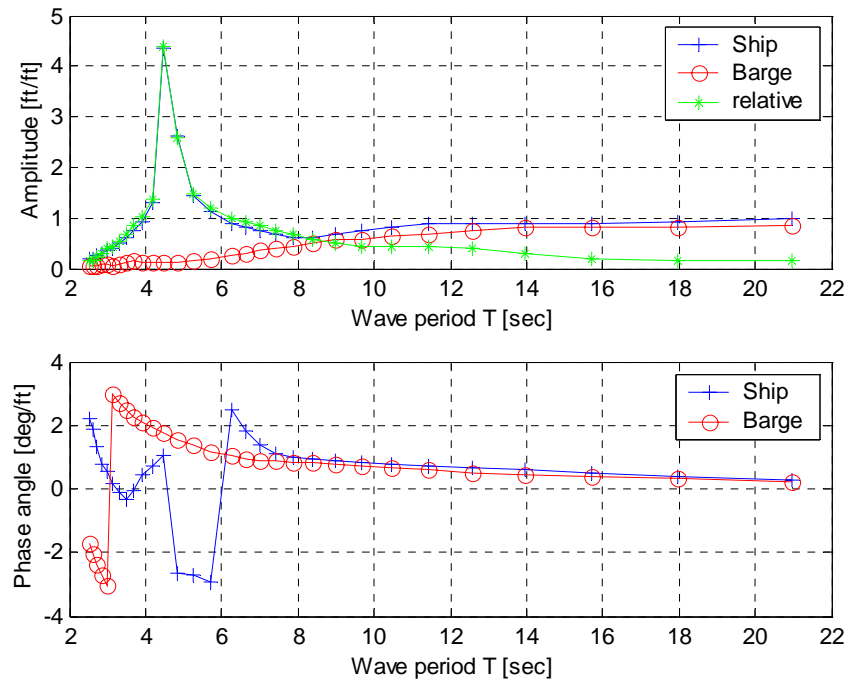


Figure A36. Plot of Vertical Motion ( $\xi$ ) per [ft] Wave Height of Connection Point B, Onboard the Ship (CAPE-D) and the Barge (RRDF) at Port Beam Seas (270 degrees)



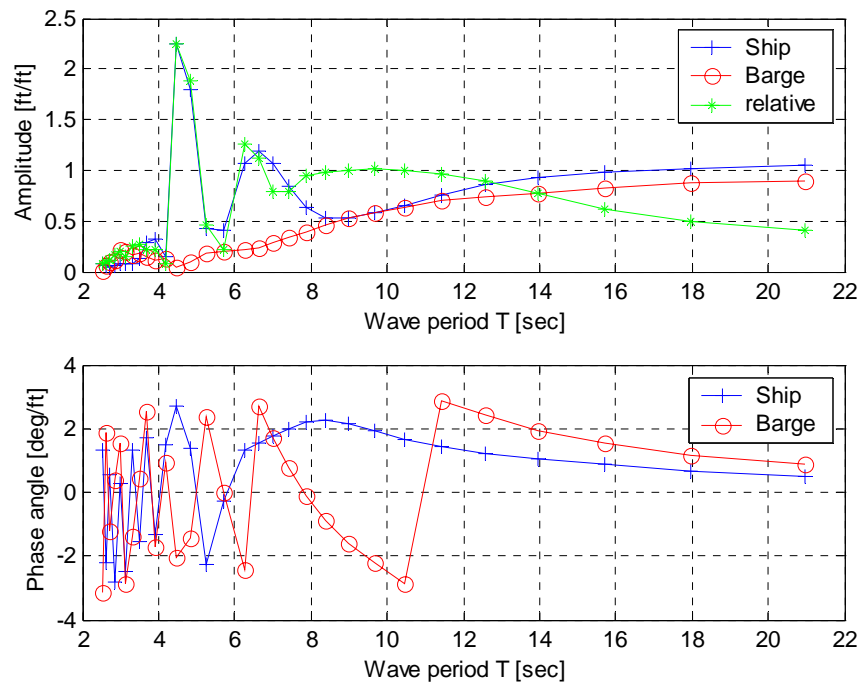


Figure A37. Plot of Vertical Motion ( $\xi$ ) per [ft] Wave Height of Connection Point A, Onboard the Ship (CAPE-D) and the Barge (RRDF) at 45 degrees Seas.

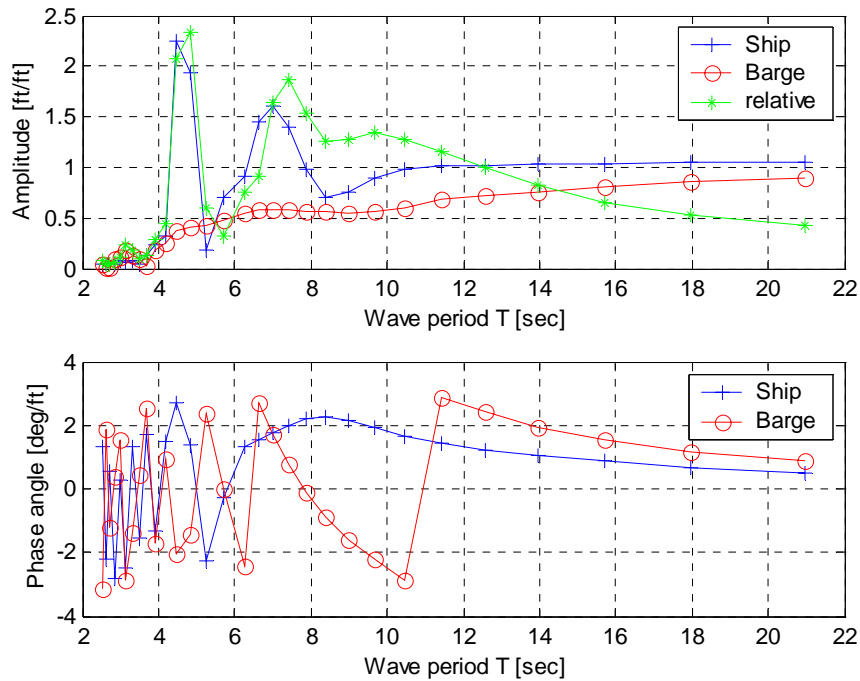


Figure A38. Plot of Vertical Motion ( $\xi$ ) per [ft] Wave Height of Connection Point B, Onboard the Ship (CAPE-D) and the Barge (RRDF) at 45 degrees Seas.

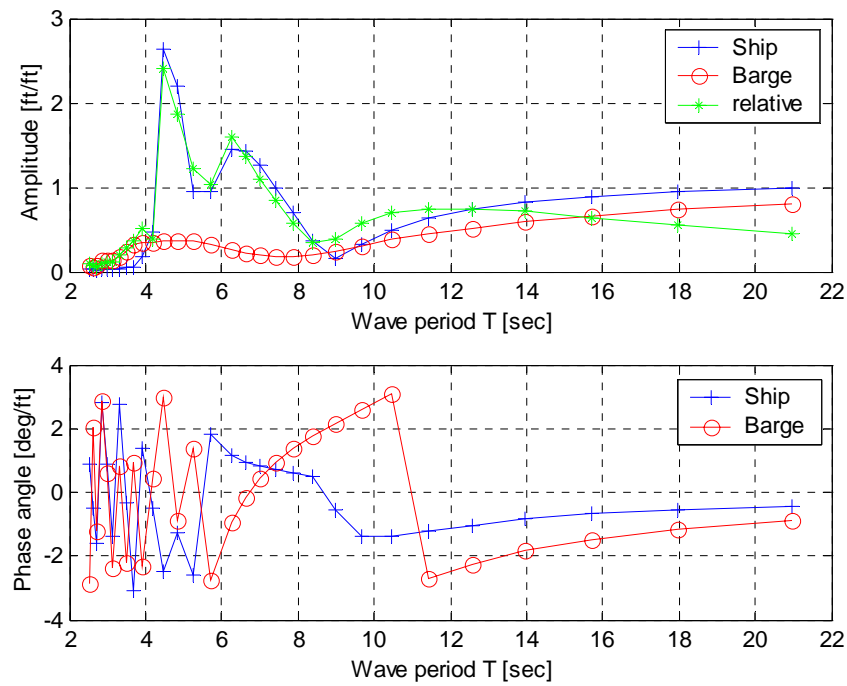


Figure A39. Plot of Vertical Motion ( $\xi$ ) per [ft] Wave Height of Connection Point A, Onboard the Ship (CAPE-D) and the Barge (RRDF) at 135 degrees Seas.

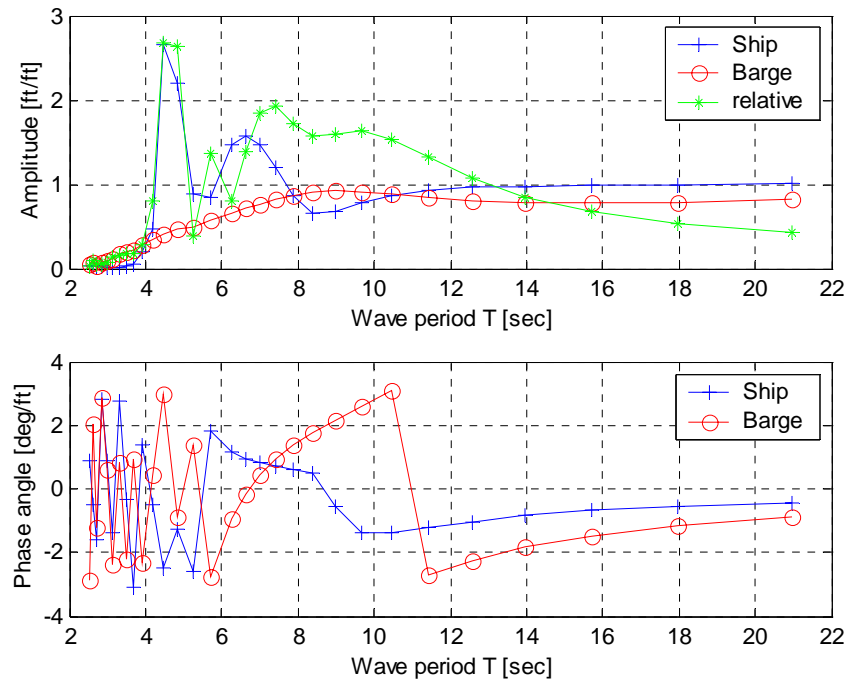


Figure A40. Plot of Vertical Motion ( $\xi$ ) per [ft] Wave Height of Connection Point B, Onboard the Ship (CAPE-D) and the Barge (RRDF) at 135 degrees Seas.

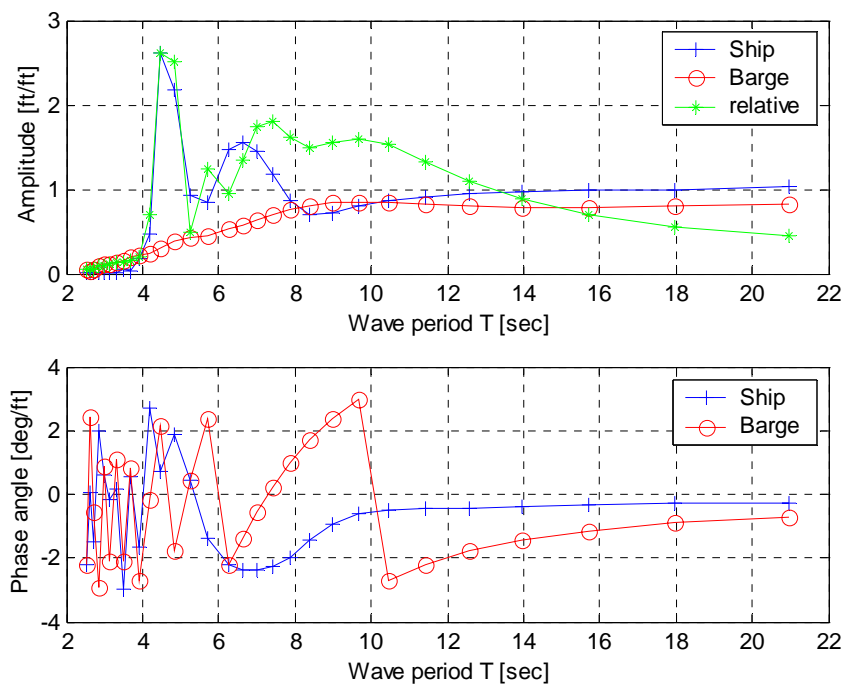


Figure A41. Plot of Vertical Motion ( $\xi$ ) per [ft] Wave Height of Connection Point A, Onboard the Ship (CAPE-D) and the Barge (RRDF) at 225 degrees Seas.

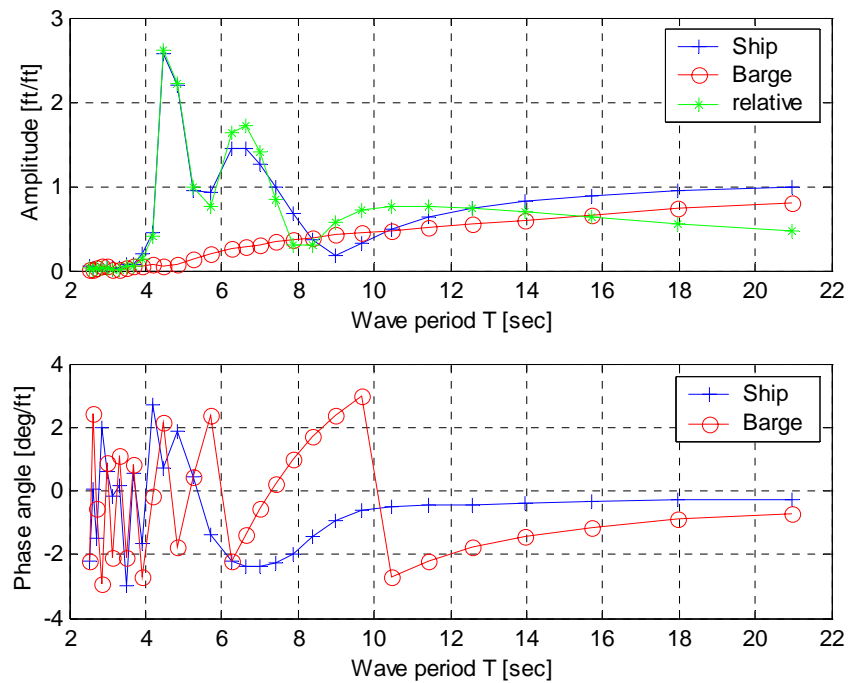


Figure A42. Plot of Vertical Motion ( $\xi$ ) per [ft] Wave Height of Connection Point B, Onboard the Ship (CAPE-D) and the Barge (RRDF) at 225 degrees Seas.

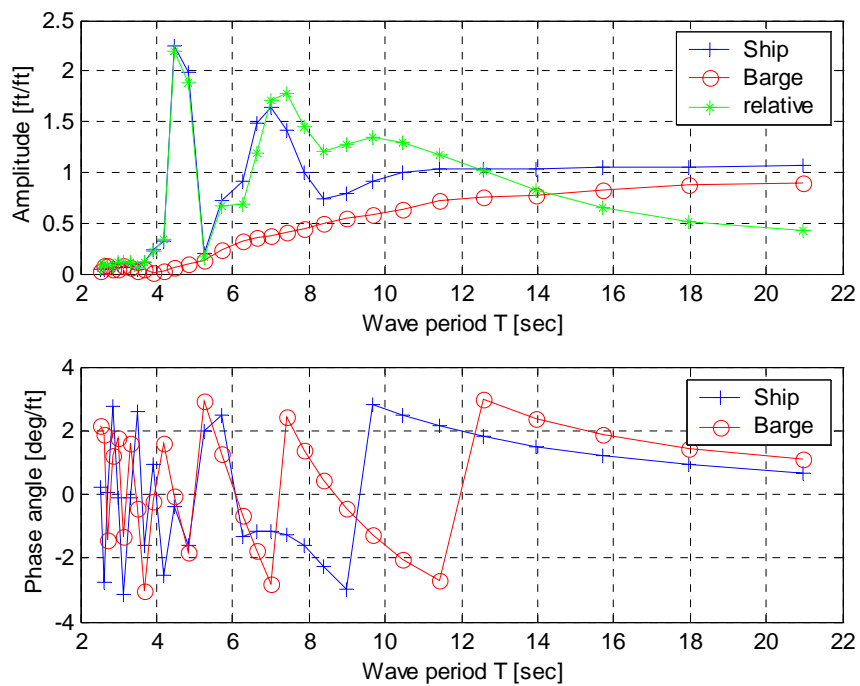


Figure A43. Plot of Vertical Motion ( $\xi$ ) per [ft] Wave Height of Connection Point A, Onboard the Ship (CAPE-D) and the Barge (RRDF) at 315 degrees Seas.

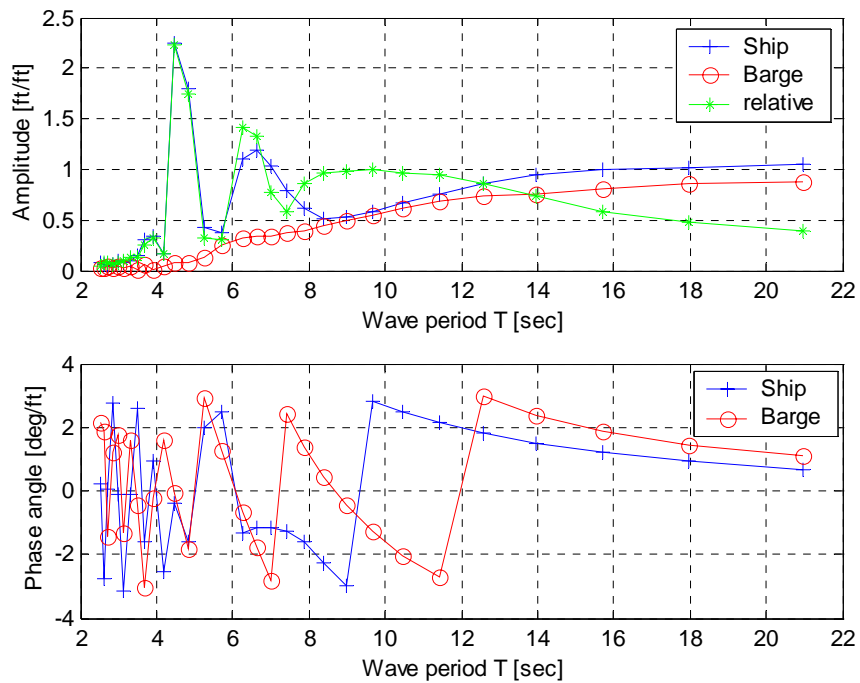


Figure A44. Plot of Vertical Motion ( $\xi$ ) per [ft] Wave Height of Connection Point B, Onboard the Ship (CAPE-D) and the Barge (RRDF) at 315 degrees Seas.

THIS PAGE INTENTIONALLY LEFT BLANK

## APPENDIX B

Length of the Ramp	$L = 100\text{ ft } (30.5m)$
Width of the Ramp	$B = 25\text{ ft } (7.6m)$
Mass Density of the Ramp	$0.284\text{ lb} / \text{in}^3$
Young's Module for Stress Calculations	$E = 29 \times 10^6\text{ psi } (200GPa)$
Spring Stiffness between Ramp and Barge	$k = 205.6 \times 10^2\text{ lbf} / \text{ft } (3 \times 10^5 [N / m])$
Damping between Ramp and Barge	$c = 4 \times 10^2\text{ lbf} \cdot \text{s} / \text{ft } (5.9 \times 10^3 [Ns / m])$

Table 2      Parameters used in the Numerical Solution

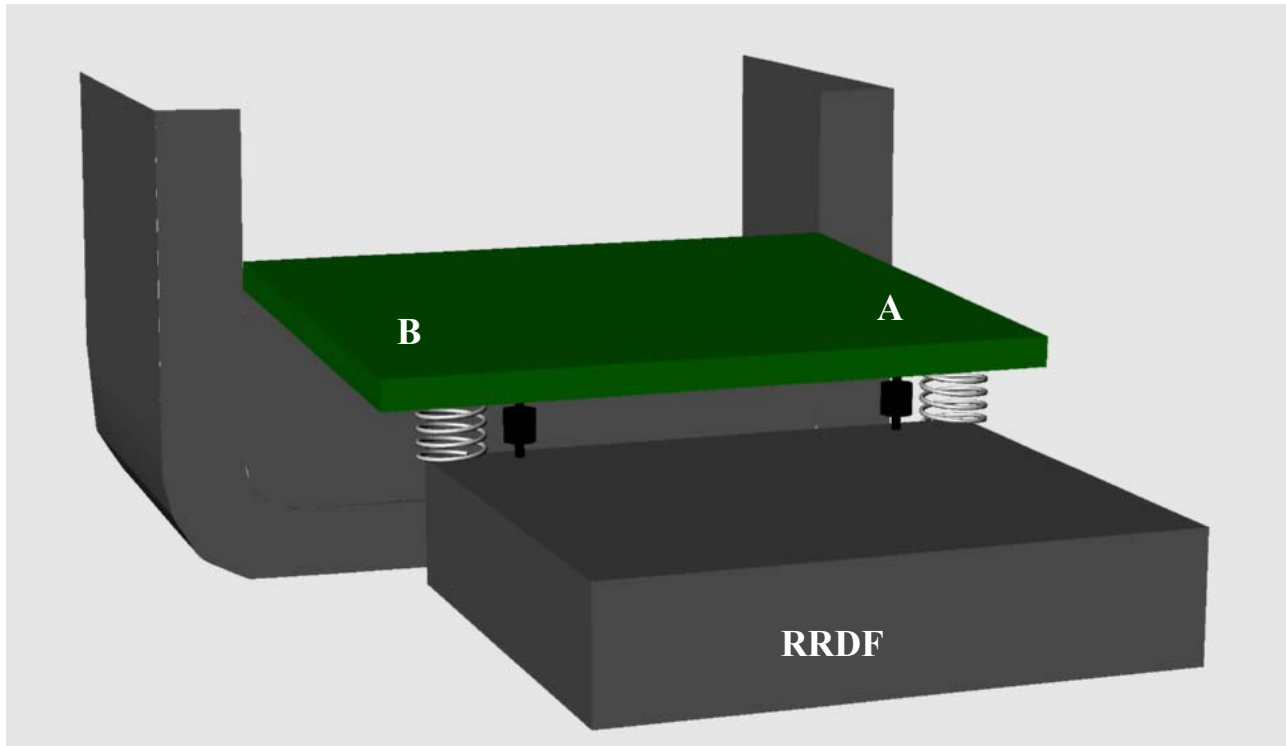


Figure 7.      Sketch of the Ship-Stern Ramp-Barge Arrangement.

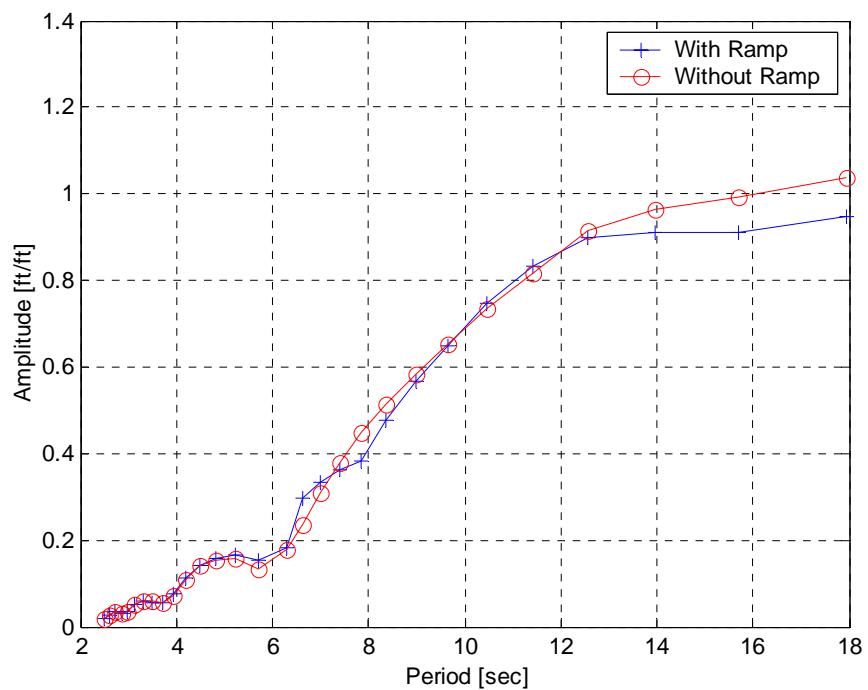


Figure B1. Effect of Ramp on Barge (RRDF) Heave Amplitude per [ft] Wave Height, at Following Seas (0 degrees).

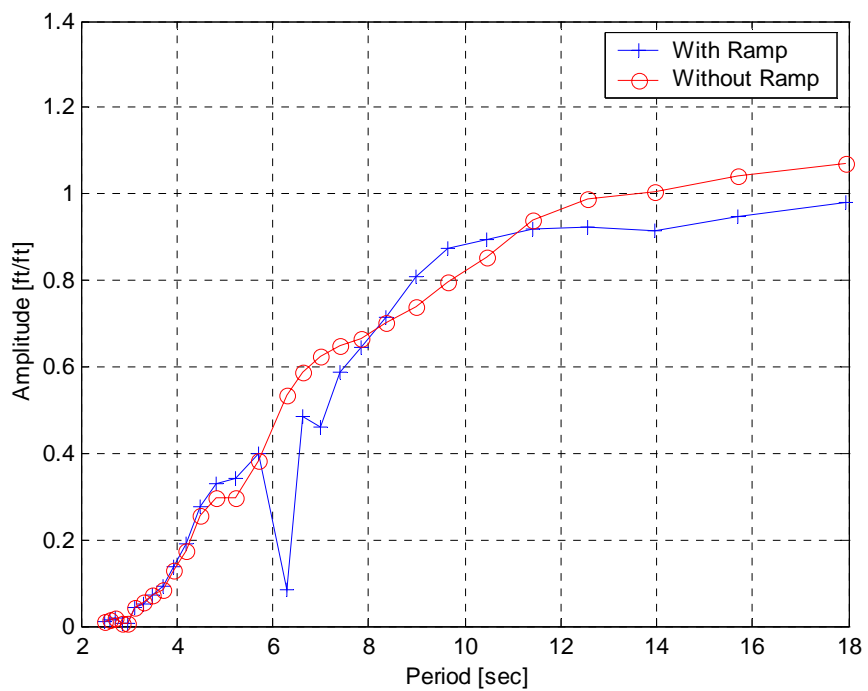


Figure B2. Effect of Ramp on Barge (RRDF) Heave Amplitude per [ft] Wave Height, at Quartering Seas (45 degrees).

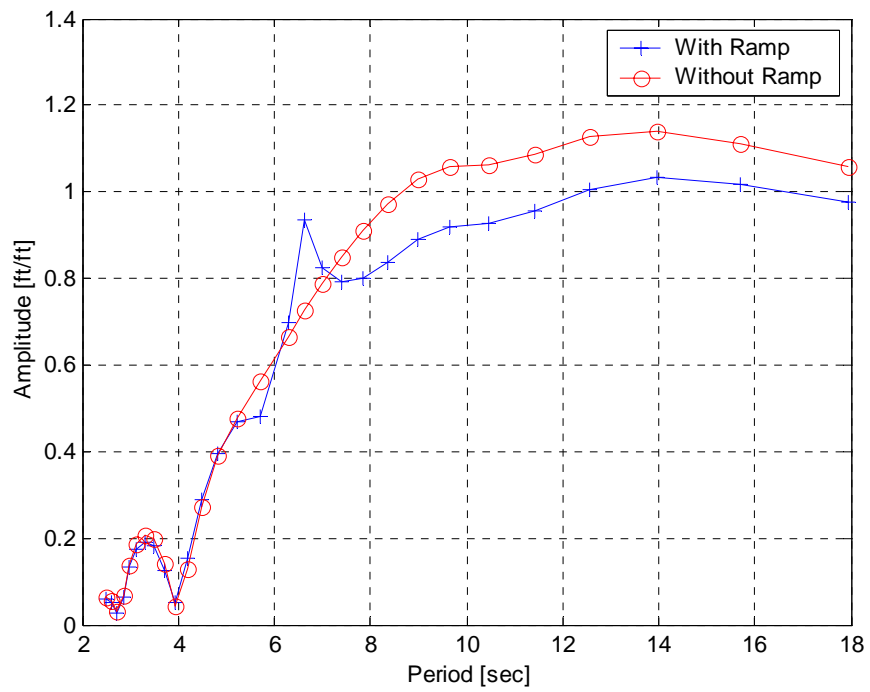


Figure B3. Effect of Ramp on Barge (RRDF) Heave Amplitude per [ft] Wave Height, at Starboard Beam Seas (90 degrees).

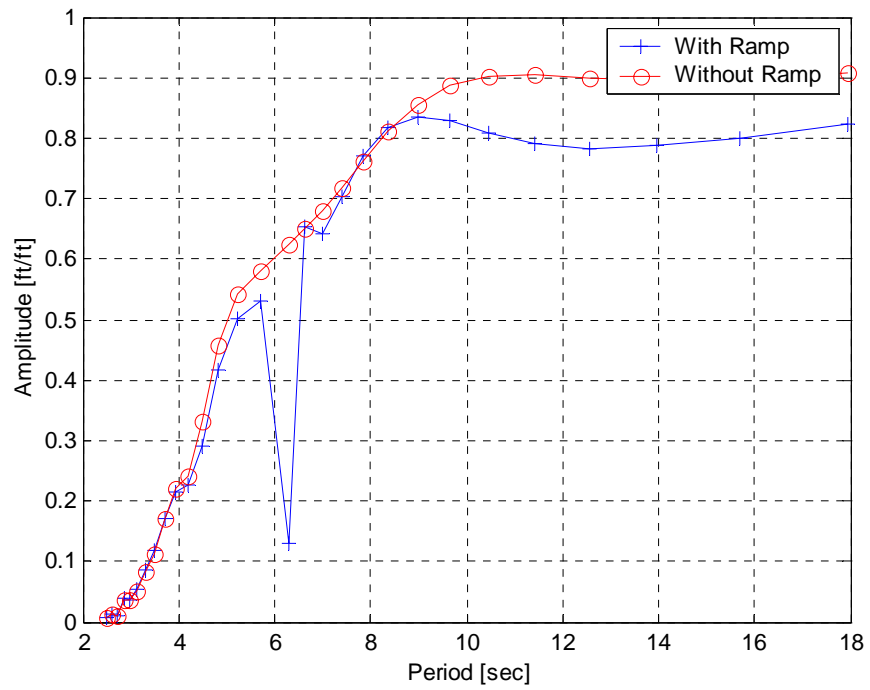


Figure B4. Effect of Ramp on Barge (RRDF) Heave Amplitude per [ft] Wave Height, at Quartering Seas (135 degrees).



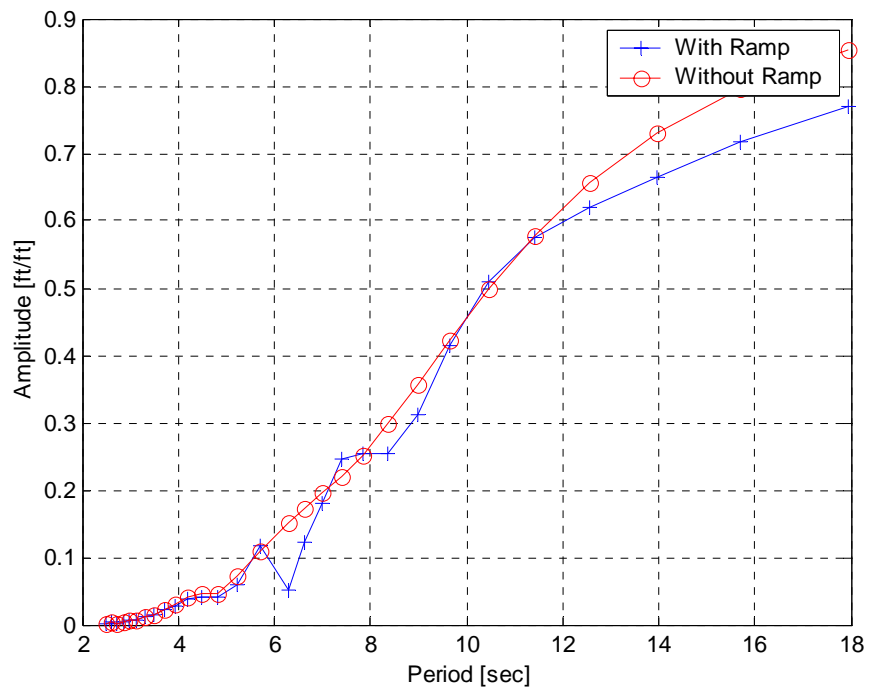


Figure B5. Effect of Ramp on Barge (RRDF) Heave Amplitude per [ft] Wave Height, at Head Seas (180 degrees).

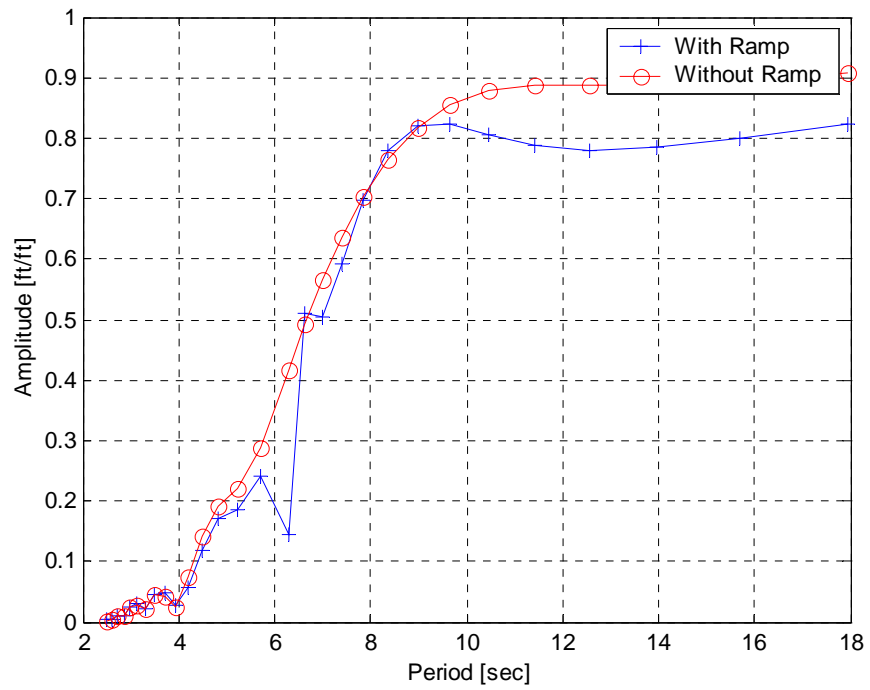


Figure B6. Effect of Ramp on Barge (RRDF) Heave Amplitude per [ft] Wave Height, at Quartering Seas (225 degrees).

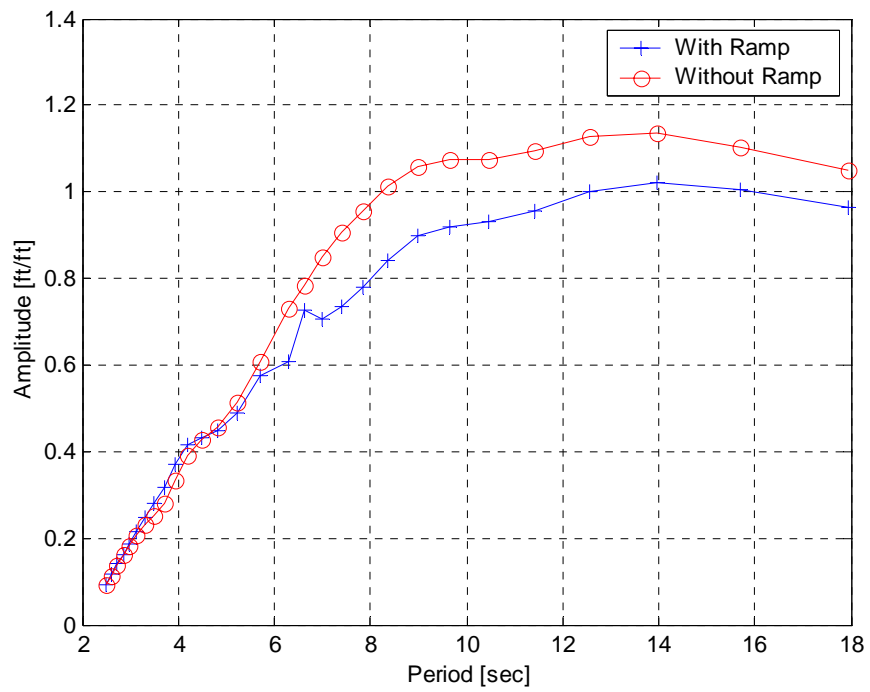


Figure B7. Effect of Ramp on Barge (RRDF) Heave Amplitude per [ft] Wave Height, at Port Beam Seas (270 degrees).

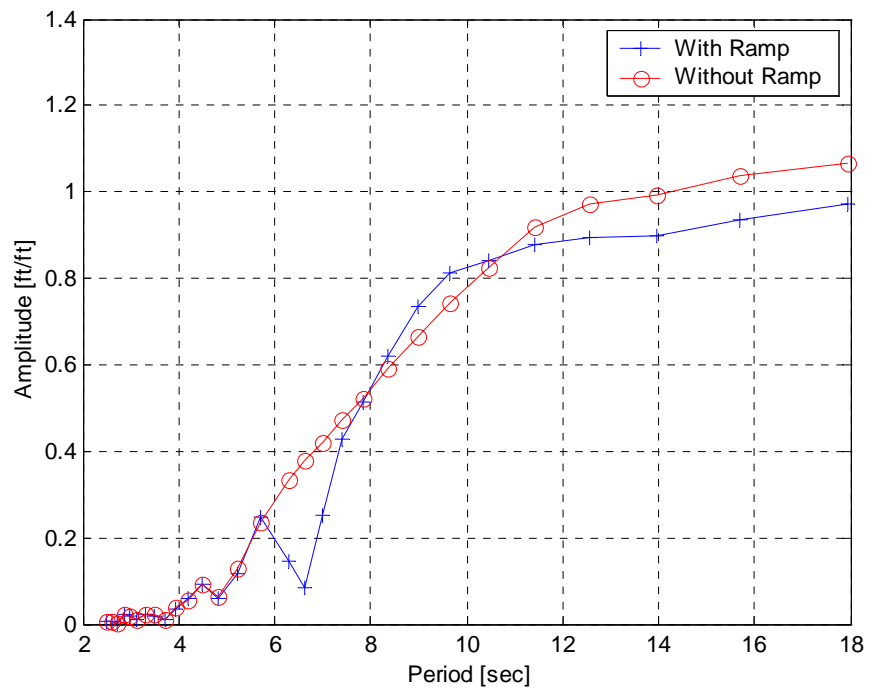


Figure B8. Effect of Ramp on Barge (RRDF) Heave Amplitude per [ft] Wave Height, at Quartering Seas (315 degrees).

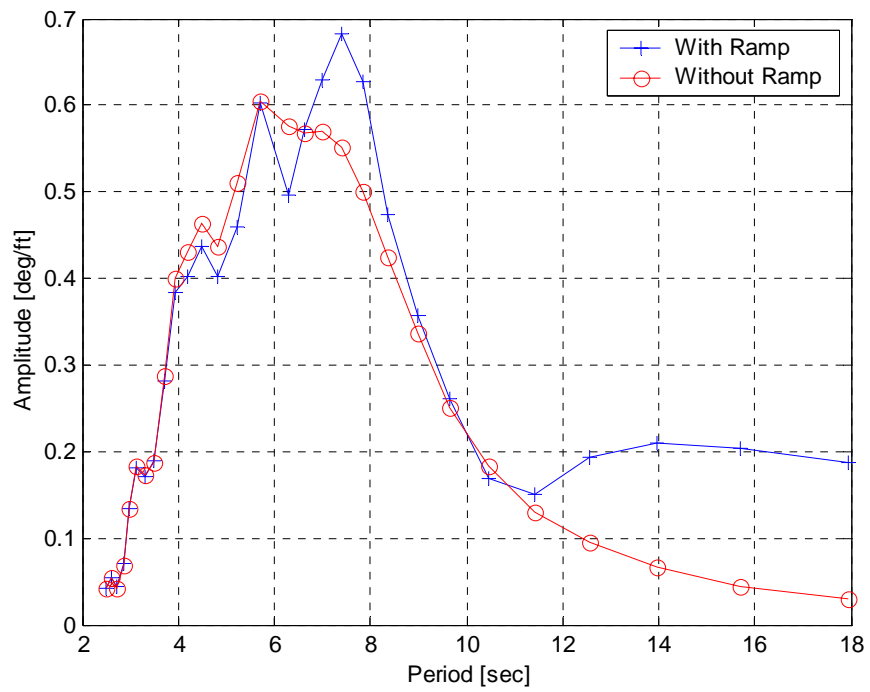


Figure B9. Effect of Ramp on Barge (RRDF) Roll Amplitude per [ft] Wave Height, at Following Seas (0 degrees).

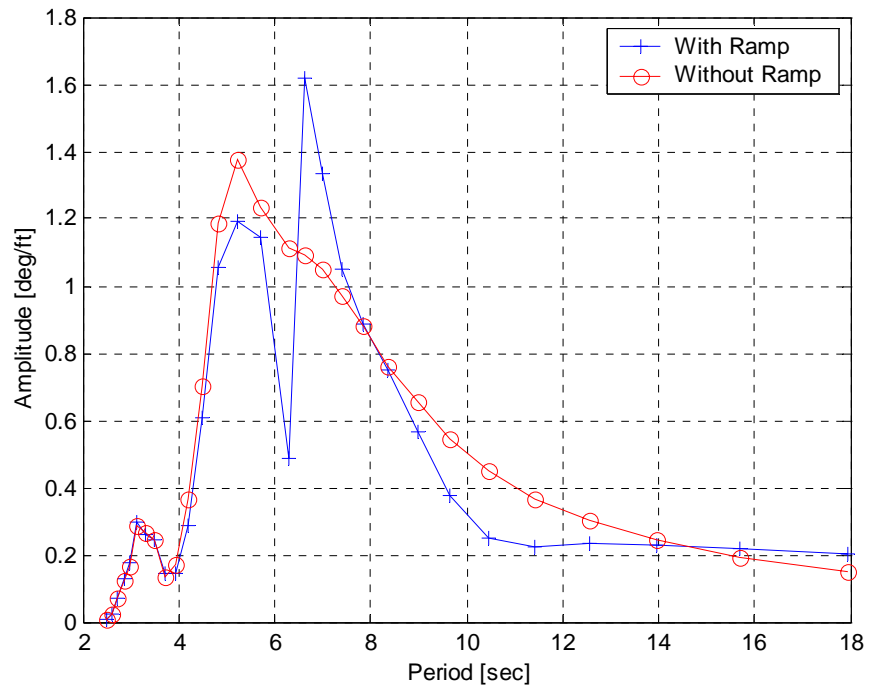


Figure B10. Effect of Ramp on Barge (RRDF) Roll Amplitude per [ft] Wave Height, at Quartering Seas (45 degrees).

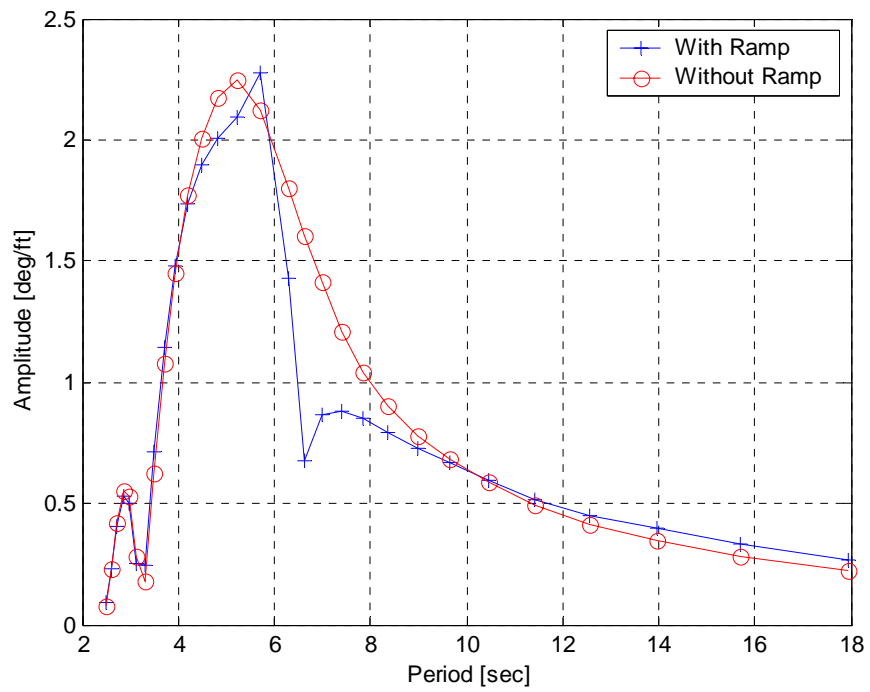


Figure B11. Effect of Ramp on Barge (RRDF) Roll Amplitude per [ft] Wave Height, at Starboard Beam Seas (90 degrees).

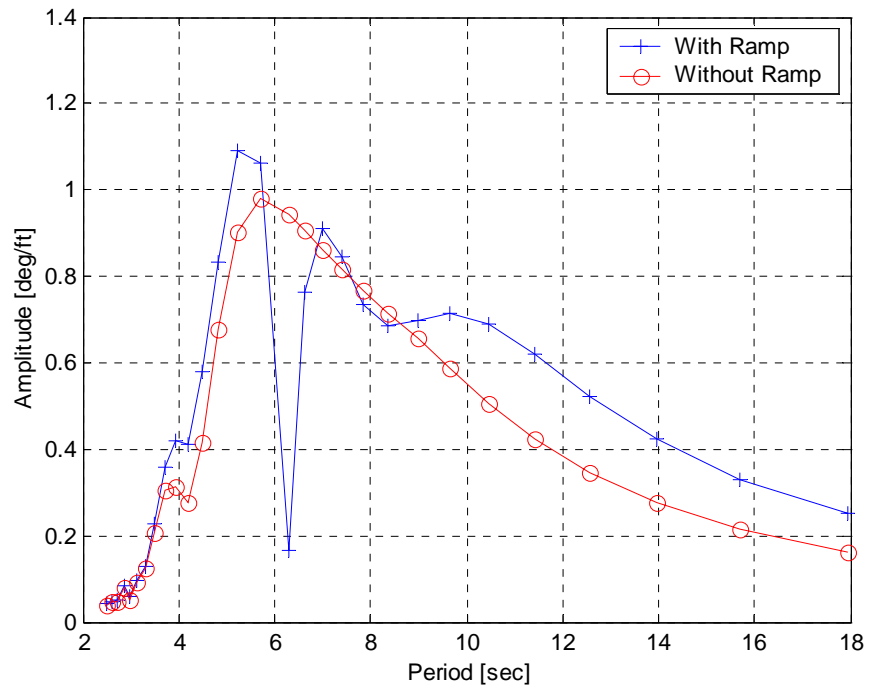


Figure B12. Effect of Ramp on Barge (RRDF) Roll Amplitude per [ft] Wave Height, at Quartering Seas (135 degrees).

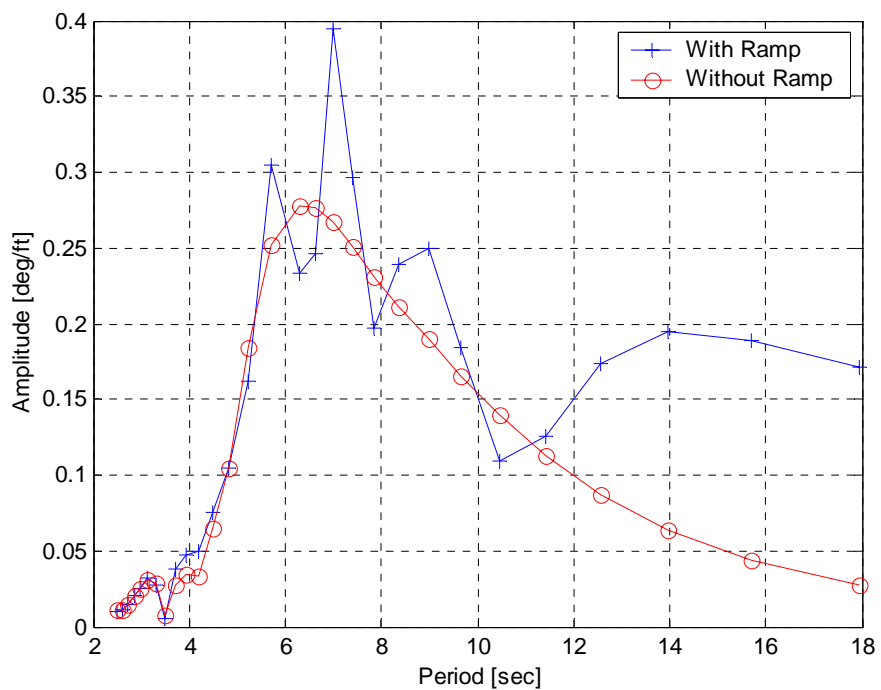


Figure B13. Effect of Ramp on Barge (RRDF) Roll Amplitude per [ft] Wave Height, at Head Seas (180 degrees).

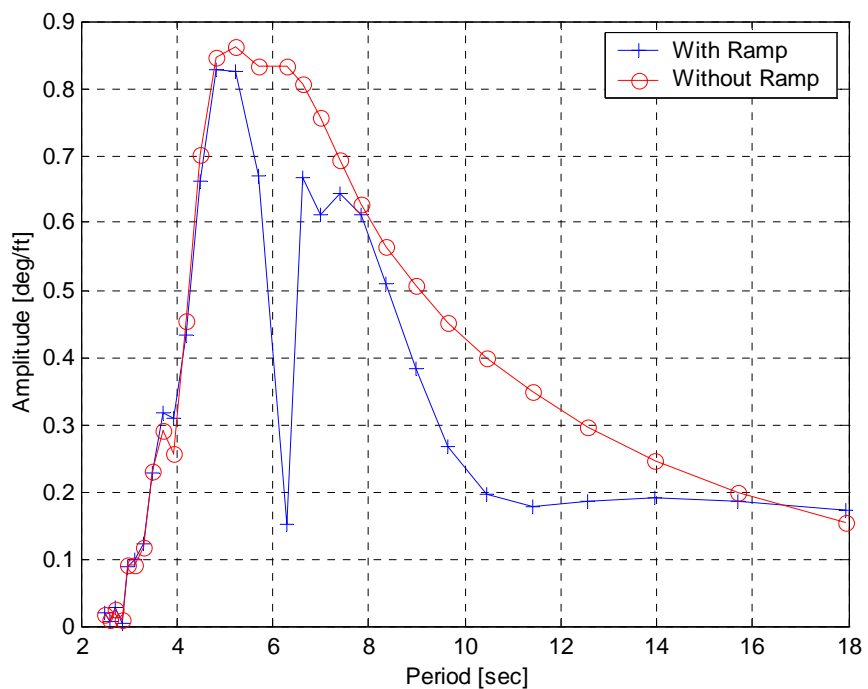


Figure B14. Effect of Ramp on Barge (RRDF) Roll Amplitude per [ft] Wave Height, at Quartering Seas (225 degrees).

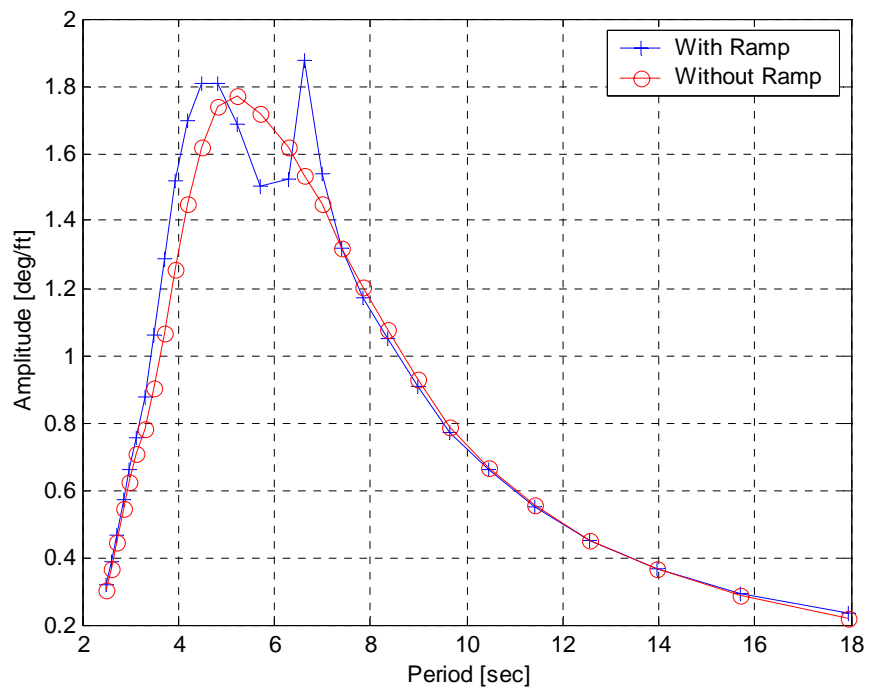


Figure B15. Effect of Ramp on Barge (RRDF) Roll Amplitude per [ft] Wave Height, at Port Beam Seas (270 degrees).

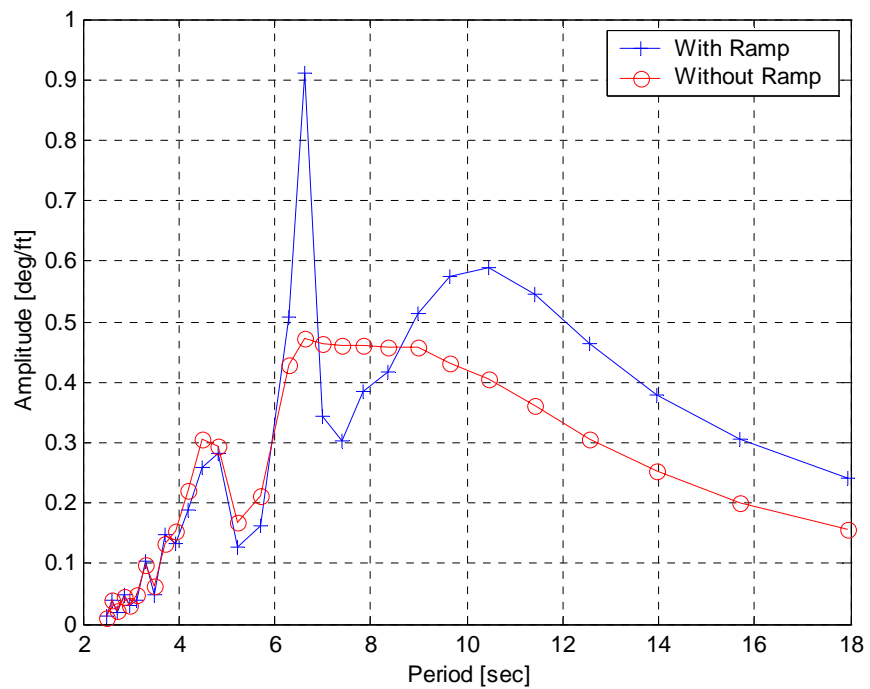


Figure B16. Effect of Ramp on Barge (RRDF) Roll Amplitude per [ft] Wave Height, at Quartering Seas (315 degrees).

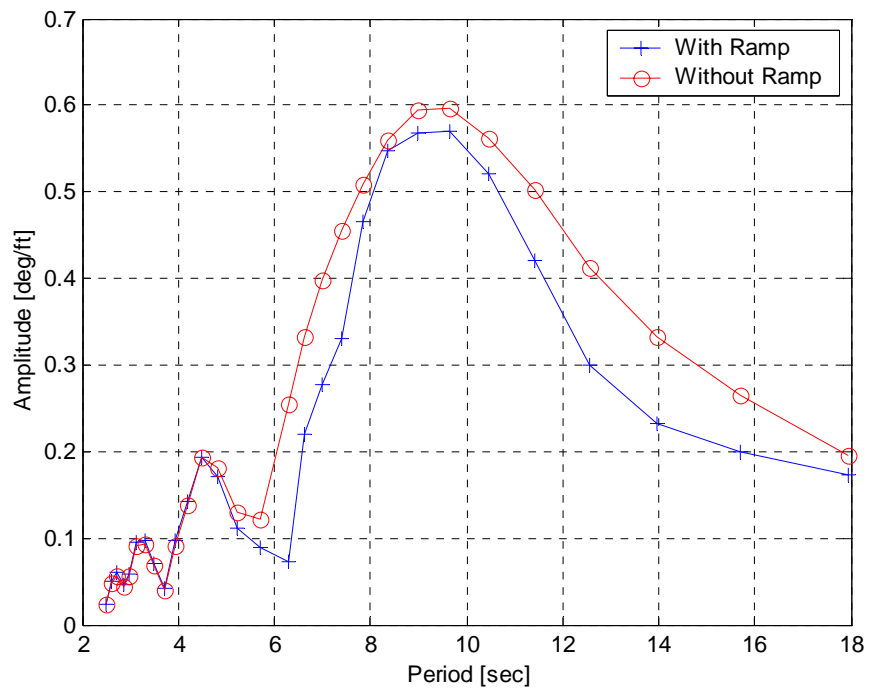


Figure B17. Effect of Ramp on Barge (RRDF) Pitch Amplitude per [ft] Wave Height, at Following Seas (0 degrees).

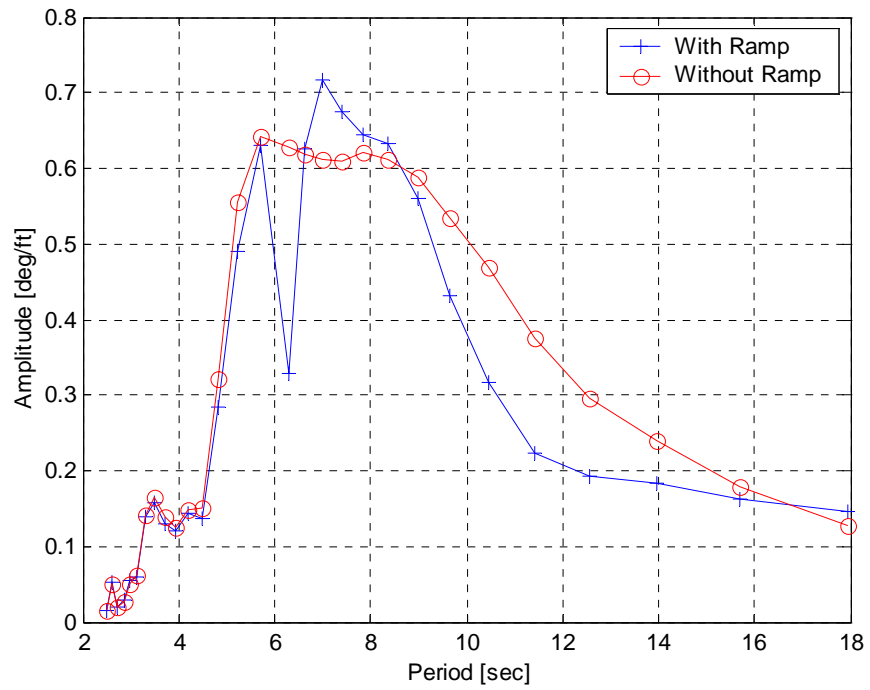


Figure B18. Effect of Ramp on Barge (RRDF) Pitch Amplitude per [ft] Wave Height, at Quartering Seas (45 degrees).

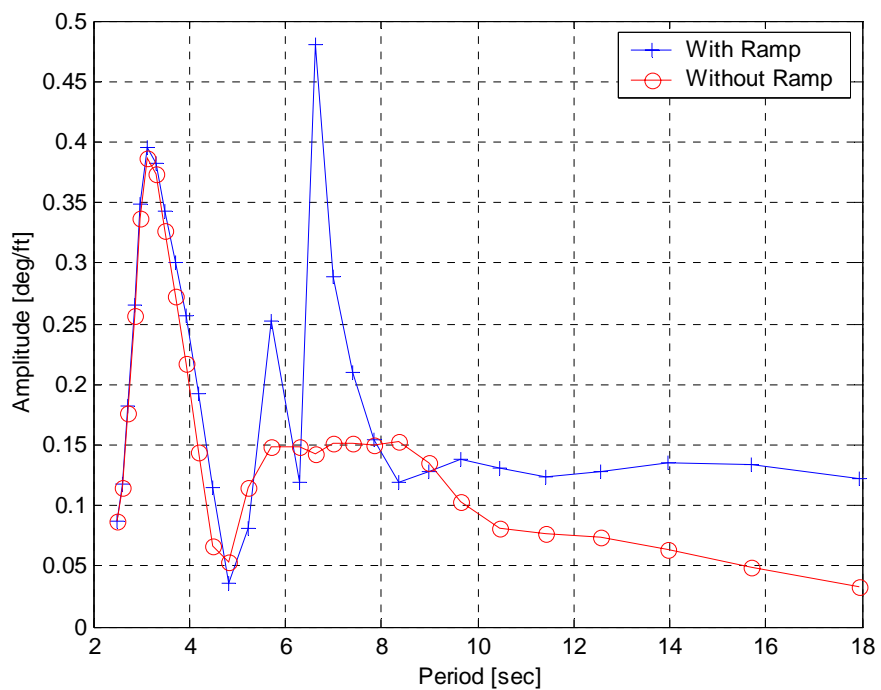


Figure B19. Effect of Ramp on Barge (RRDF) Pitch Amplitude per [ft] Wave Height, at Starboard Beam Seas (90 degrees).

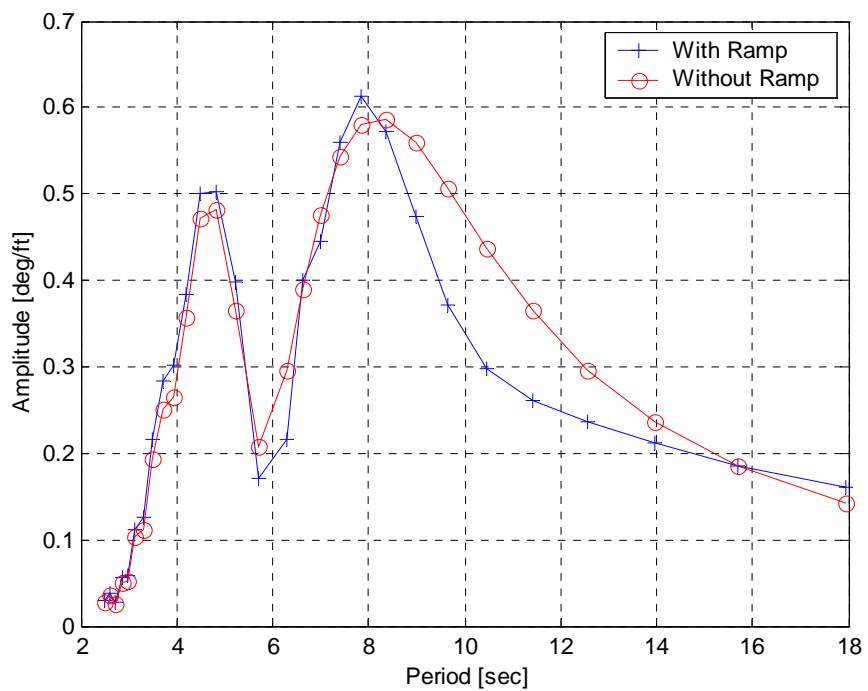


Figure B20. Effect of Ramp on Barge (RRDF) Pitch Amplitude per [ft] Wave Height, at Quartering Seas (135 degrees).



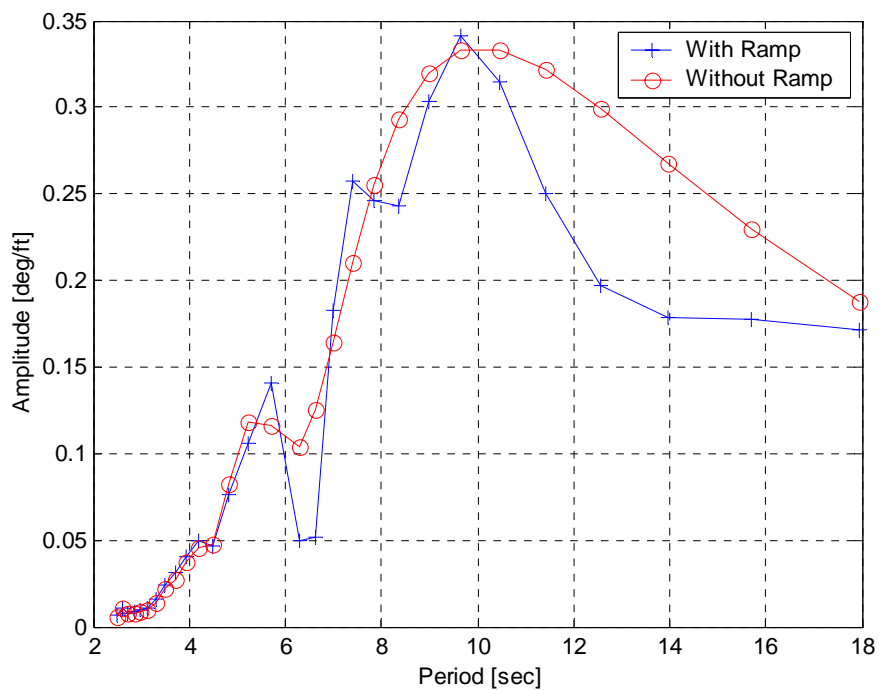


Figure B21. Effect of Ramp on Barge (RRDF) Pitch Amplitude per [ft] Wave Height, at Head Seas (180 degrees).

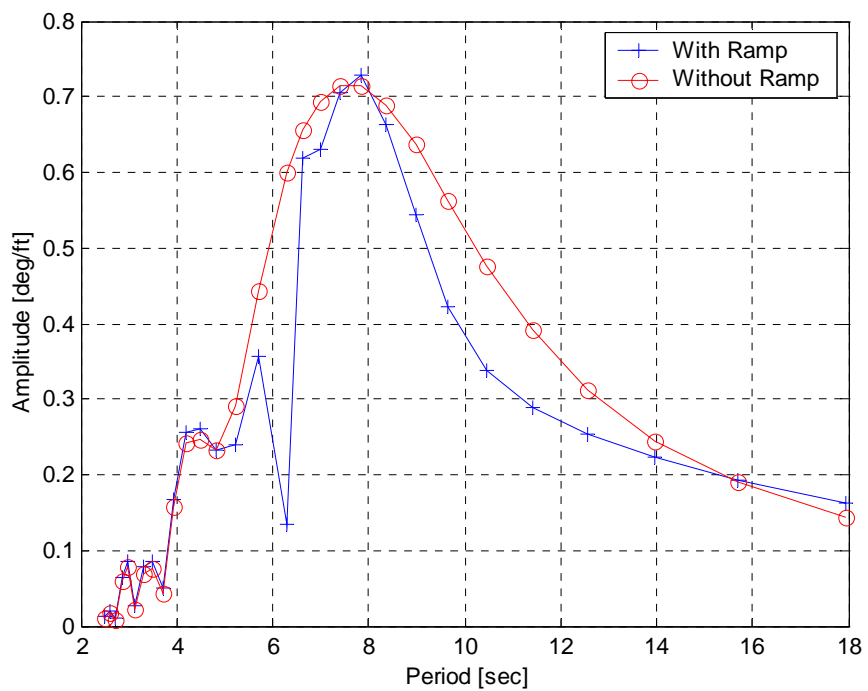


Figure B22. Effect of Ramp on Barge (RRDF) Pitch Amplitude per [ft] Wave Height, at Quartering Seas (225 degrees).

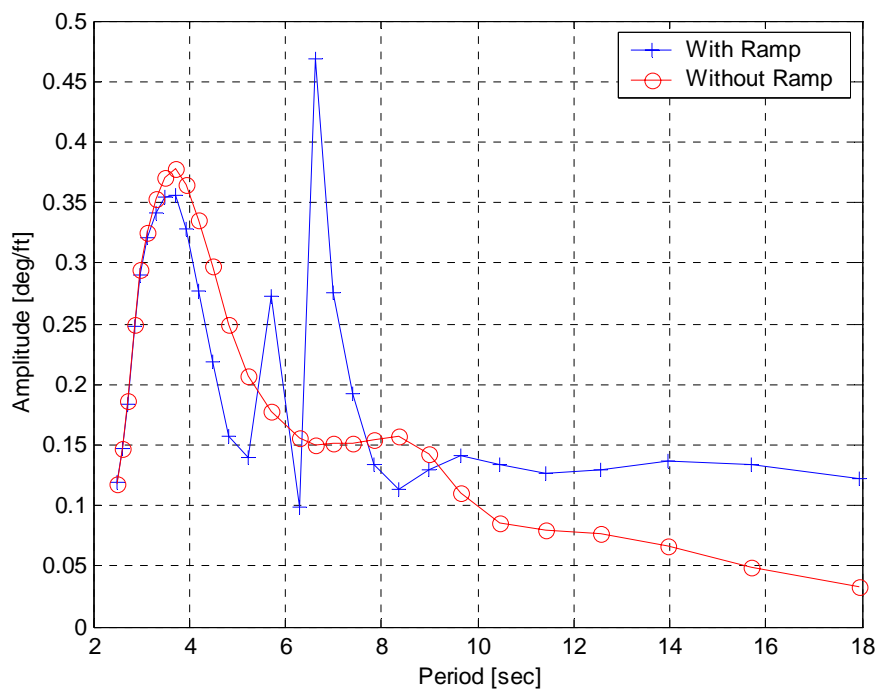


Figure B23. Effect of Ramp on Barge (RRDF) Pitch Amplitude per [ft] Wave Height, at Port Beam Seas (270 degrees).

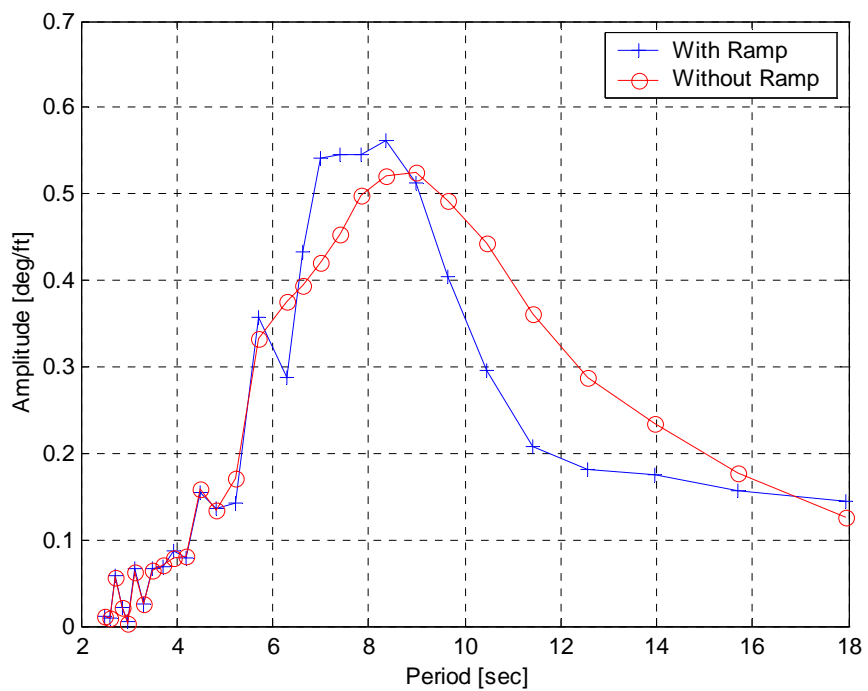


Figure B24. Effect of Ramp on Barge (RRDF) Pitch Amplitude per [ft] Wave Height, at Quartering Seas (315 degrees).

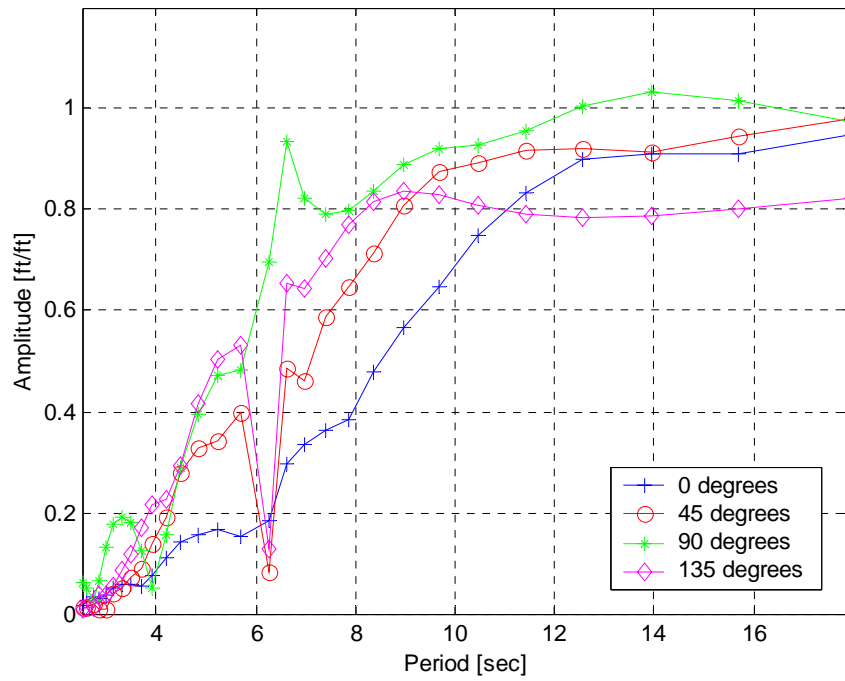


Figure B25. Heave Amplitude per [ft] Wave Height for the Barge (RRDF), with Ramp, at Variable Wave Directions.

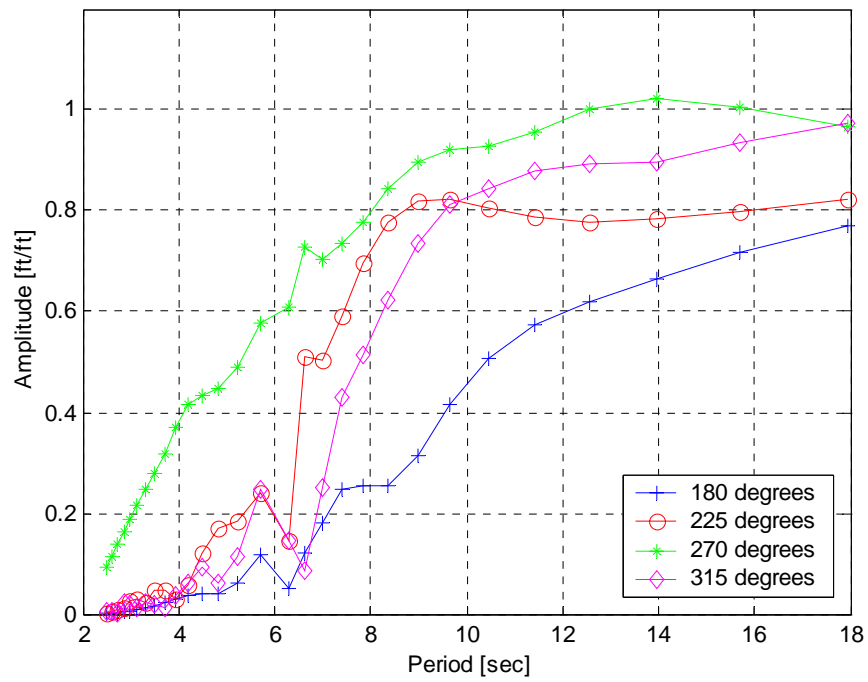


Figure B26. Heave Amplitude per [ft] Wave Height for the Barge (RRDF), with Ramp, at Variable Wave Directions.

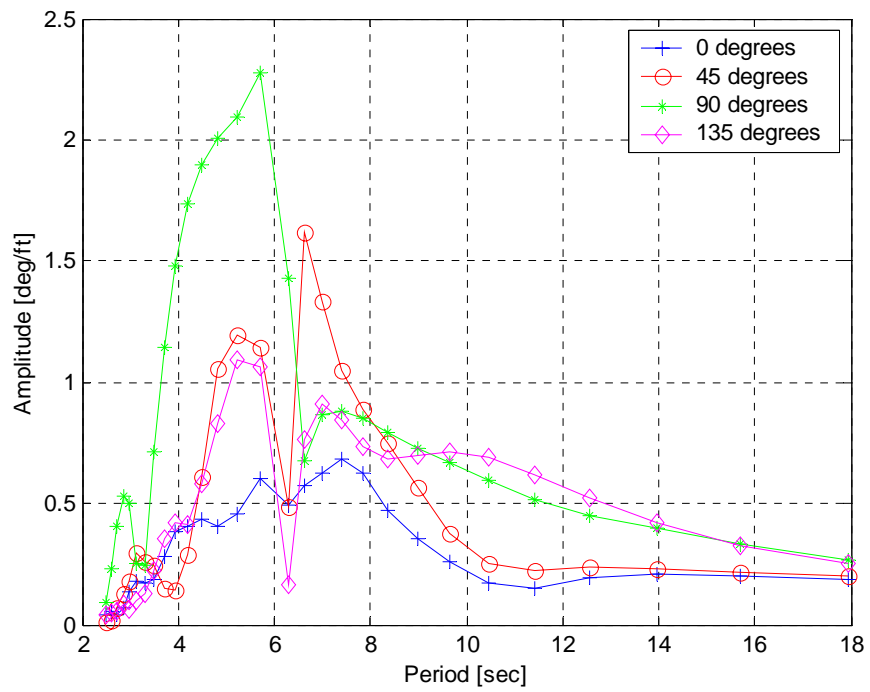


Figure B27. Roll Amplitude per [ft] Wave Height for the Barge (RRDF), with Ramp, at Variable Wave Directions

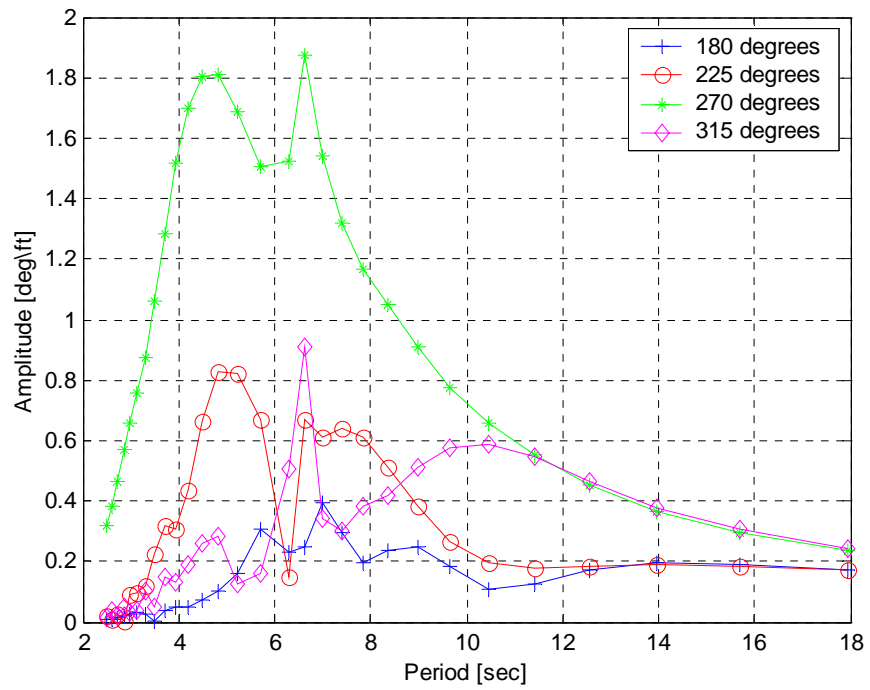


Figure B28. Roll Amplitude per [ft] Wave Height for the Barge (RRDF), with Ramp, at Variable Wave Directions .

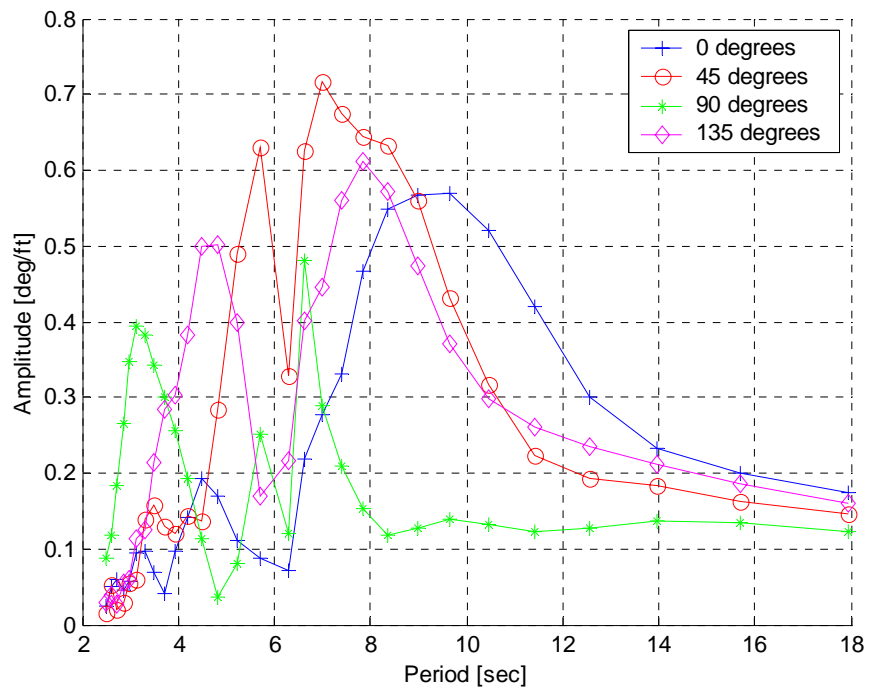


Figure B29. Pitch Amplitude per [ft] Wave Height for the Barge (RRDF), with Ramp, at Variable Wave Directions

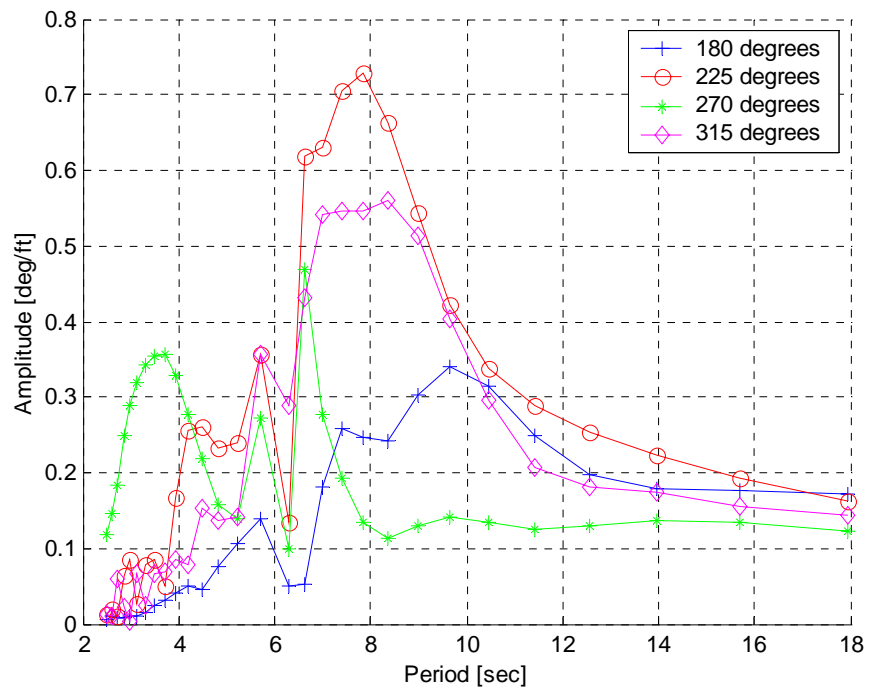


Figure B30. Pitch Amplitude per [ft] Wave Height for the Barge (RRDF), with Ramp, at Variable Wave Directions .

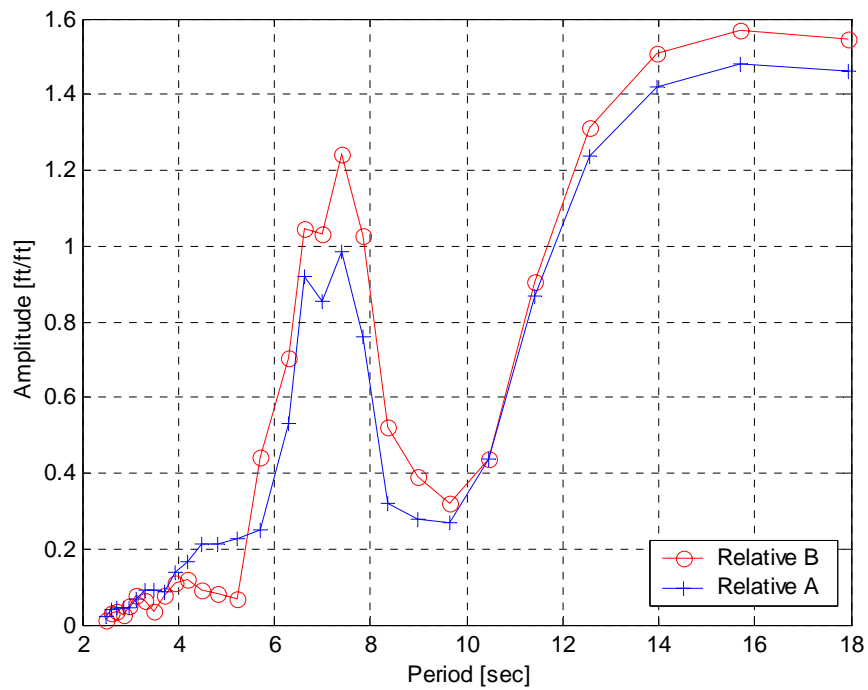


Figure B31. Amplitude per [ft] Wave Height of Relative Motion Between Ramp's and Barge Connection Points at Following Seas (0 degrees) .

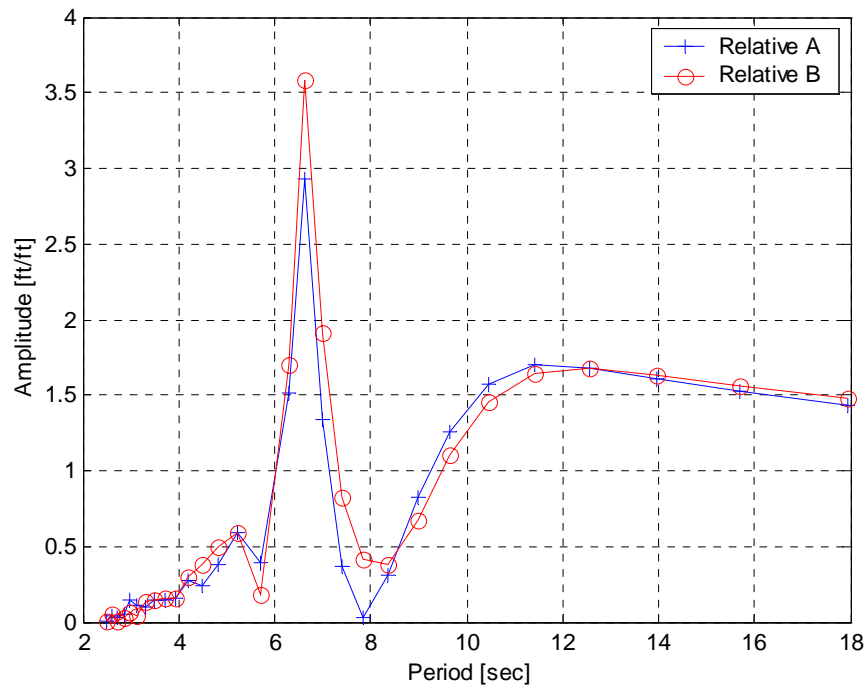


Figure B32. Amplitude per [ft] Wave Height of Relative Motion Between Ramp's and Barge Connection Points at Quartering Seas (45 degrees) .

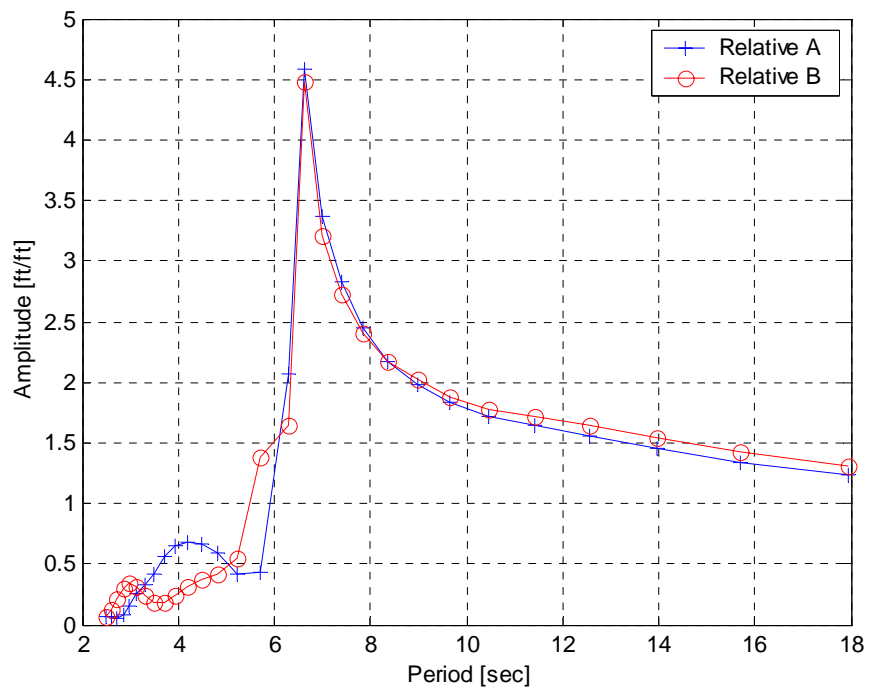


Figure B33. Amplitude per [ft] Wave Height of Relative Motion Between Ramp's and Barge Connection Points at Starboard Beam Seas (90 degrees) .

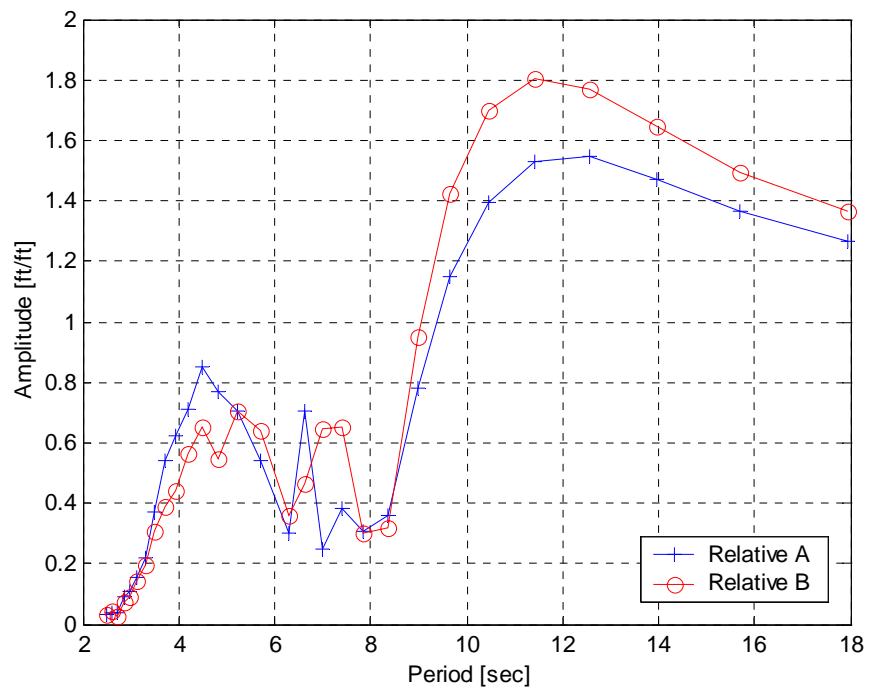


Figure B34. Amplitude per [ft] Wave Height of Relative Motion Between Ramp's and Barge Connection Points at Quartering Seas (135 degrees) .

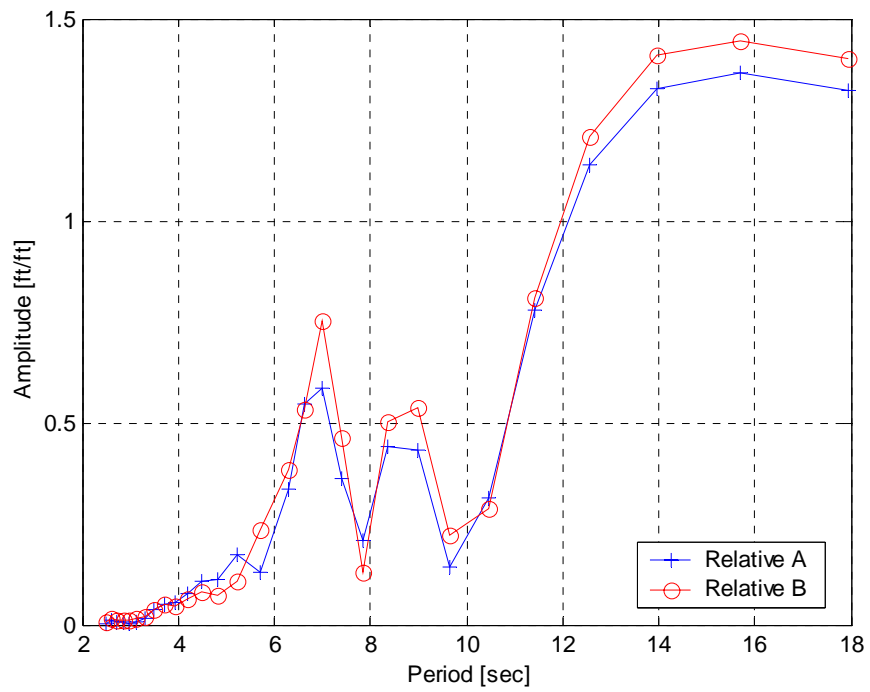


Figure B35. Amplitude per [ft] Wave Height of Relative Motion Between Ramp's and Barge Connection Points at Head Seas (180 degrees) .

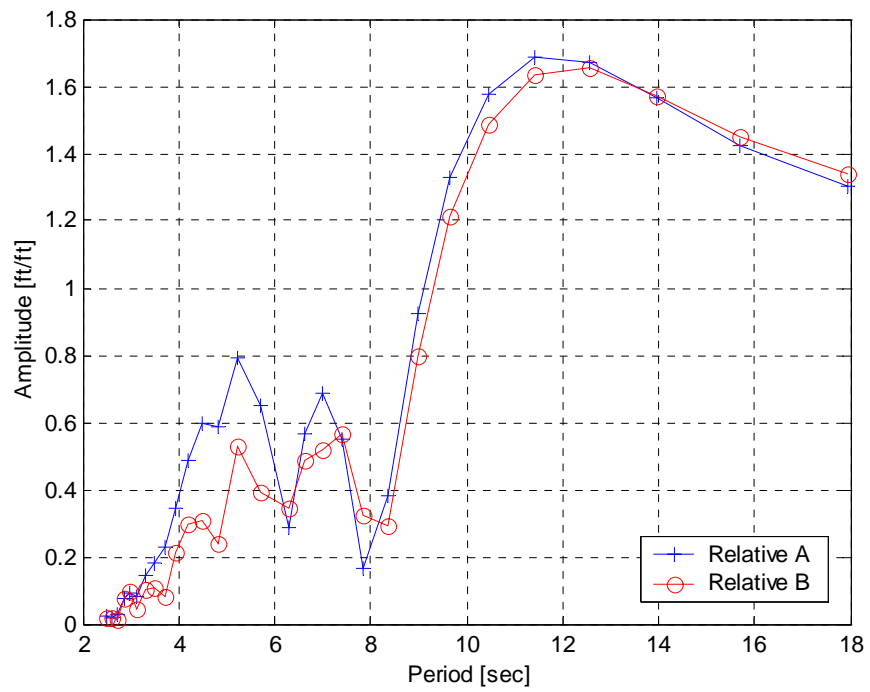


Figure B36. Amplitude per [ft] Wave Height of Relative Motion Between Ramp's and Barge Connection Points at Quartering Seas (225 degrees) .



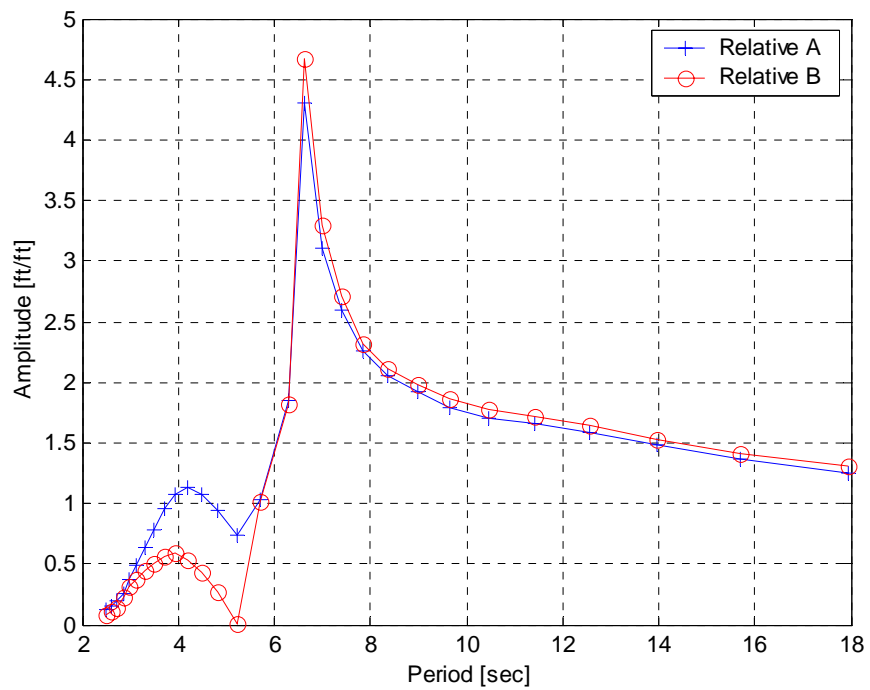


Figure B37. Amplitude per [ft] Wave Height of Relative Motion Between Ramp's and Barge Connection Points at Port Beam Seas (270 degrees) .

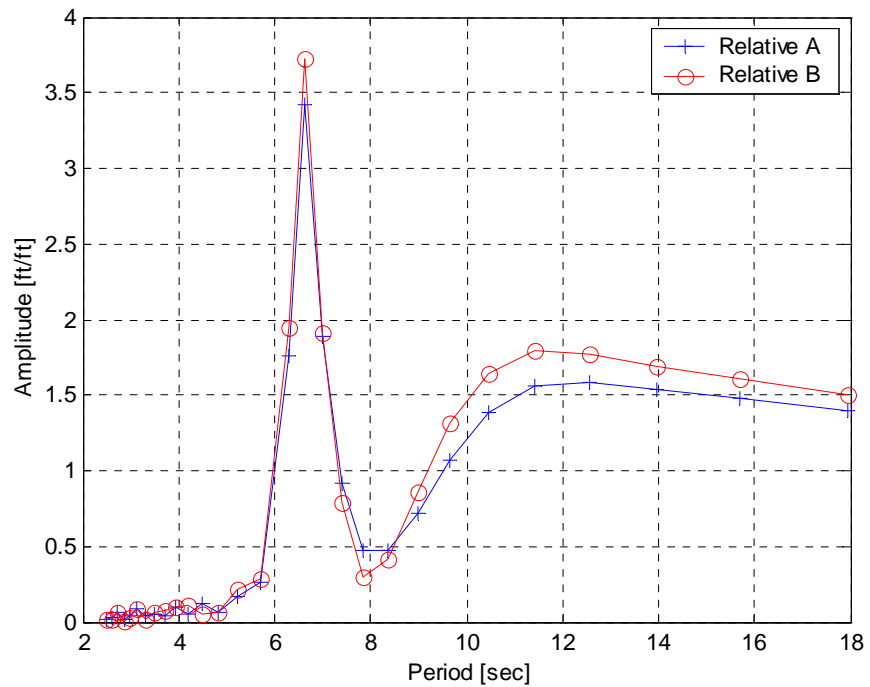


Figure B38. Amplitude per [ft] Wave Height of Relative Motion Between Ramp's and Barge Connection Points at Quartering Seas (315 degrees), .

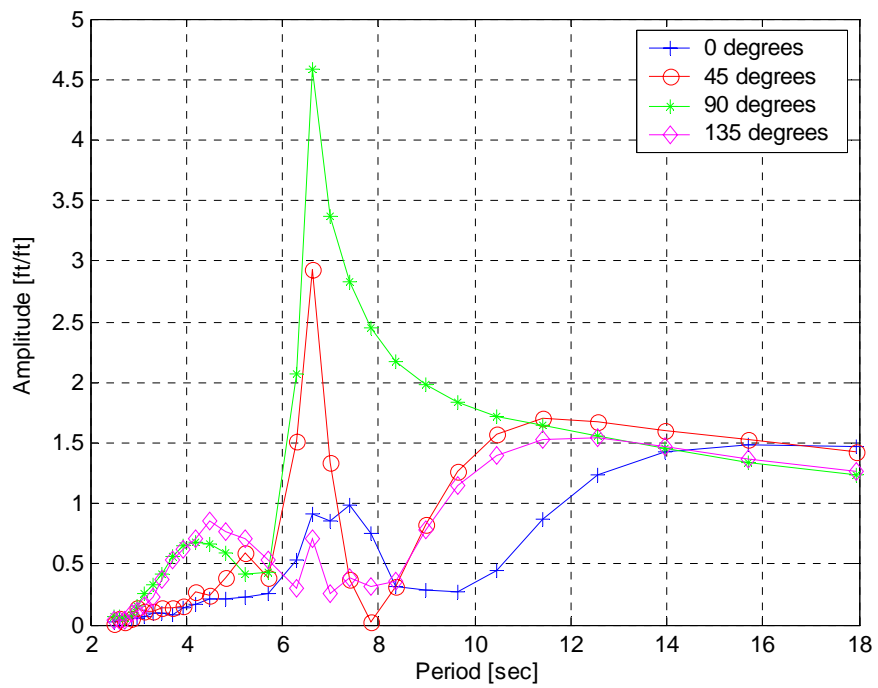


Figure B39. Amplitude per [ft] Wave Height, of Relative Motion Between Ramp's and Barge Connection Point A, for Various Headings. .

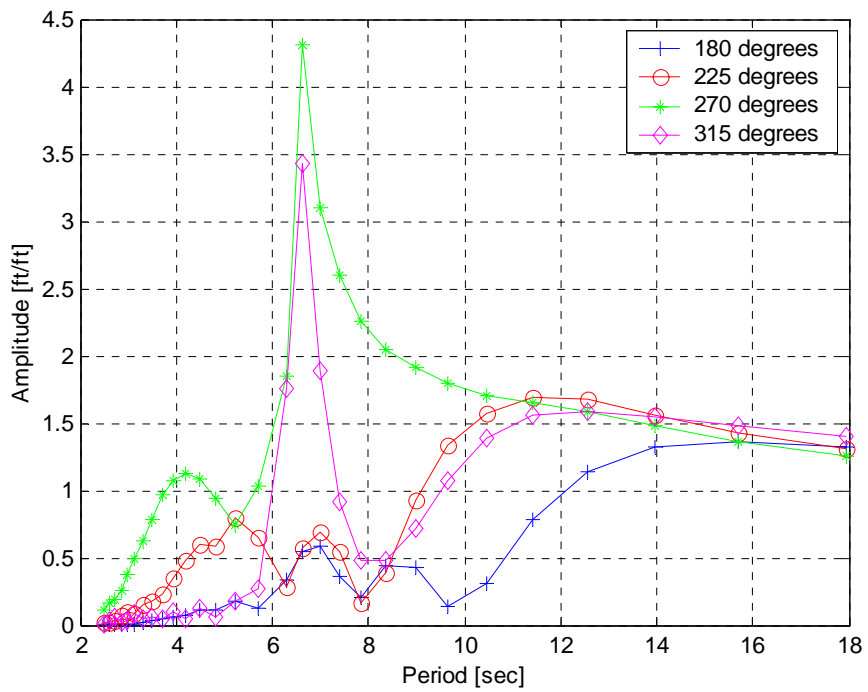


Figure B40. Amplitude per [ft] Wave Height, of Relative Motion Between Ramp's and Barge Connection Point A, for Various Headings. .

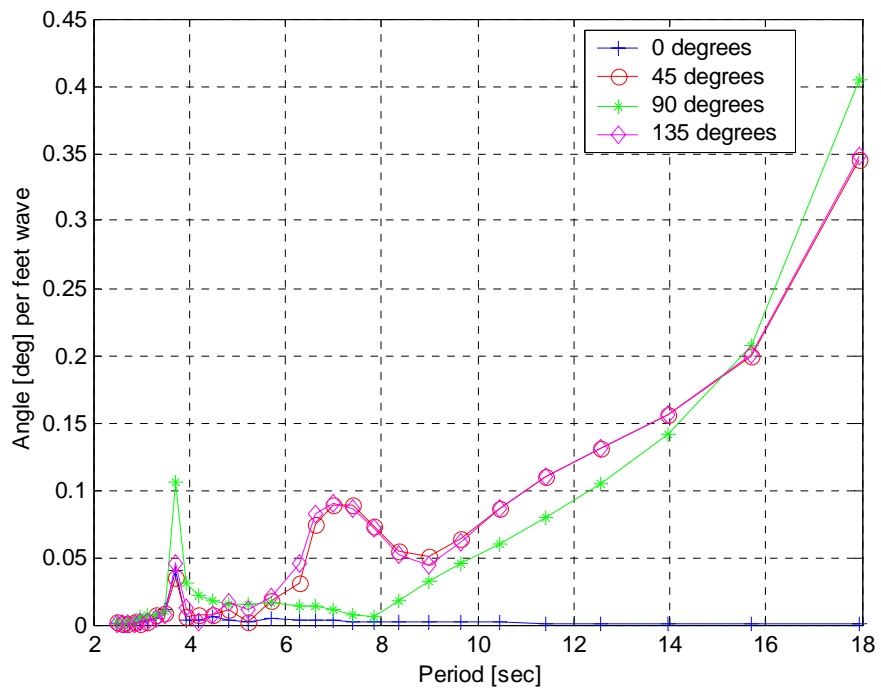


Figure B41. Twist Angle per [ft] Wave Height of Ramp at Various Headings .

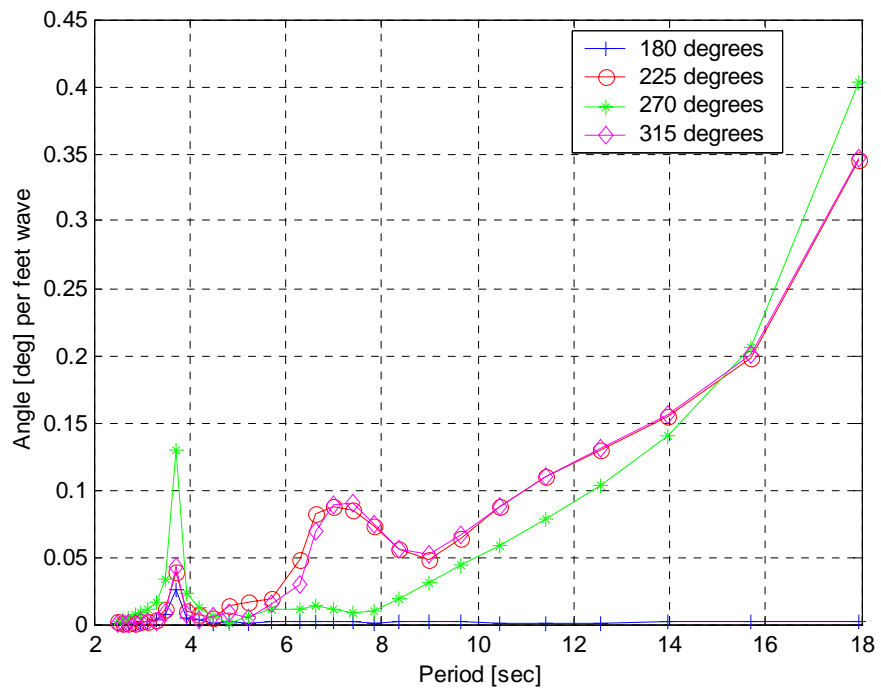


Figure B42. Twist Angle per [ft] Wave Height of Ramp at Various Headings .

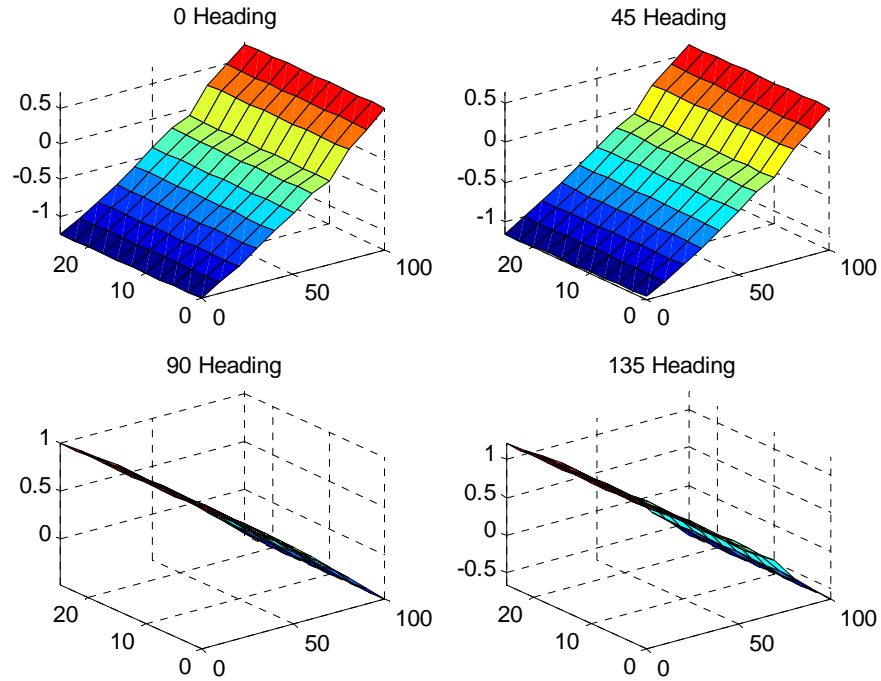


Figure B43. Displacement Amplitude per [ft] Wave Height of the Ramp at Wave Period 18 sec (0.35 Hz) and at Various Headings .

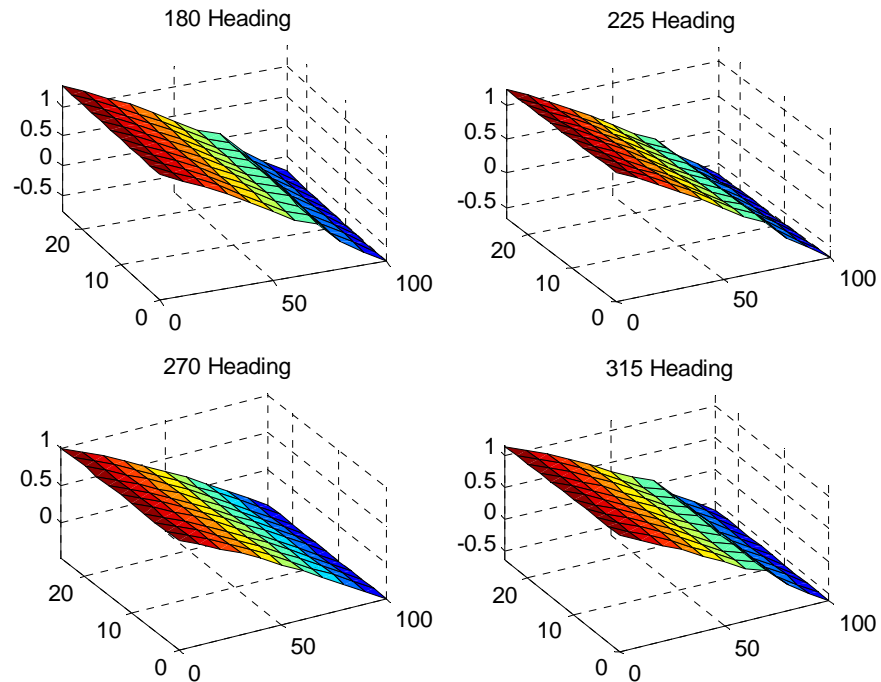


Figure B44. Displacement Amplitude per [ft] Wave Height of the Ramp at Wave Period 18 sec (0.35 Hz) and at Various Headings .

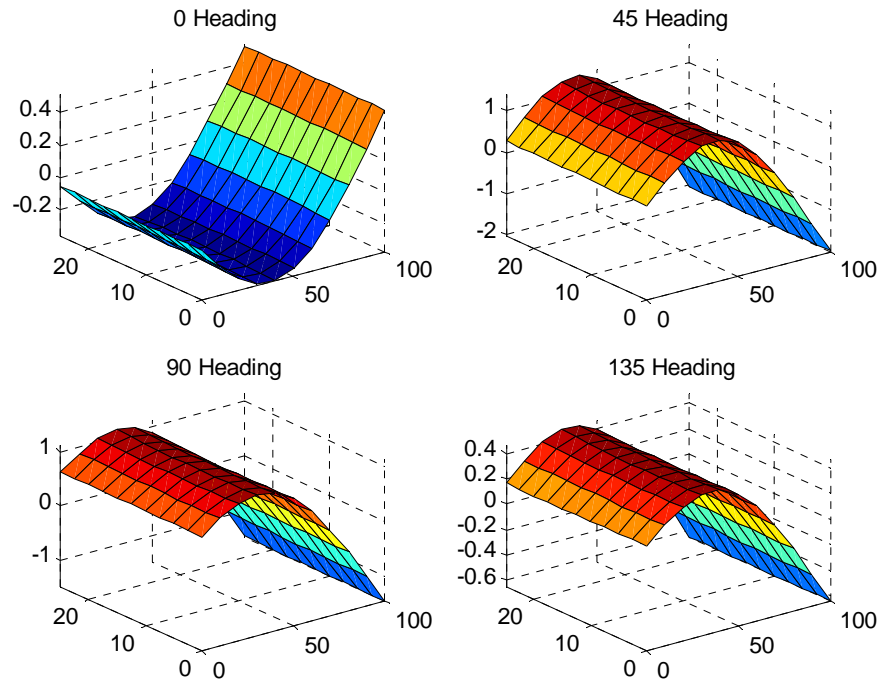


Figure B45. Displacement Amplitude per [ft] Wave Height of the Ramp at Wave Period 6.28 sec (1 Hz) and at Various Headings .

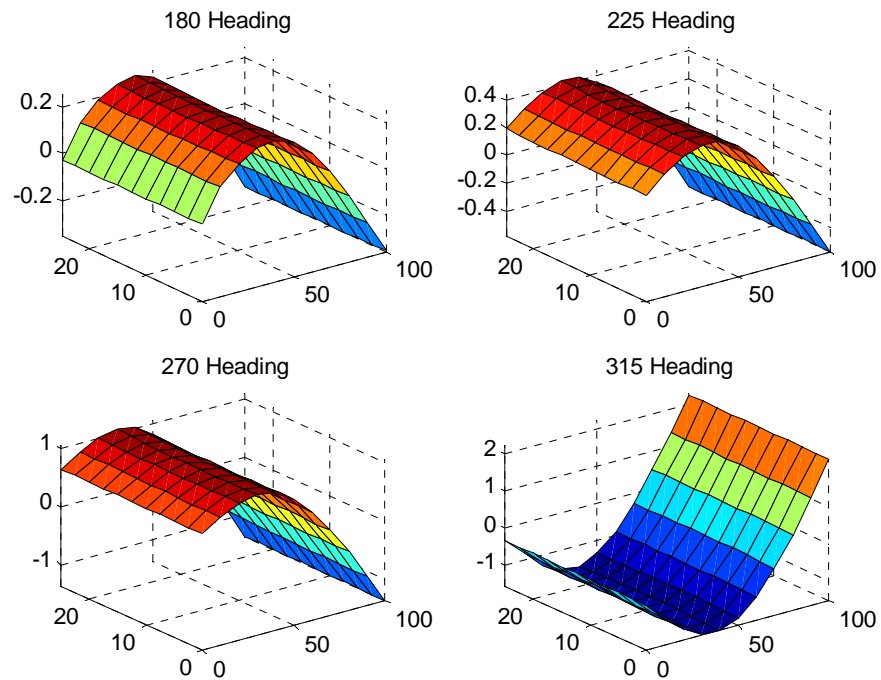


Figure B46. Displacement Amplitude per [ft] Wave Height of the Ramp at Wave Period 6.28 sec (1 Hz) and at Various Headings .

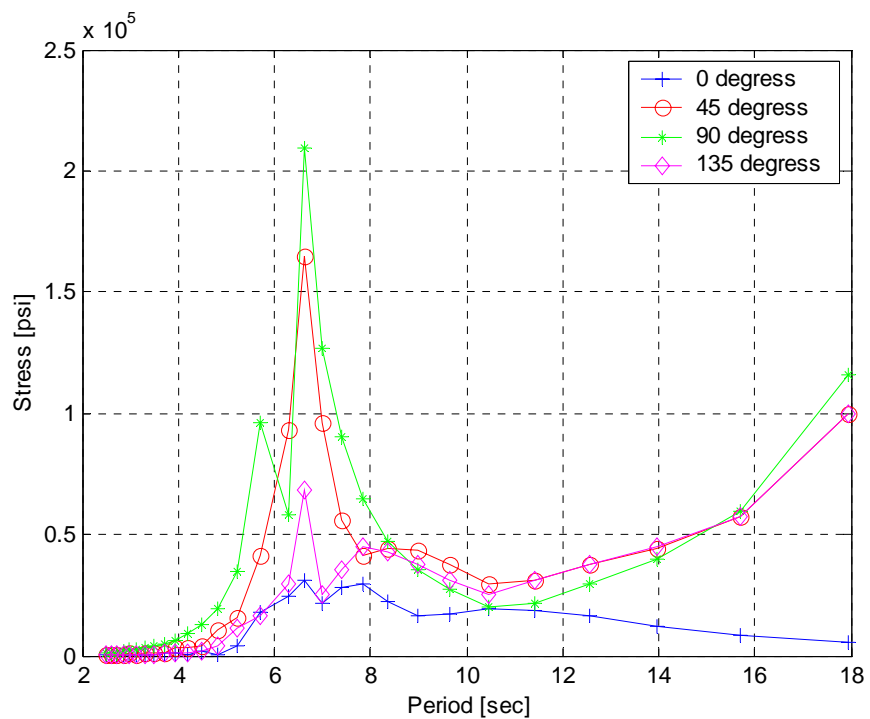


Figure B47. Ramp Maximum Stress Amplitude per [ft] Wave Height for Various Headings .

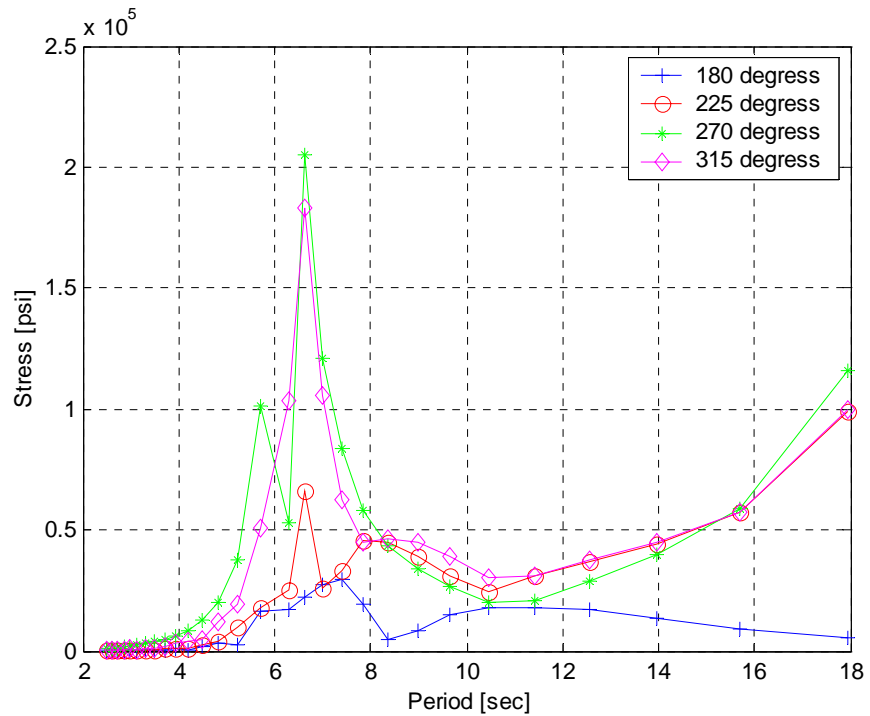


Figure B48. Ramp Maximum Stress Amplitude per [ft] Wave Height for Various Headings .

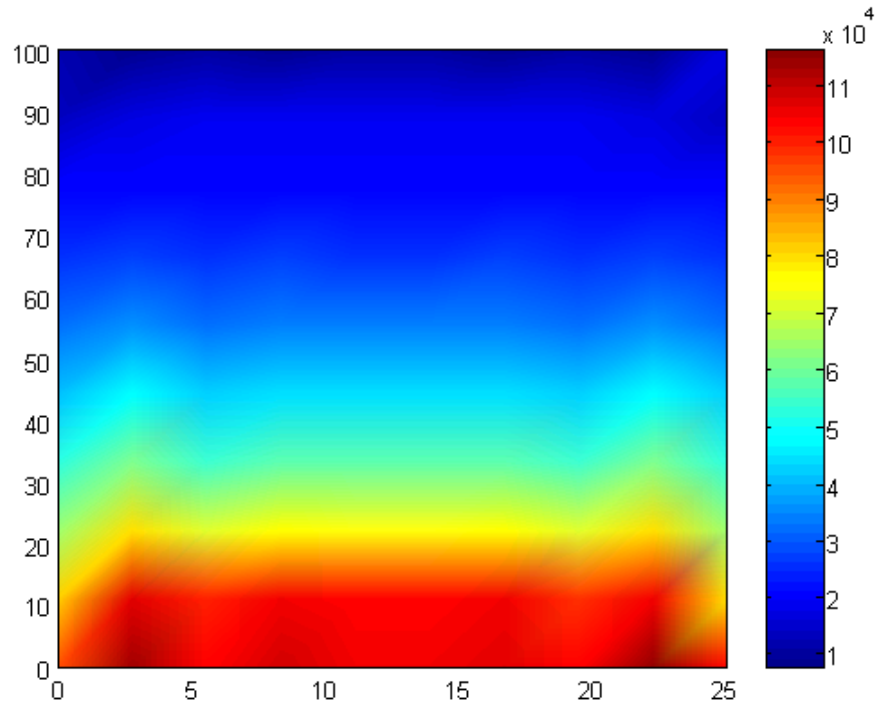


Figure B49. Ramp Stress Amplitude per [ft] Wave Height at Wave Period 18 sec (0.35 Hz) and 90 degrees Heading (k, c values as Figure B43).

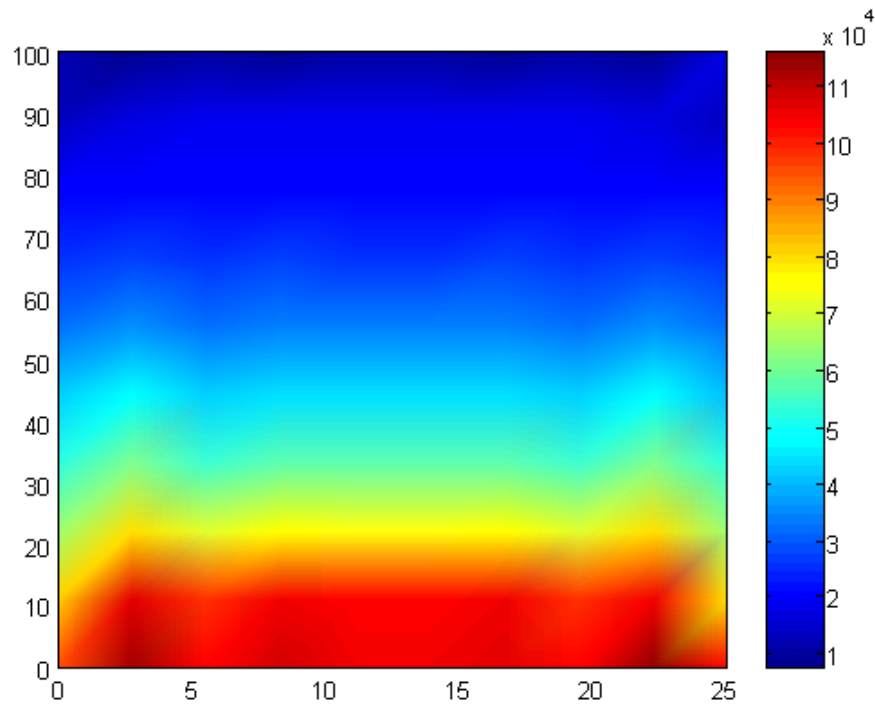


Figure B50. Ramp Stress Amplitude per [ft] Wave Height at Wave Period 18 sec (0.35 rad/sec) and 270 degrees Heading (k, c values as Figure B44).

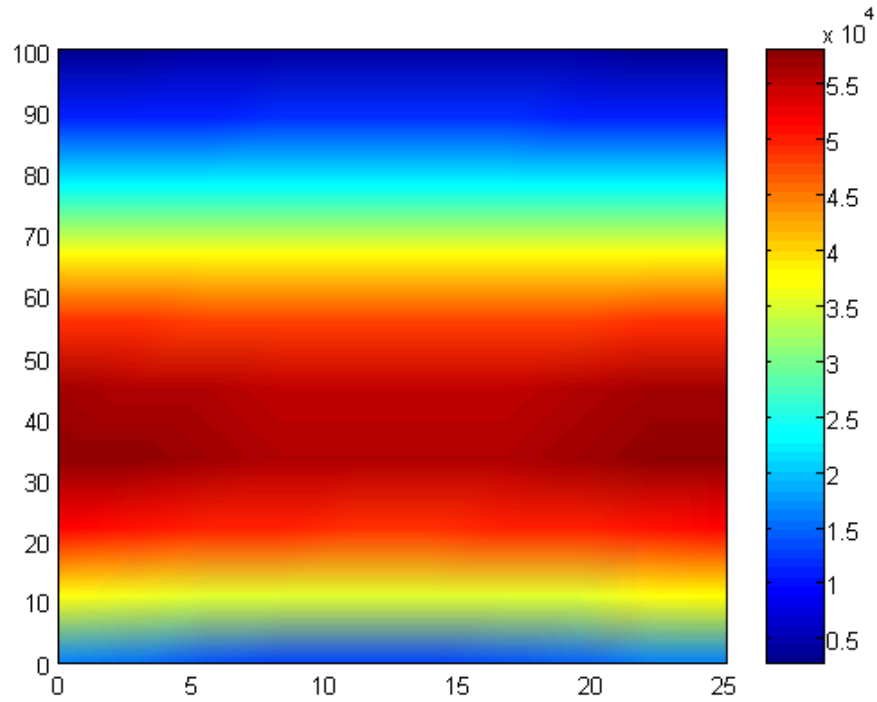


Figure B51. Ramp Stress Amplitude per [ft] Wave Height at Wave Period 6.28 sec (1 rad/sec) and 90 degrees Heading (k, c values as Figure B45).

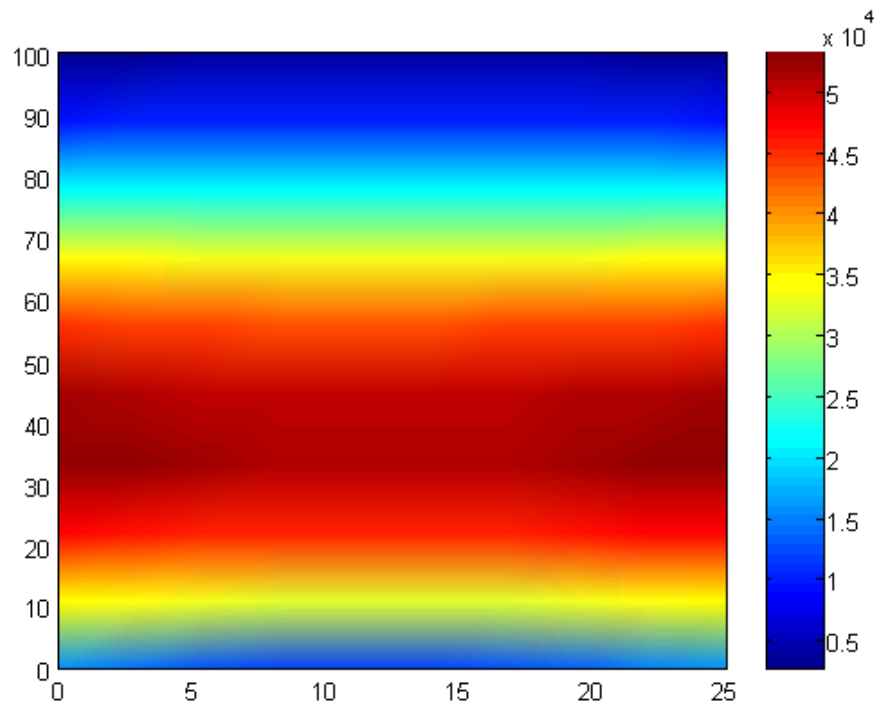


Figure B52. Ramp Stress Amplitude per [ft] Wave Height at Wave Period 6.28 sec (1 rad/sec) and 270 degrees Heading (k, c values as Figure B46).



THIS PAGE INTENTIONALLY LEFT BLANK

## APPENDIX C

This Appendix contains the following figures:

- Figure C1: Pierson – Moskowitz Spectrum.
- Figures C2 through C13: Spectrum of the relative motion response at connection point A for all cases of spring/damper values under consideration, and for different headings.
- Figures C14 through C20: RMS value of the relative motion of ramp and barge at connection point A for all cases of spring/damper values considered. Both rectangular and polar plots are presented .
- Figures C21 through C27: RMS value of the ramp twist for all cases of spring/damper values considered and vertical motions at the Ramp/RRDF connection points. Both rectangular and polar plots are presented here.
- Figures C28 through C34: RMS value of the ramp maximum stress for all cases of spring/damper values considered and vertical motions at the Ramp/RRDF connection points. Both rectangular and polar plots are presented here.
- Figures C35 through C36: RMS value of the vertical motion of the barge connection point A and B for all cases of spring/damper values considered.

Discussion of these figures is presented in Chapter V, Section D.

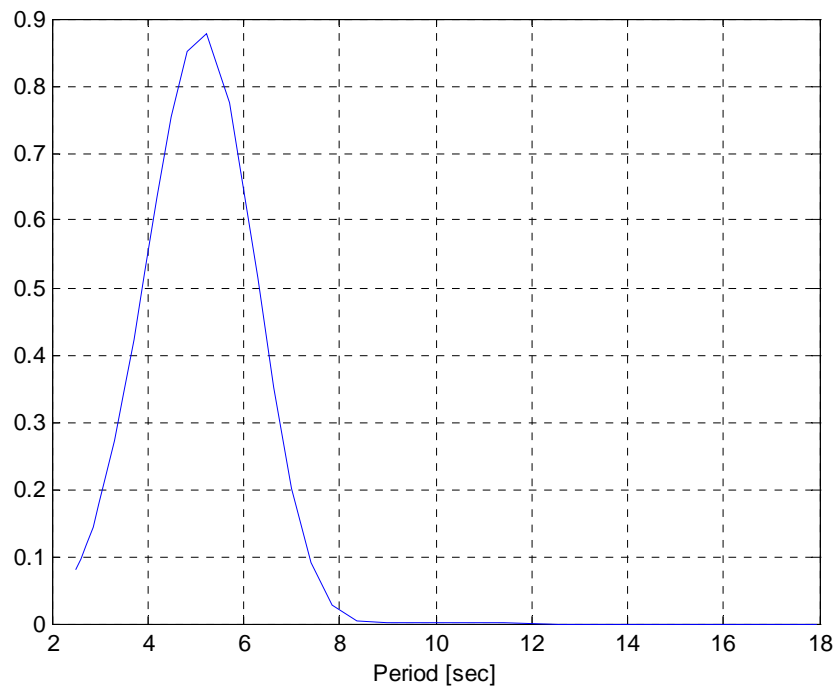


Figure C1. Pierson – Moskowitz Spectrum

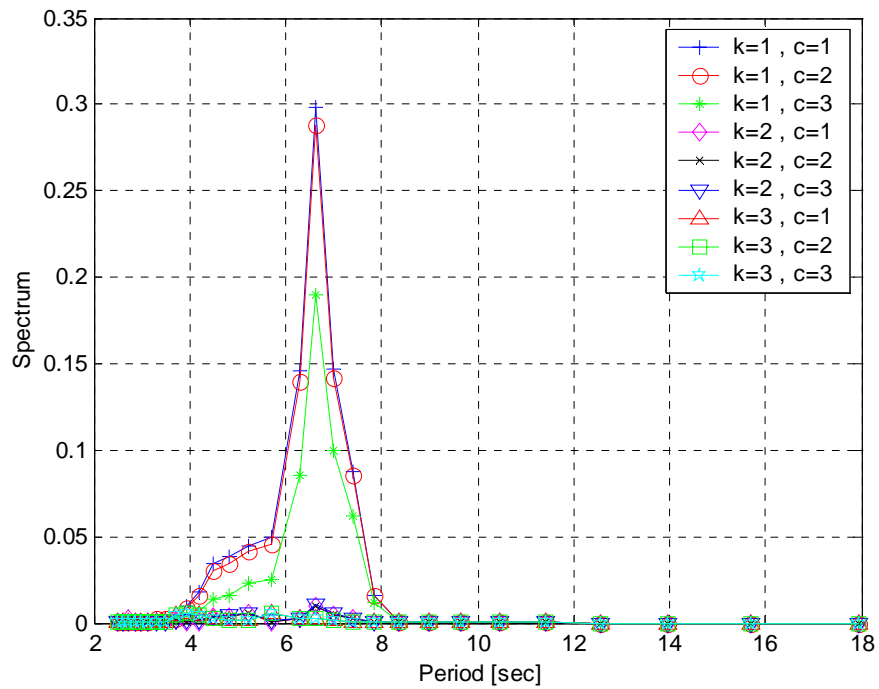


Figure C2. Spectrum of the Relative Motion Response at Connection Point A at Following Seas (0 Degrees) for all Cases Under Consideration.

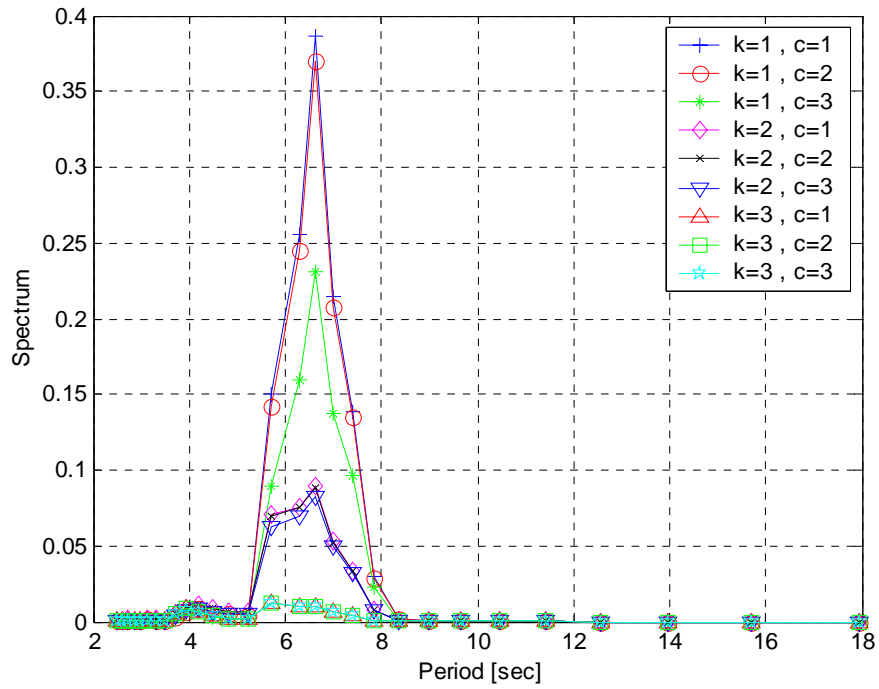


Figure C3. Spectrum of the Relative Motion Response at Connection Point B at Following Seas (0 degrees) for all Cases Under Consideration.

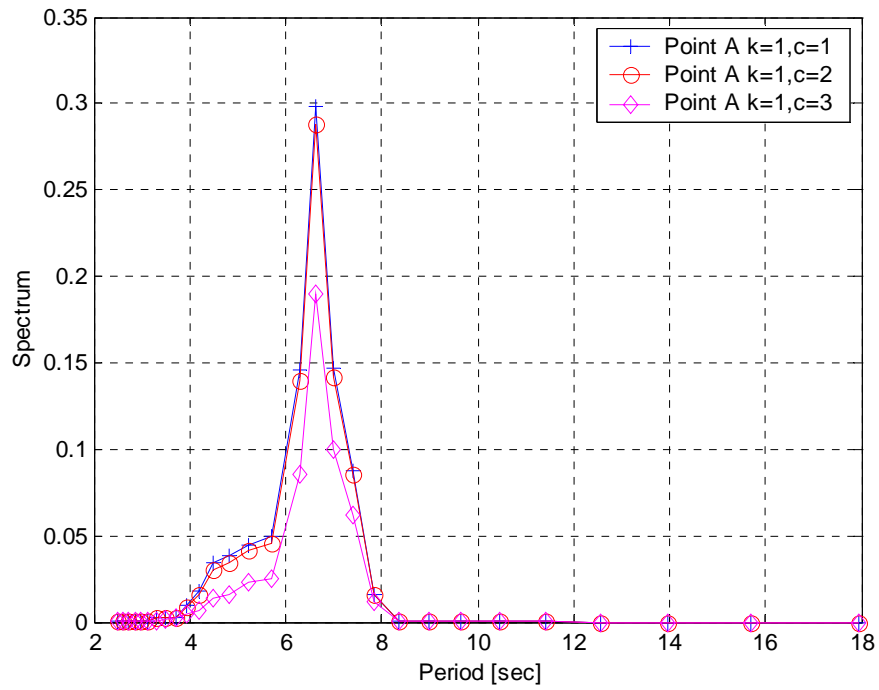


Figure C4. Spectrum of the Relative Motion Response at Connection Point A at Following Seas (0 degrees), (holding  $k$  constant and varying  $c$ ).

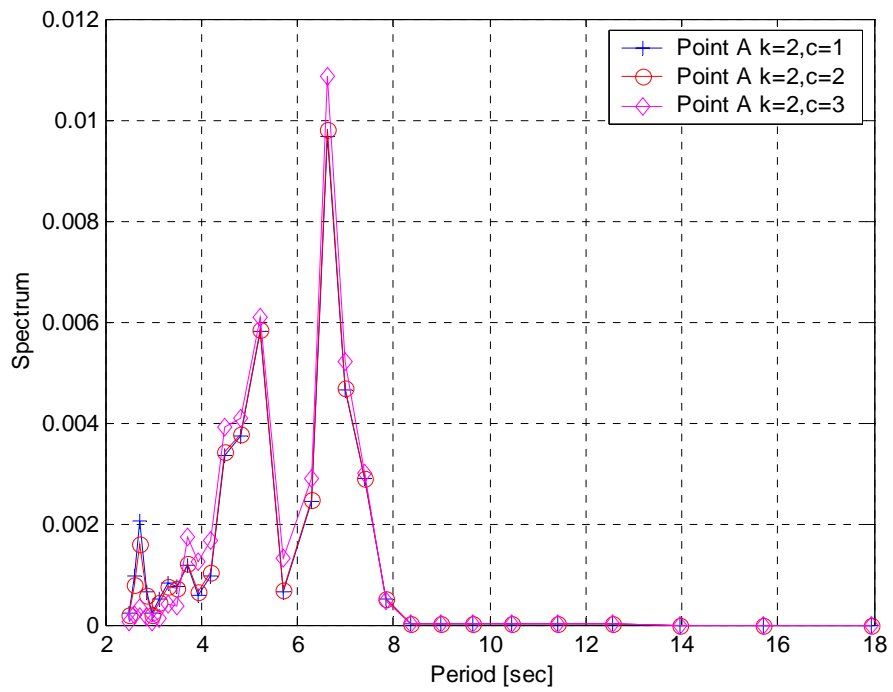


Figure C5. Spectrum of the Relative Motion Response at Connection Point A at Following Seas (0 degrees), (holding  $k$  constant and varying  $c$ ).

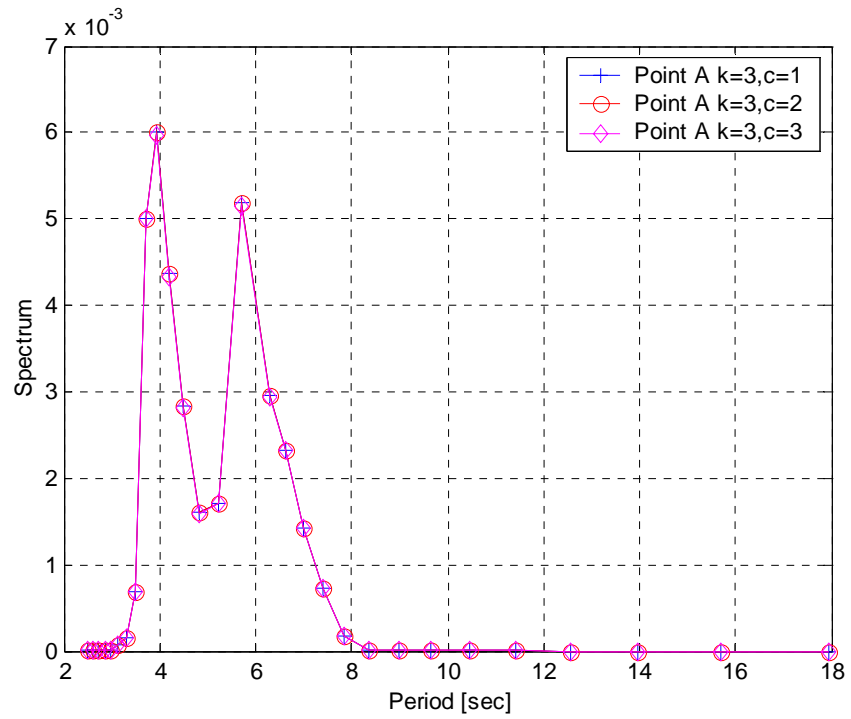


Figure C6. Spectrum of the Relative Motion Response at Connection Point A at Following Seas (0 degrees), (holding  $k$  constant and varying  $c$ ).

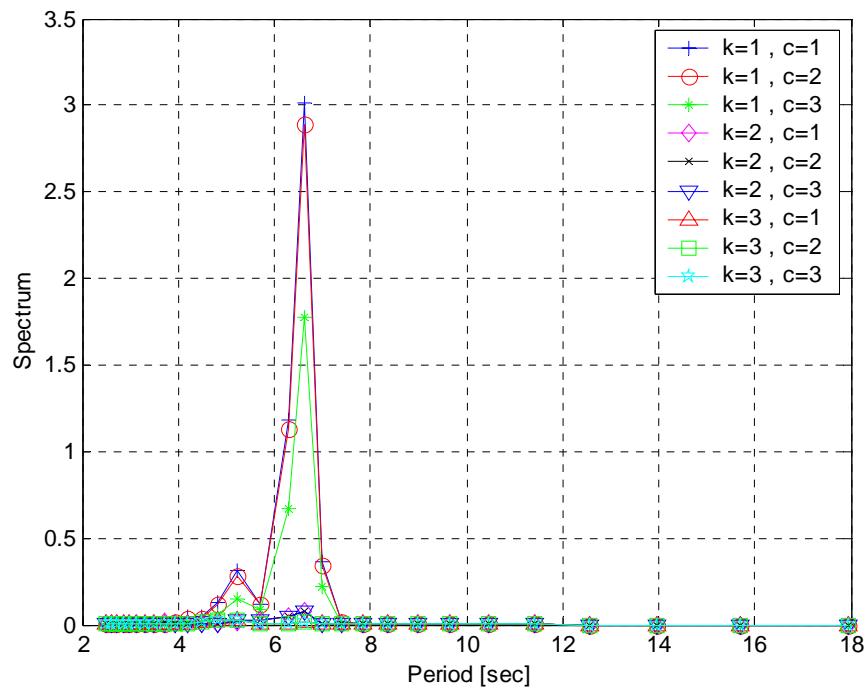


Figure C7. Spectrum of the Relative Motion Response at Connection Point A at Quartering Seas (45 degrees) for all Cases Considered.

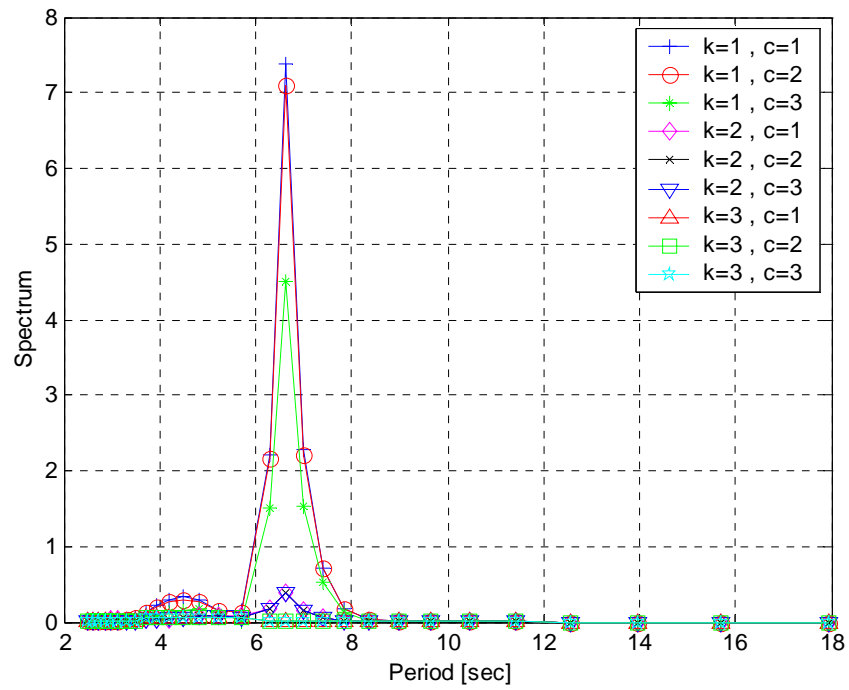


Figure C8. Spectrum of the Relative Motion Response at Connection Point A at Starboard Beam Seas (90 degrees) for all Cases Considered.

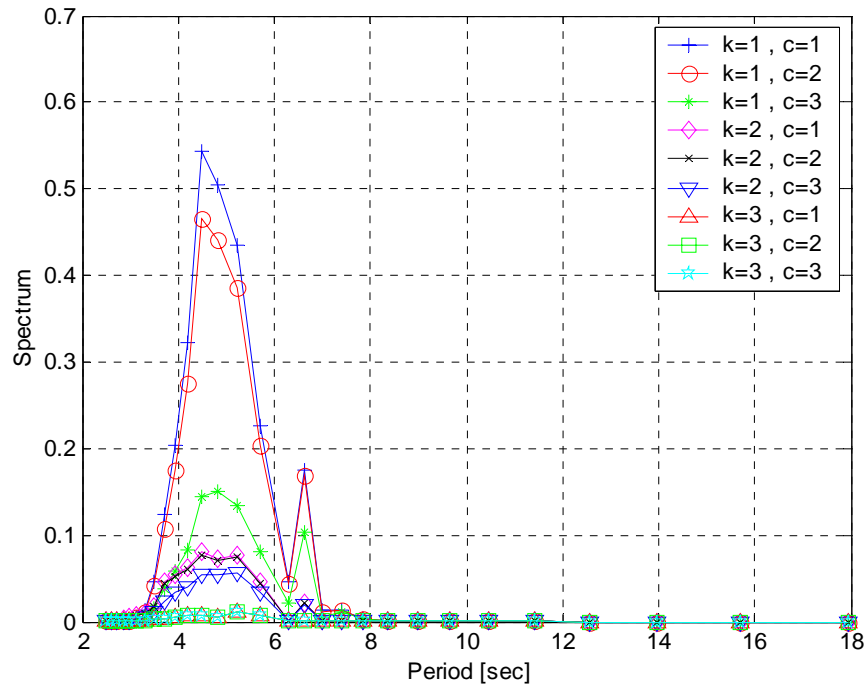


Figure C9. Spectrum of the Relative Motion Response at Connection Point A at Quivering Seas (135 degrees) for all Cases Considered.

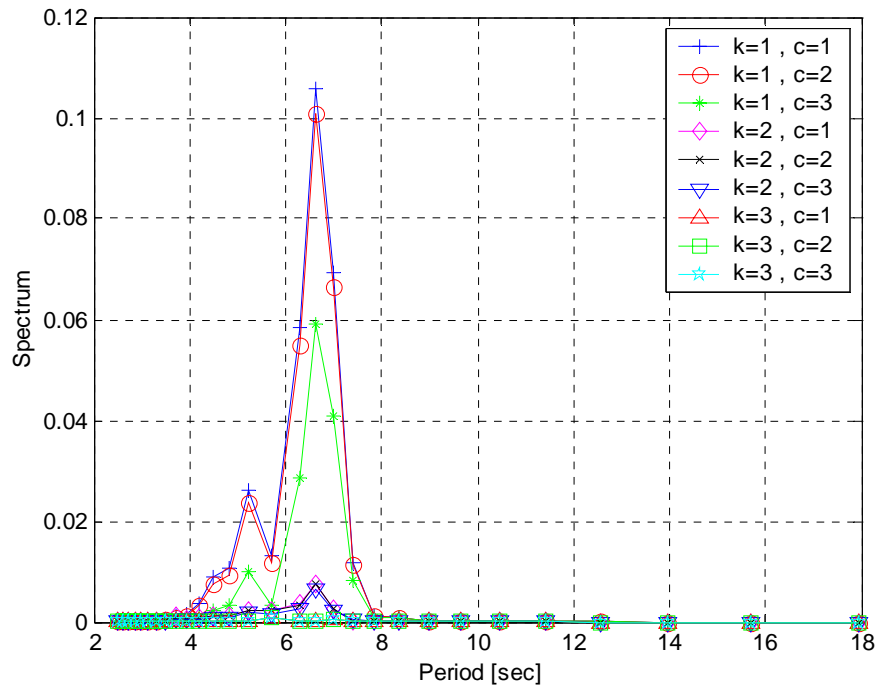


Figure C10. Spectrum of the Relative Motion Response at Connection Point A at Head Seas (180 degrees) for all Cases Considered.

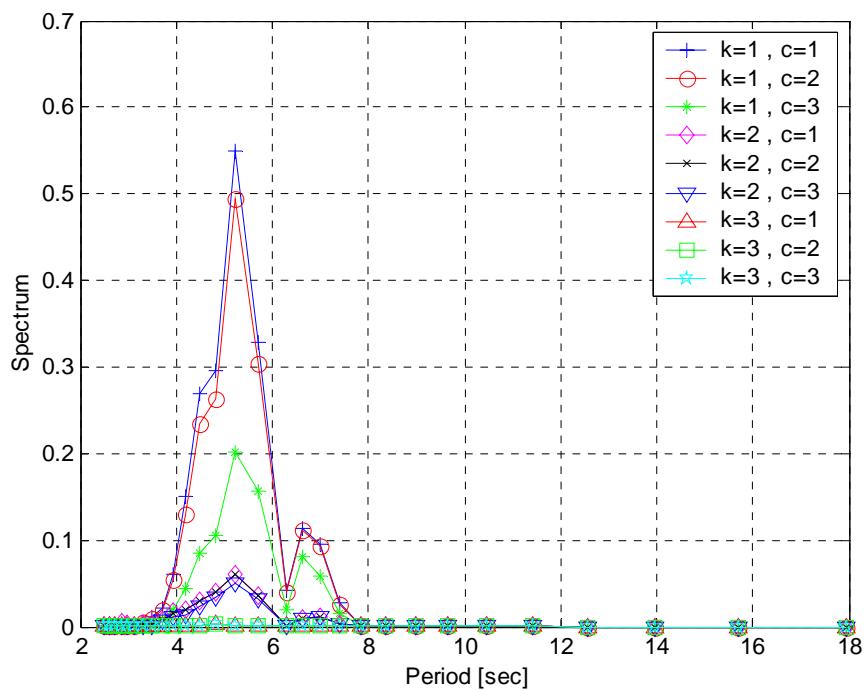


Figure C11. Spectrum of the Relative Motion Response at Connection Point A at Quatering Seas (225 degrees) for all Cases Considered.

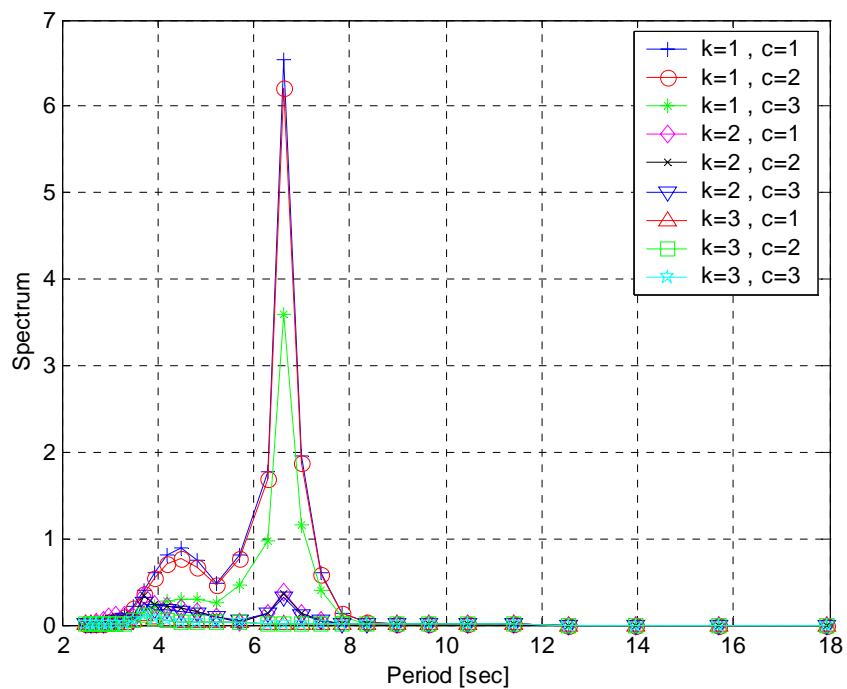


Figure C12. Spectrum of the Relative Motion Response at Connection Point A at Port Beam Seas (270 degrees) for all Cases Considered.



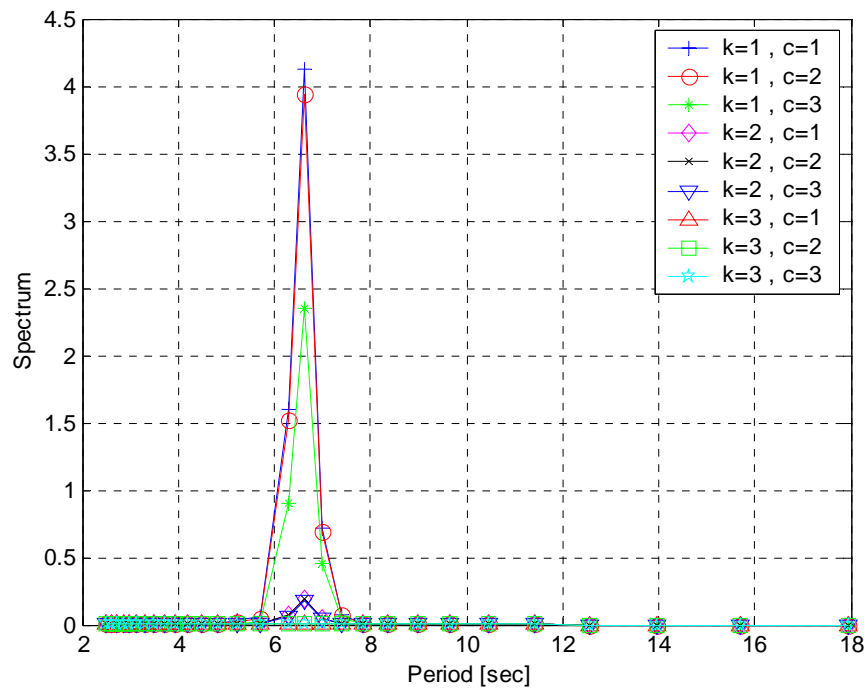


Figure C13. Spectrum of the Relative Motion Response at Connection Point A at Quatering Seas (315 degrees) for all Cases Considered.

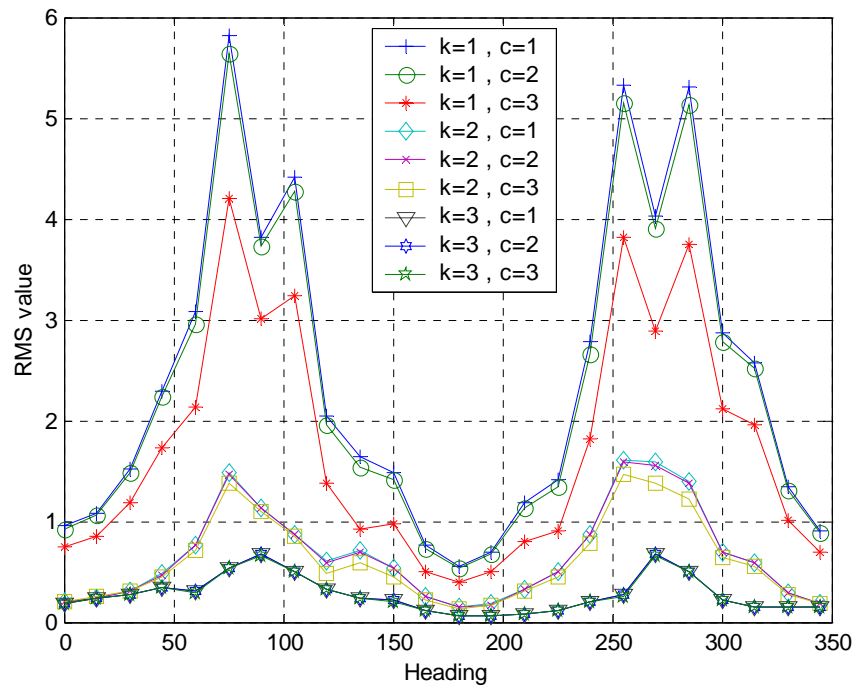


Figure C14. RMS Value of the Relative Motion of Ramp and Barge at Connection Point A for all Cases Considered

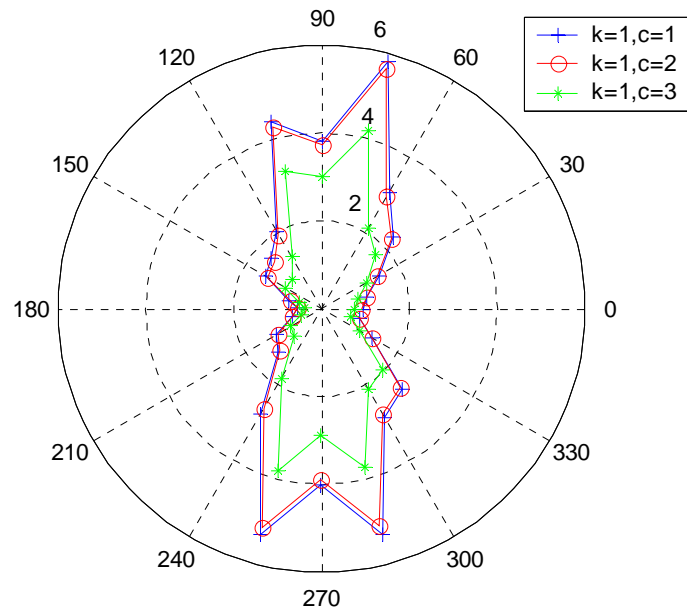


Figure C15. Polar Plot of the RMS Value of the Relative Motion of Ramp and Barge at Connection Point A (holding  $k$  constant and varying  $c$ ).

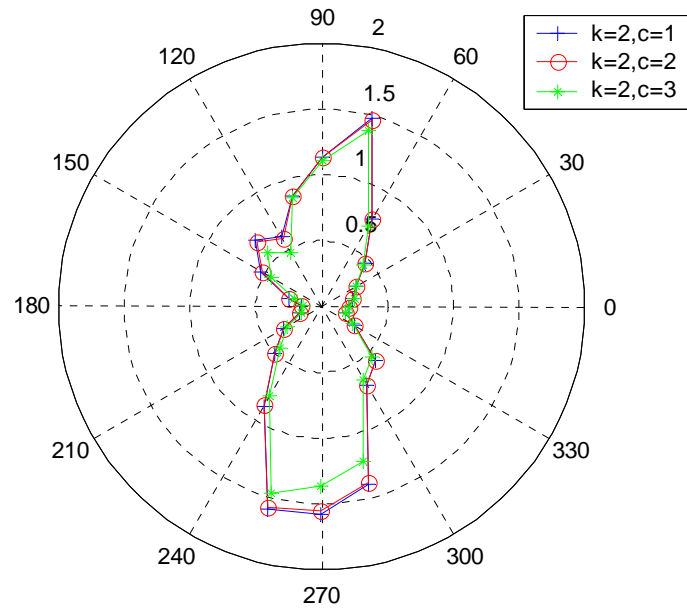


Figure C16. Polar Plot of the RMS Value of the Relative Motion of Ramp and Barge at Connection Point A (holding  $k$  constant and varying  $c$ ).

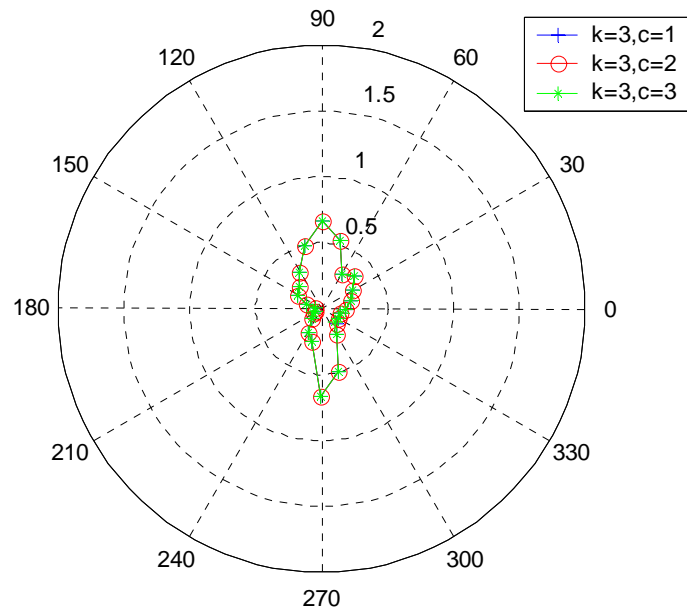


Figure C17. Polar Plot of the RMS Value of the Relative Motion of Ramp and Barge at Connection Point A (holding  $k$  constant and varying  $c$ ).

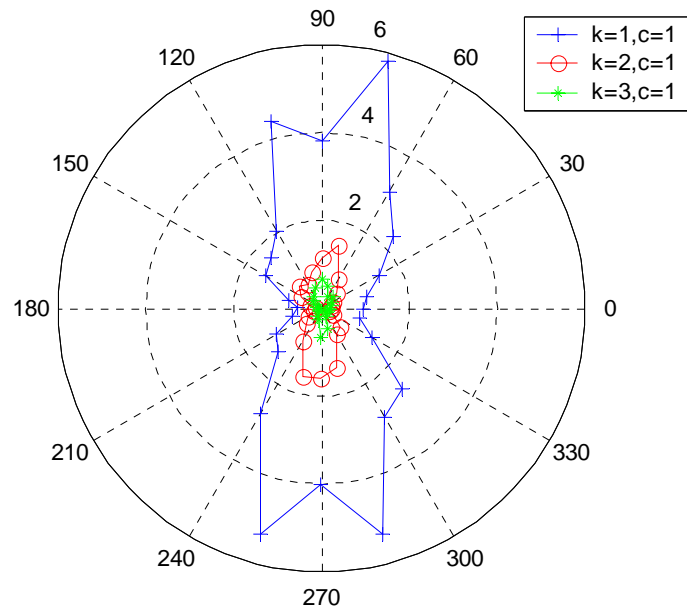


Figure C18. Polar Plot of the RMS Value of the Relative Motion of Ramp and Barge at Connection Point A (holding  $c$  constant and varying  $k$ ).

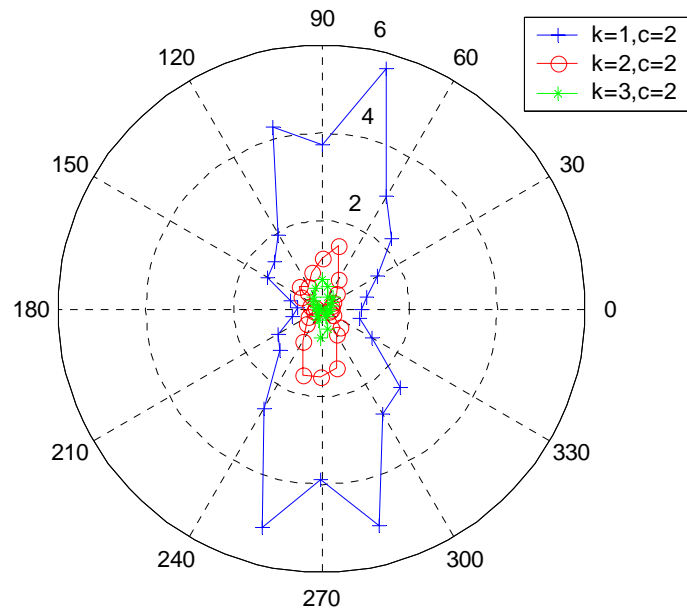


Figure C19. Polar Plot of the RMS Value of the Relative Motion of Ramp and Barge at Connection Point A (holding  $c$  constant and varying  $k$ ).

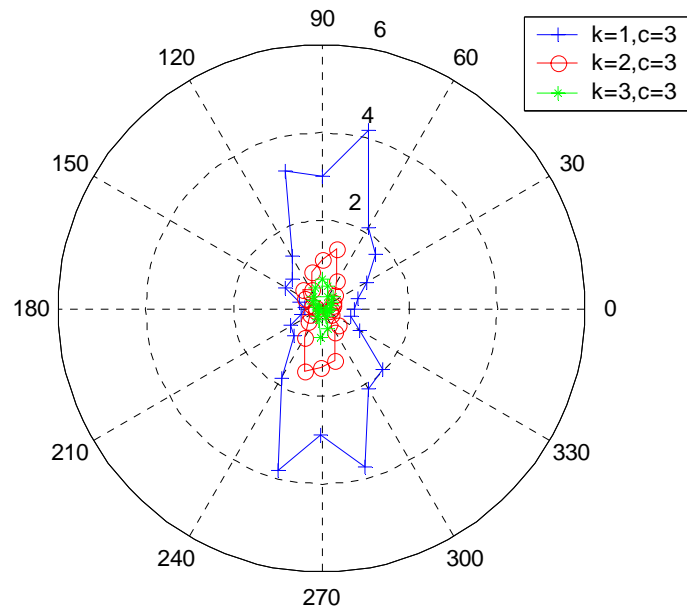


Figure C20. Polar Plot of the RMS Value of the Relative Motion of Ramp and Barge at Connection Point A (holding  $c$  constant and varying  $k$ ).

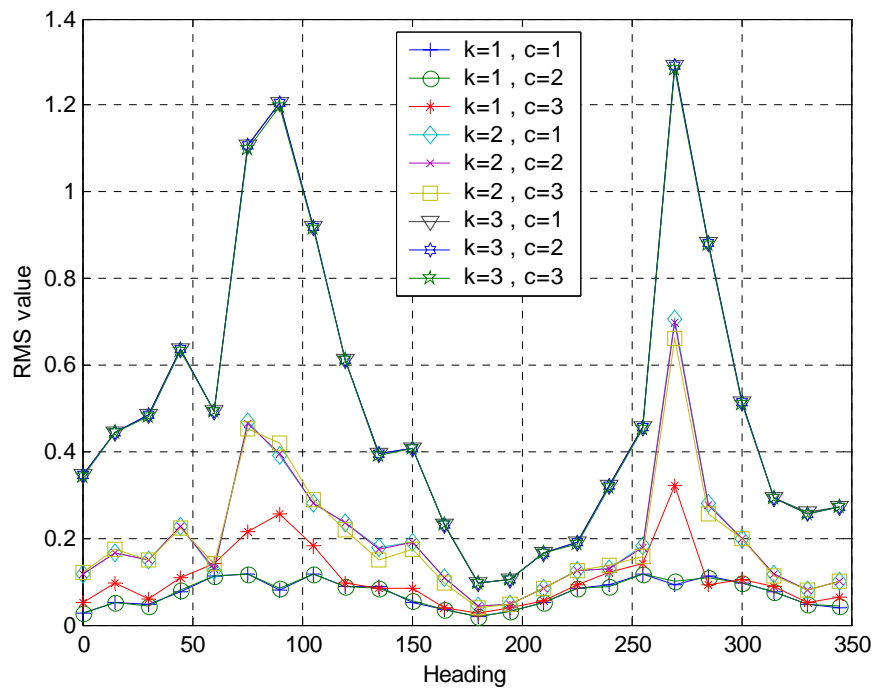


Figure C21. RMS Value of the Ramp Twist for all Cases Considered

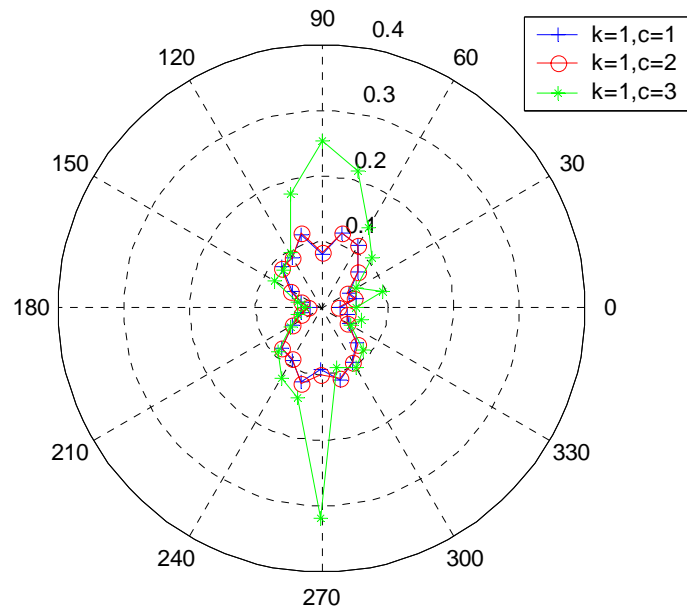


Figure C22. Polar Plot of the RMS Value of the Ramp Twist, (holding  $k$  constant and varying  $c$ ).

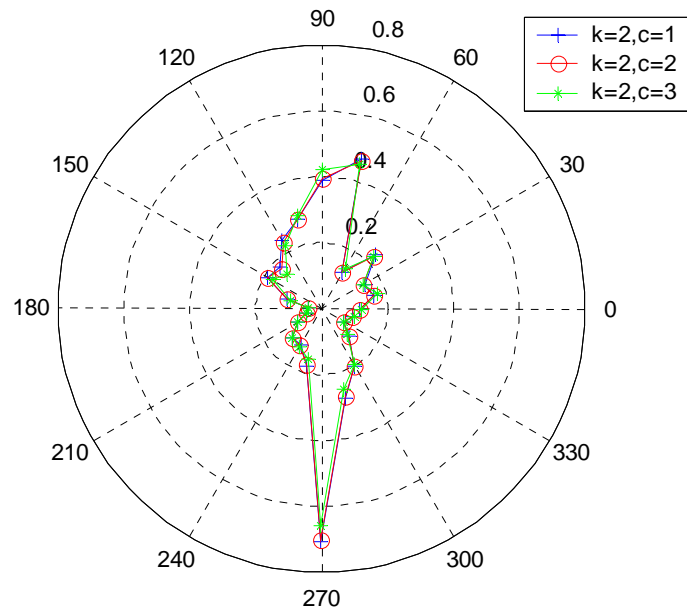


Figure C23. Polar Plot of the RMS Value of the Ramp Twist, (holding  $k$  constant and varying  $c$ ).

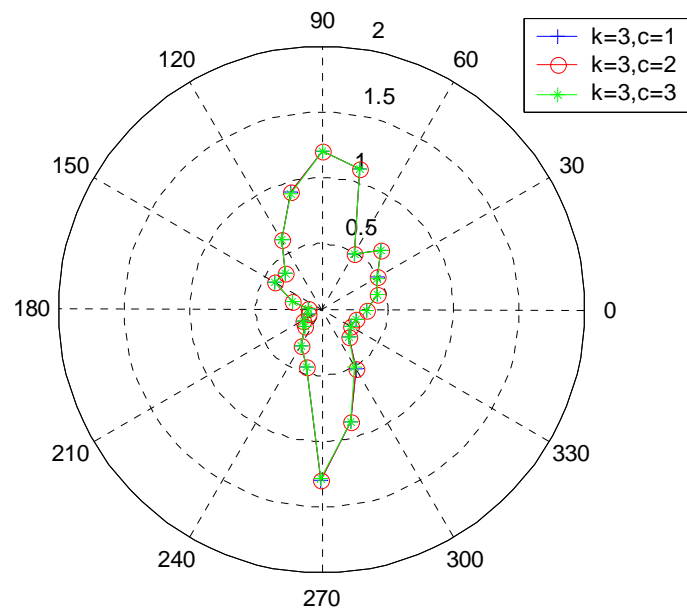


Figure C24. Polar Plot of the RMS Value of the Ramp Twist, (holding  $k$  constant and varying  $c$ ).

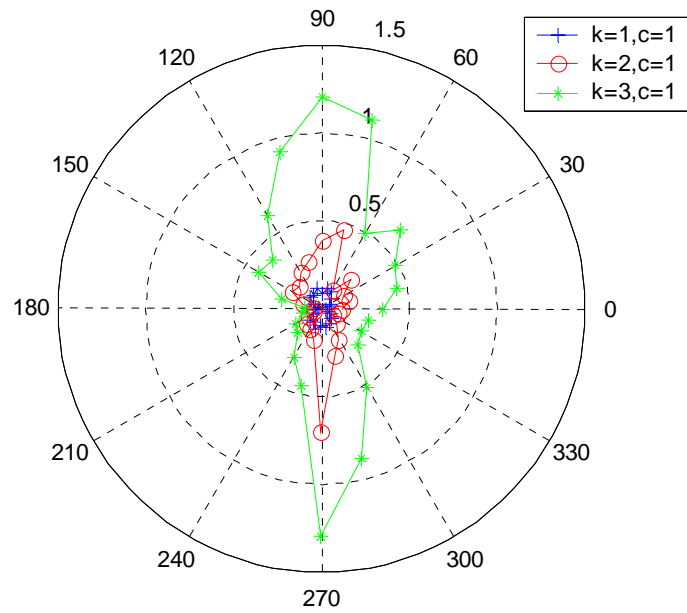


Figure C25. Polar Plot of the RMS Value of the Ramp Twist, (holding  $c$  constant and varying  $k$ ).

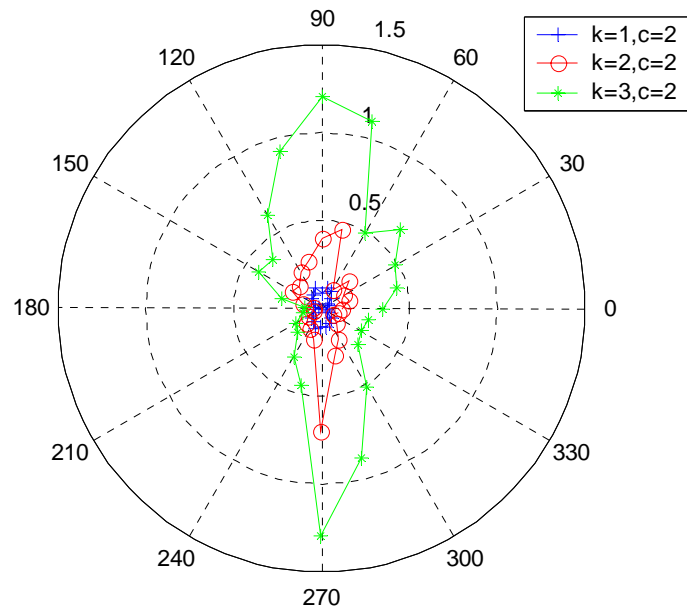


Figure C26. Polar Plot of the RMS Value of the Ramp Twist, (holding  $c$  constant and varying  $k$ ).

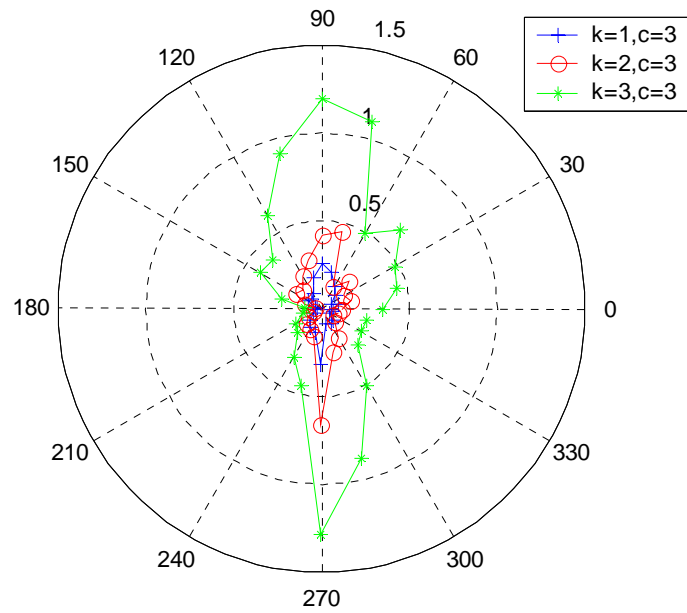


Figure C27. Polar Plot of the RMS Value of the Ramp Twist, (holding  $c$  constant and varying  $k$ ).

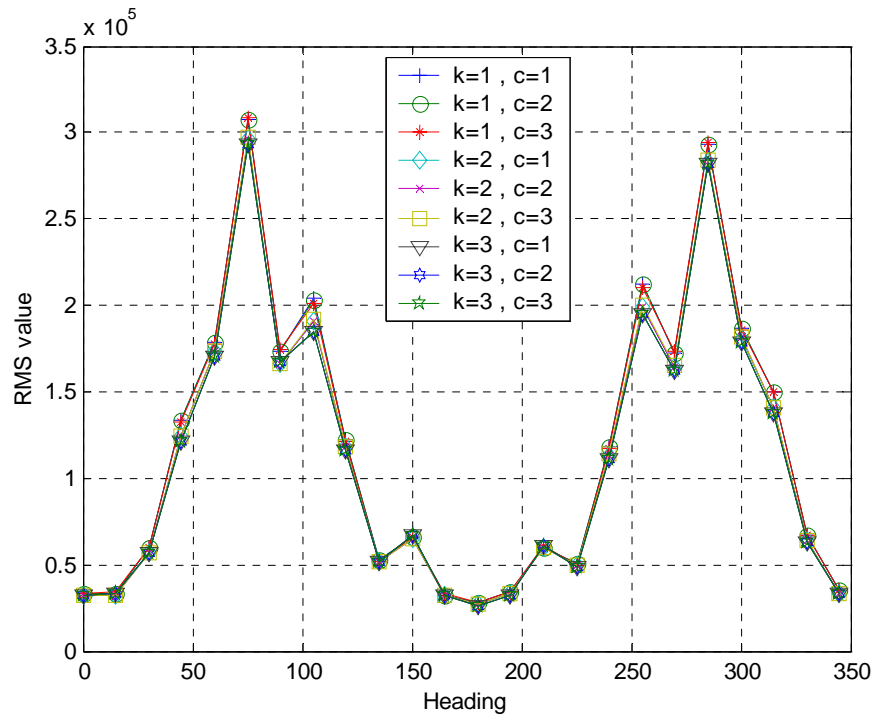


Figure C28. RMS Value of the Ramp Maximum Stress for all the Cases Considered



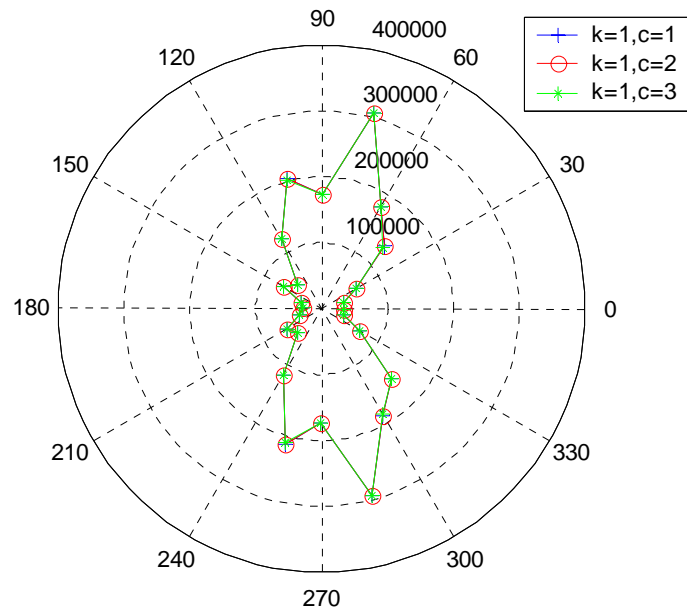


Figure C29. Polar Plot of the RMS Value of the Ramp Maximum Stress, (holding  $k$  constant and varying  $c$ ).

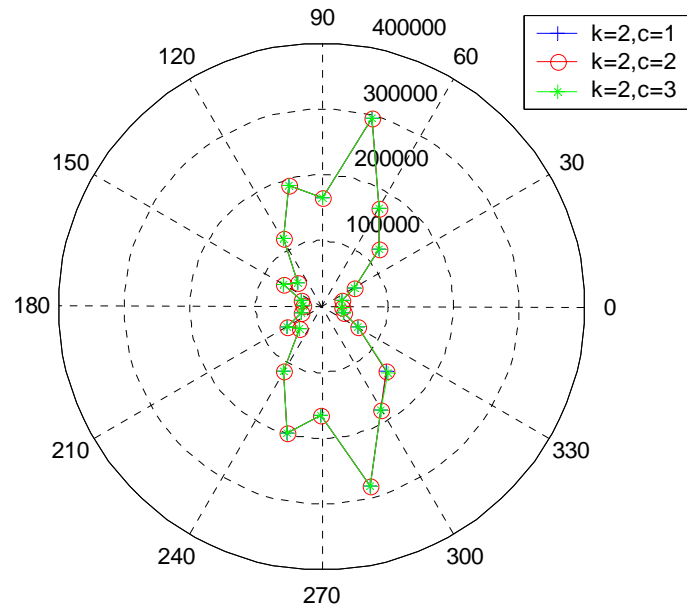


Figure C30. Polar Plot of the RMS Value of the Ramp Maximum Stress, (holding  $k$  constant and varying  $c$ ).

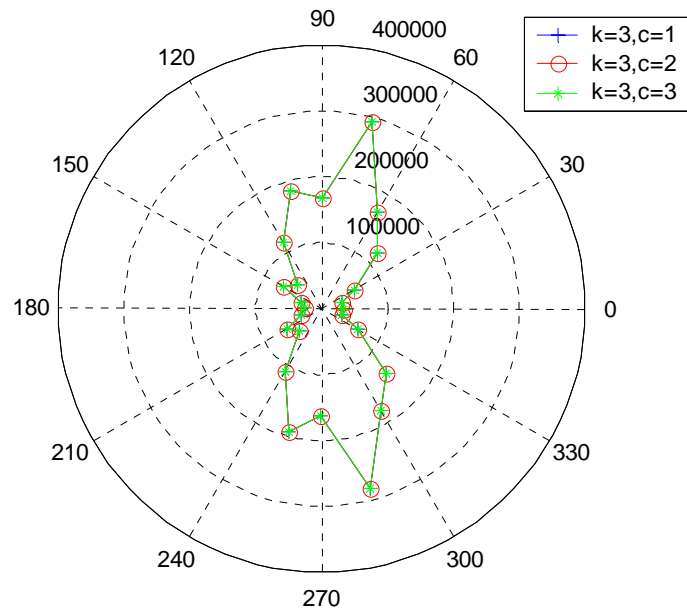


Figure C31. Polar Plot of the RMS Value of the Ramp Maximum Stress, (holding  $k$  constant and varying  $c$ ).

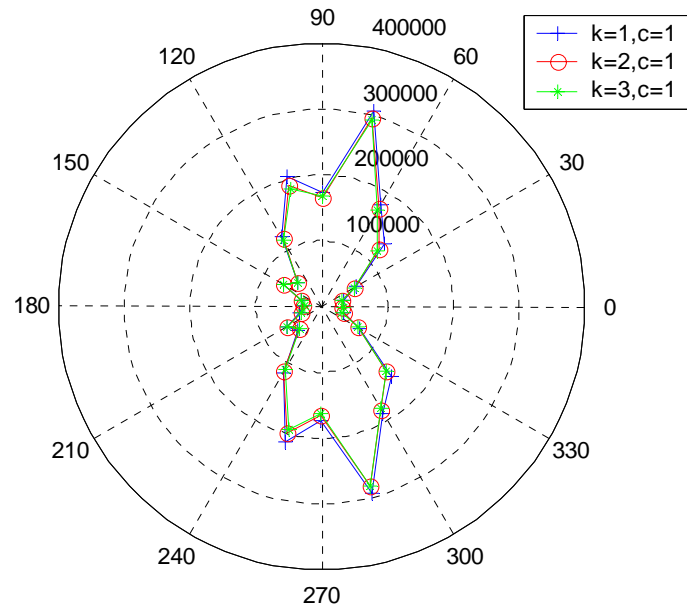


Figure C32. Polar Plot of the RMS Value of the Ramp Maximum Stress, (holding  $c$  constant and varying  $k$ ).

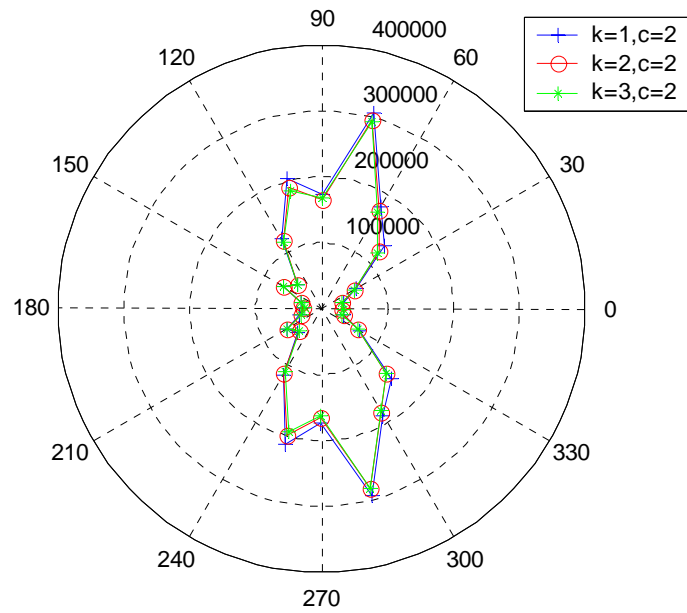


Figure C33. Polar Plot of the RMS Value of the Ramp Maximum Stress, (holding  $c$  constant and varying  $k$ ).

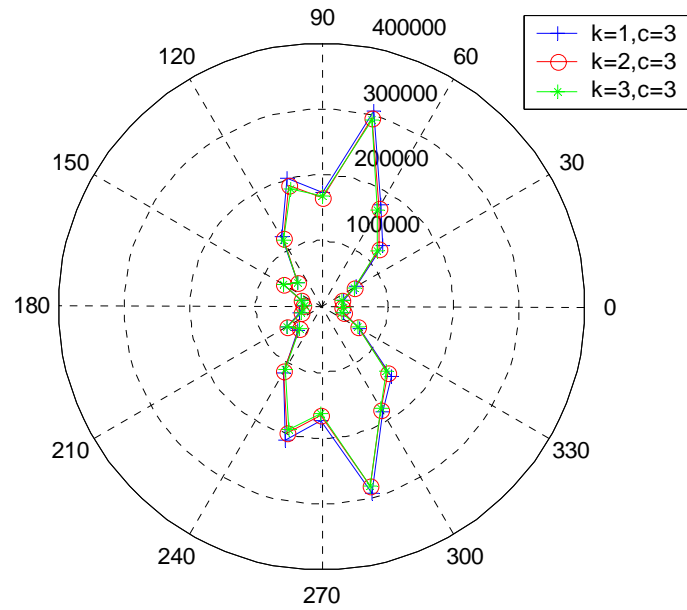


Figure C34. Polar Plot of the RMS Value of the Ramp Maximum Stress, (holding  $c$  constant and varying  $k$ ).

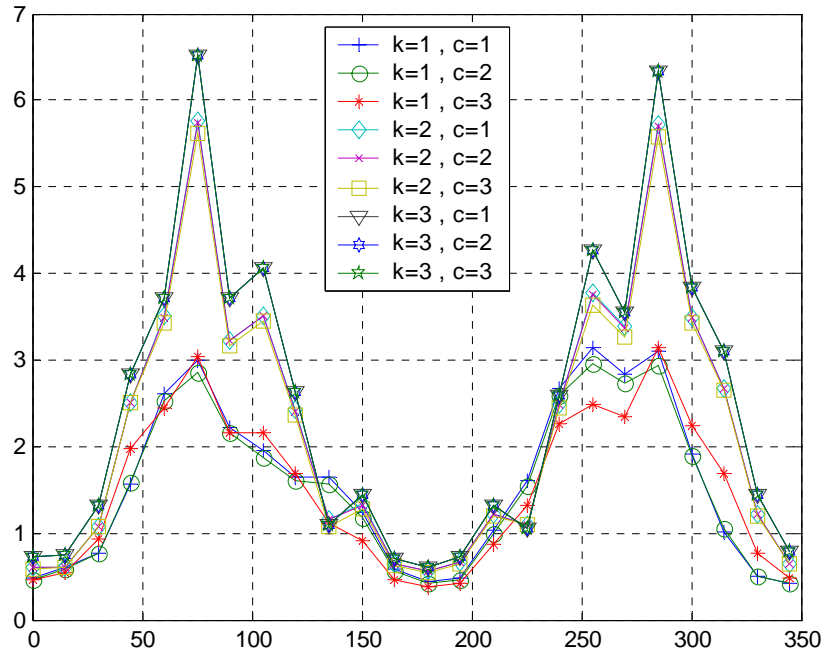


Figure C35. Plot of the RMS Value of the Barge Vertical Motion ( $\xi$ ) at Connection Point A for Cases Considered.

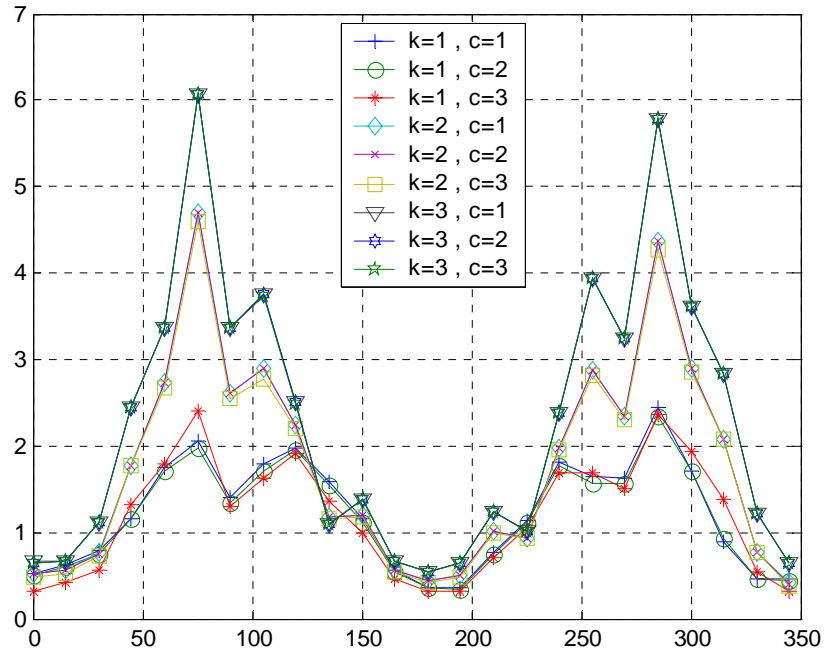


Figure C36. Plot of the RMS Value of the Barge Vertical Motion ( $\xi$ ) at Connection Point B for all Cases Considered.

THIS PAGE INTENTIONALLY LEFT BLANK

## LIST OF REFERENCES

1. Beck & Reed, *Modern Computational Methods for Ships in Seaway*, 12 August 2001.
2. Edward V Lewis, Editor, *Principles of Naval Architecture, Volume III, Motions in Waves and Controllability*, The Society of Naval Architects and Marine Engineers, pp. 1-125, 1989.
3. Dimitrios S. Konstantinou, *Random Wave Analysis of Ship/Ramp/Barge Response*, Master Thesis, Naval Postgraduate School, September 2000.
4. *WAMIT User Manual Versions 6.0, 6.0PC, 5.3S*, WAMIT Inc., [www.wamit.com](http://www.wamit.com), 2000.
5. G. Yang, B.F. Spencer, Jr., *Reduced Ramp Stress Levels Using "Smart" Dumping*, University of Notre Dame.
6. James E. Buckley, *Computational Mechanics of the Full-Scale and Model-Scale RORO Stern Ramp and Experimental Modal Analysis of the Model-Scale Ramp and Support*, Master Thesis, Naval Postgraduate School, September 2000.
7. Young W Kwon, Hyochoong Bang, *Finite Elements Method Using MATLAB Second Edition*, CRC Press, 2000.
8. Kathryn K. McCreight *A Note on the Selection of Wave Spectra for Design Evaluation* Naval Surface Warfare Center, January 1998.
9. J. H. Gordis, *Integral Equation Formulation for Transient Structural Synthesis* AIAA Journal, February 1995.

THIS PAGE INTENTIONALLY LEFT BLANK

## INITIAL DISTRIBUTION LIST

1. Defense Technical Information Center  
Ft. Belvoir, Virginia
2. Dudley Knox Library  
Naval Postgraduate School  
Monterey, California
3. Chairman, Code ME  
Department of Mechanical Engineering  
Naval Postgraduate School  
Monterey,
4. Engineering and Technology Curricular Office, Code 34  
Naval Postgraduate School  
Monterey, CA
5. Professor Fotis A. Papoulias, Code ME/PA  
Naval Postgraduate School  
Monterey, CA
6. Hellenic Navy General Staff/  
Personnel & Education Department  
Papagos Athens  
Greece
7. LT Antonios Dalakos  
Daidalou 13A Nikaia  
Pireas TK 18454  
Greece